PSFC/RR-09-8 **DOE/ET-54512-366**

A Study of Reversed Shear Alfvén Eigenmodes in Alcator C-Mod with Phase Contrast Imaging

E.M. Edlund

May 2009

Plasma Science and Fusion Center
Massachusetts Institute of Technology
Cambridge MA 02139 USA

This work was supported by the U.S. Department of Energy, Grant Nos. DE-FC02-99-ER54512 and DE-FC02-04ER54698. Reproduction, translation, publication, use and disposal, in whole or in part, by or for the United States government is permitted.

A Study of Reversed Shear Alfvén Eigenmodes in Alcator C-Mod with Phase Contrast Imaging

by

Eric Matthias Edlund

B.S. (2003), Departments of Physics and Mathematics,
California State University, Chico

Submitted to the Department of Physics
in partial fulfillment of the requirements for the degree of

Doctor of Philosophy

at the

MASSACHUSETTS INSTITUTE OF TECHNOLOGY

September 2009

Author . . . .
Department of Physics
August 28, 2009

Certified by . . . .
Miklos Porkolab
Professor of Physics
Thesis Supervisor

Accepted by . . . .
Thomas J. Greytak
Professor of Physics
Associate Department Head for Education

A Study of Reversed Shear Alfvén Eigenmodes in Alcator C-Mod with Phase Contrast Imaging

by

Eric Matthias Edlund

Submitted to the Department of Physics
on August 28, 2009, in partial fulfillment of the
requirements for the degree of
Doctor of Philosophy

Abstract

Shear Alfvén waves are a fundamental mode of magnetized plasma oscillation and may exist in tokamak plasmas as eigenmodes with a global structure and discrete frequencies. The inhomogeneity of the plasma profiles in conjunction with tokamak geometry tends to focus the Alfvén waves in regions of near uniformity defined by local extrema in the Alfvén continuum, a quantity which describes the local Alfvén resonance frequency for particular mode numbers. Modes excited in the vicinity of these near uniform regions may be weakly damped and excited by energetic ions. The reversed shear Alfvén eigenmode (RSAE), localized deep in the plasma core, is typically associated with a minimum in q in reversed magnetic shear configurations. RSAEs have proven especially useful for MHD spectroscopy, that is the inference of plasma equilibrium properties through their frequency spectra, due to their high sensitivity to the value of q_{min}. Reversed shear equilibria during the current ramp-up phase and sawtoothing phase are studied through the spatial and temporal characteristics of the RSAEs. Analysis of the spatial structures of RSAEs measured by phase contrast imaging, and interpreted with a synthetic diagnostic using numerical results from the ideal MHD code NOVA, provides constraints on the evolution of q_{min}. Additional observations including mode coupling, mode tunneling, and minimum frequency scaling are discussed in light of theoretical and numerical models, with commentary on possible future experiments.

Thesis Supervisor: Miklos Porkolab
Title: Professor of Physics

Acknowledgments

Six years have passed since I first joined the Alcator C-Mod group at MIT. The culminating experience of writing my thesis transformed many thoughts, forcing vague ideas to take definite form on the page. Simultaneously experiencing and witnessing this transformation, it seems I have become student and teacher both. Many have contributed to my education and success, and the contributions have taken many forms, but all unified in a single essence I think of as grace, perhaps the most noble and mysterious of virtues. I am humbled to have shared this time with so many who possess so much. This thesis would not be complete without an acknowledgement of those who have inspired me on this journey.

I would first of all like to thank my friend and fellow classmate from Chico State, Lukas Kennedy, whose belief in me helped me through dark times when I did not believe in myself. To Ilana Brito, I give my sincerest gratitude for bringing me peace and adventure through the years. I am proud to have ridden with Paul Nerenberg, Seth Behrends, Issao Fujiwara, Jason Sears, Chris Tracy and Keith Berkoben, comrades of the wheel who embrace the passion of competition at its highest. These times would have been empty without the company of my fellow graduate students at the PSFC with whom I've shared many good words and good laughs: Roark Marsh, Arturo Dominguez, Balint Veto, Jason Sears, Greg Wallace, Noah Smick, Brock Böse, Alex Parisot, Felix Parra-Diaz, Naoto Tsujii, Antoine Cerfon, Istvan Czeigler and Will Fox. I would like to give particular acknowledgement to Liang Lin, my compatriot for six years in all things PCI, office mate, and the level voice that kept me focused when I drifted on theoretical tangents. And to my family, who has always provided me a warm welcome and generosity in what ways they could afford, I want to say only that I love you and I always look forward to coming home.

I am indebted to the Alcator C-Mod group for their support over the years. These experiments could not have been conducted without the expert assistance of the many dedicated staff and scientists. In particular, I would like to thank Bill Parkin, Ed Fitzgerald, Tommy Toland and Andy Pfeiffer for their contributions in day-to-day operations. Thanks to Earl Marmar for supporting the next generation of plasma physicists, and to Earl and Steve Wolfe for running a successful experimental program. Steve Wuktich taught me the importance of getting it done, an invaluable skill when working on a thesis, perhaps to him I owe the clarity of mind I have enjoyed these last few weeks.

Lastly, I would like to thank my teachers and mentors. Among the many professors I've had the great opportunity to study under at MIT, I need also to acknowledge the influence of my undergraduate professors, namely Eric Dietz, Vladimir Rosenhaus and Louis Buchholtz who inspired me to pursue physics at its highest. Bruno Coppi has been a model professor, dedicated to sharing with the next generation the wisdom of the past. Among my mentors in my thesis studies I would like to acknowledge Gerrit Kramer, whose generosity has been invaluable and inspiring. Many thanks to my thesis committee, Jan Egedal, John Belcher and Miklos Porkolab for helping me find the essence of an argument and the holes in my understanding. The success of my thesis defense is in large part due to their criticism of and attention to my research over the years. Above all, I would like to recognize the dedication of my advisor, Miklos Porkolab. If there is one paramount virtue I admire in Miklos it is his ability to embrace the mathematics of a problem, and with physical insight in one hand and patience in the other, discover the meaning of things.

The graduate experience is at times a lonely and arduous process, but also one of deep camaraderie and supreme delight. The university is one of the most remarkable creations in the history of man, an institution dedicated to the development of the mind and the exploration of our world. At the root of all our efforts we seek an understanding of ourselves and our place in the cosmos. As scientists we endeavor to unearth the great patterns and find the connections that link the atoms and the stars. As citizens we should share our understanding with our culture and help to free it from the shackles of the past. We should ask ourselves daily, “in what capacity can I best serve?” At the end of the day we should be judged not by what we have done, but by what more we could have done. I am honored to have walked the halls of one of the world’s premier institutions, and aspire to carry forth the light of patient study.

Contents

List of Figures

Chapter 1

Introduction

The overarching motivation of tokamak research is to study control and confinement of plasmas at with magnetic fields temperatures on the order of 10 keV and densities on the order of 10^{20} m^{-3} as a method of harnessing the potential energy released from the fusion of hydrogen isotopes. Most generally, the tokamak confines a plasma with magnetic fields which trap particles along closed magnetic field lines which form toroidally symmetric surfaces. The magnetic field is composed of a dominant toroidal field, largely induced by magnetic coils external to the vacuum vessel, and a poloidal field which is generated by a current flowing in the plasma itself. The plasma is however, slightly diamagnetic, arising from the fact the gyro-motion of the particles do not perfectly cancel in the presence of a pressure gradient, resulting in a poloidal current. These field components sum to form an equilibrium configuration of nested, toroidal helices. To lowest order, the plasma shape is characterized by two parameters: the major radius (R_0) which is the distance from the center of the torus to the magnetic axis of the plasma, and the minor radius (a) which is the distance from the magnetic axis to the plasma edge at the outboard midplane. The general

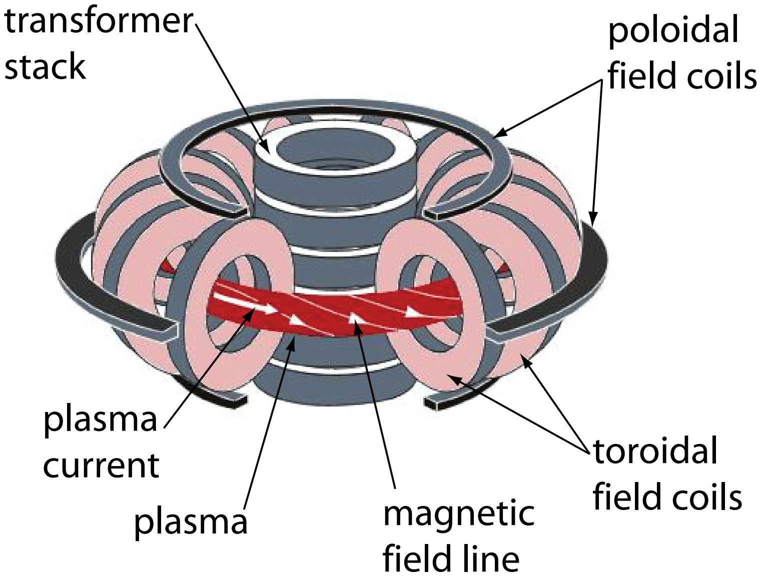

Figure 1-1: Cutaway illustration of the tokamak concept. The transformer stack generates the toroidal electric field which drives the plasma current. The poloidal field coils allow for plasma shaping and provide stability. The vacuum vessel (not shown) is interior to the toroidal field magnets. Used with permission from the EFDA.

structure of a tokamak is presented in Fig. 1-1.

This thesis presents studies of shear Alfvén waves performed at the Alcator C-Mod tokamak at MIT. The Alfvén wave is characterized by strongly coupled magnetic fluctuations and plasma motion dominated by the $\mathbf{E} \times \mathbf{B}$ drift velocity [1], and is present in astrophysical [2] and planetary [3] plasmas, as well as in earth-bound devices such as the tokamak [4]. In a homogenous plasma, magnetic fluctuations from the shear Alfvén wave ($\delta\mathbf{B}$) are orthogonal to the background magnetic field, resulting in a magnetic energy density which is second order in the perturbation, $(\delta B)^2$. In an inhomogeneous plasma the magnetic fluctuation acquires a small component parallel to $\mathbf{B}$. In tokamaks, the wavelength of the shear Alfvén waves parallel to the magnetic

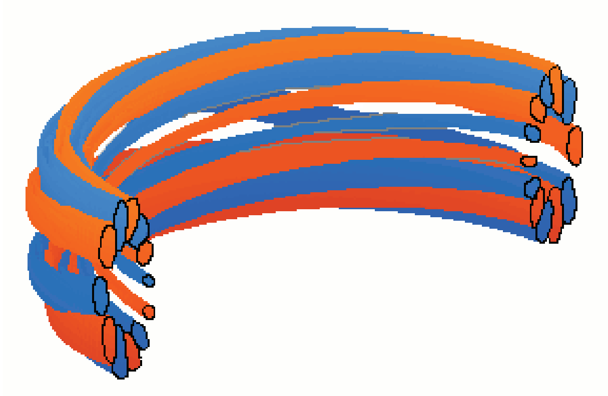

Figure 1-2: Cross-section of the torus illustrating the helical density perturbation (orange is positive and blue is negative) for an Alfvén eigenmode. The structure has a six-fold periodicity in the poloidal plane and a three-fold periodicity in the toroidal plane.

field can be many times the circumference of the magnetic axis so that the waves form as coherent structures, more properly described as eigenmodes of the system. An eigenmode must be periodic in the poloidal and toroidal directions, which results in a structure that follows approximately the local magnetic field lines, as illustrated in Fig. 1-2. A population of resonant high-energy ions can excite the shear Alfvén wave to levels detectable by magnetic and inferferometric diagnostics [5]. This thesis focuses on a particular class of Alfvén eigenmode called the "reversed shear Alfvén eigenmode" (RSAE) [6], or sometimes the "Alfvén cascade" [7, 8, 9], and builds upon former works which have used Alfvén eigenmodes for diagnostic purposes [10, 11, 12].

Studies of the RSAEs are motivated by the desire to know the evolution of the current density profile. The distribution of current in the plasma has important consequences for global tokamak performance, stability of the plasma with respect to a range of instabilities and also for transport processes [13]. Measurement of the current distribution has been called the"holy grail" of plasma diagnostics for this reason. A range of instruments have been designed with the intention of measuring the pitch of the magnetic field lines as a method for determining the poloidal magnetic field structure. Perhaps most notable among these are the motional Stark effect (MSE) diagnostic [14] and the polarimetry diagnostic [15], however, neither of these instruments was available on Alcator C-Mod during the experiments reported in this thesis. Furthermore, there exist circumstances of regular plasma operation where the magnetic field topology may change rapidly, such as the so-called "sawtooth oscillations" [16], and an instrument with fast time response is desired. Recalling that the natural modes of a system represent fundamental properties of the medium itself, e.g. the lattice spacing of a crystal determine the phonon frequencies, the spatial and temporal structure of the RSAEs provides a means for inferring certain properties of the plasma equilibrium magnetic structure to very high accuracy and on short time scales [7, 17, 18, 19]. A second motivating factor for the study of RSAEs is that future tokamaks will have a significant population of high energy alpha particles which are expected to drive many shear Alfvén eigenmodes [20, 21]. The full consequences of this are unknown at this time, though there is some evidence that enhanced transport of energetic ions may result from the excitation of these modes [22, 23]. At the time of the experiments reported in this thesis, we had little ability to accurately diagnose the energetic ion population. Consequently, the issues of energetic ion transport and the energetic ions themselves are somewhat tangential to this thesis. The focus of this work should be regarded as a study of the phenomenon of reversed shear Alfvén eigenmodes with experimental and theoretical approaches. The concluding chapter of this thesis identifies a few possibly fruitful paths with respect to transport, building off of observations reported here.

The primary experimental tool used in the studies reported in this thesis is the phase contrast imaging (PCI) diagnostic, a device which converts variations of phase in the incident laser beam into variations of intensity at the detector [24]. It is interesting that phase contrast imaging, Alfvén eigenmodes, and the diffusion of current in the plasma find a common explanation in the principle of phase coherence. The remainder of this chapter will discuss these aspects as an introduction to the major themes of this thesis.

The phase contrast imaging diagnostic on Alcator C-Mod uses a CO_2 laser with a wavelength of 10.6 μm. It has been remarked that the laser is a device which approaches the ideal measure of coherence [25]. The phase contrast method utilizes this ideal coherence in the measurement of plasma waves. A sinusoidal variation in the index of refraction gives rise to a sinusoidal variation in the phase of the outgoing wave [26]. This result may be derived from ray tracing, where the wavefront of a packet of incident waves is solved by the method of characteristics [27, 28]. The wave equation for the scalar electric field in the case of weak variations in the index of refraction has a wave function given by $\nabla^2 E = -k_0^2 N^2 E$, where $N = c/v_{ph}$ is the index of refraction. Interestingly, the electric field may be interpreted as a quantum quasi-particle of zero energy trapped in a potential well proportional to $-k_0^2 N^2$ when N^2 has a maximum. Conversely, the system admits no stable solutions when N^2 has a minimum. This is precisely the basis for gradient index imaging optics [27], as found in some fiber-optic cables and illustrated in Fig. 1-3. In the presence of a plasma wave which creates a sinusoidal variation in the index of refraction, the incident laser beam will be focused toward regions of lower density and diverted away from regions of higher density.

As a model for a range of phenomena, including the diffraction of a laser beam by a plasma wave, let us consider the modification of the phase of a plane wave traveling in the $+\hat{z}$ direction incident upon an object of uniform thickness but with a spatially varying index of refraction $N(x')$, where x' is the coordinate in the direction per-

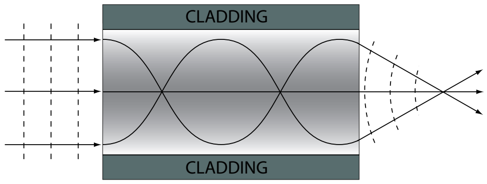

Figure 1-3: Some fiber optic cables utilize a gradient in the index of refraction, where the index has a minimum on axis and increases toward the cladding. The effect is to trap the light waves within the cavity like a particle in a potential well.

pendicular to the direction of propagation. If the variation in the index of refraction is weak we may approximate the true paths of the wavefronts by straight line paths between points on the incident plane and points on the exit plane of the object. The electric field resulting from this interaction is,

$$E(x) = \int_{-\infty}^{+\infty} E_0 \frac{e^{i\Phi(x')}}{r} \mathrm{d}x', \tag{1.1}$$

where E_0 is the incident electric field, x is the coordinate of the outgoing plane separated by a distance z from the incident plane, $\Phi(x')$ is the accumulated phase along the path from x' to x found by integrating $k\,\mathrm{d}l$ along the wavefront, and $r = \sqrt{z^2 + (x - x')^2}$. Equation 1.1 is the mathematical expression of Huygens' principle of wavelet superposition [29], an approximation to the full electromagnetic wave theory in the small angle propagation. The fraction in the integrand may be regarded as the Green's function for spherical wave propagation [30]. Considering a single value of x for the moment, the integrand may be decomposed into symmetric and antisymmetric components. The sum over all rays tends to cancel the asymmetric components, leaving a strong dependence on the symmetric components which is dominated by the part of the integral for which $x' = x$, allowing the outgoing wave

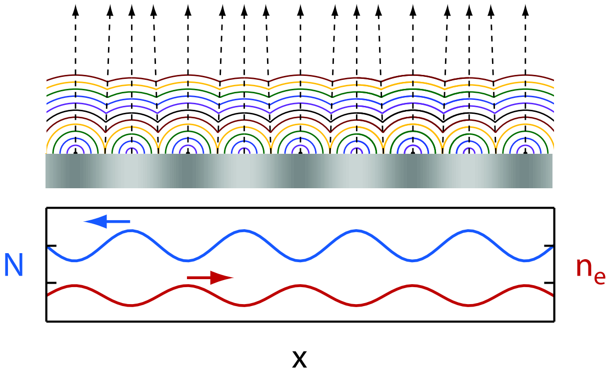

Figure 1-4: An ideal phase object changes the phase of the wavefronts but leaves the amplitude unaffected. In this illustration, a finite number of Huygens radiators approximate the true wave front across the phase object with a sinusoidal variation in the index refraction N. Regions of higher index of refraction, which in a plasma corresponds to a negative density perturbations, result in slower wave phase velocity and a convergence of the wavefront.

to be approximated as

$$E(x) \approx E_0 e^{i\Phi(x)}, \tag{1.2}$$

where $\Phi(x) = (\omega/c)N(x)L$ and L is the thickness of the object. An example of the phase at the outgoing surface of an object calculated by this method is shown in Fig. 1-4. The wave fronts of the outgoing wave are focused toward regions of higher index of refraction. This effect is the basis of gradient-index imaging, present in some fiber optic cables and the human eye for example.

Equivalently, we may think of the incident plane wave as scattering off of the plasma wave, producing three outgoing plane waves, a diffraction of the incident wave. This process touches at the question posed by Richard Feynman [31] when he asked how any individual photon knows whether to reflect off the glass, or to pass through, speaking on the phenomena of partial reflectance. Feynman's answer is that there is no single path for a photon. Rather, the field takes every possible path and interferes with itself, as exemplified in Young's double-slit experiment. Where the phases of these separate paths add coherently the probability amplitude is largest. The ensemble average of many measurements of this probability function forms the patterns we record. This is a generalization of wave mechanics which joins classical optics with discontinuous and diffusive processes of particles.

We may extend the idea of coherence to consider the propagation of plasma waves in a plasma acting as a phase object when the waves avoid resonances which absorb or transfer the energy to other forms. Consider, for example, the dispersion of shear Alfvén waves, that is $\omega_A^2 = k_\parallel^2 v_A^2$, where $k_\parallel$ is the wavenumber parallel to the magnetic field, $v_A^2 = B^2/\mu_0\rho$ is the characteristic Alfvén speed, B is the modulus of the magnetic field and ρ is the mass density [1]. In the case of the nested helical magnetic fields, as found in tokamak plasmas, the path length along the magnetic field lines of different magnetic surfaces may express strong variation due to the difference in pitch of the field lines. Similar to the prior discussion, we may imagine a packet of shear Alfvén wavelets incident on the plasma and inquire as to where we expect to find coherence. We define the parallel index of refraction through $N_\parallel^2 = c^2 k_\parallel^2/\omega^2 = (c/v_A)^2(\omega_A^2/\omega^2)$. Considering the case of negligible variation in v_A^2, we expect coherence around maxima in ω_A^2, where the Alfvén wavelets form into eigenmodes, similar to the former discussion of light waves and the generalized phase object. Conversely, a minimum in this function tends to diverge the incident Alfvén waves and only very narrow eigenmodes may form which are not expected to be excited in experiment. This describes the fundamental nature of the eigenmodes we will consider in this thesis. We may liken the Alfvén eigenmodes to a light wave trapped around a maxima in the index of refraction in a fiber optic cable.

As a last note, we consider current diffusion, the subject of chapter 6. It can be shown from a discretized form of the diffusion equation that the evolution is equivalent to a sum over all possible paths of a particle (or field quantity) between point x at time t and a point x' at a later time t'. We may then think of the process of diffusion as a movement toward a most probable state arising from the intersection of an infinite number of paths, a coherence of random walks. While the concept of coherence in the studies of diffusion is not present as a condition in the particular problem we investigate here, it is nonetheless in the background of our thoughts. The diffusion of current arises from collisions and possibly turbulence which scatter the electrons, the primary carriers of current. In chapter 6, we investigate the conditions under which a particular current profile shape arises, a critical condition for the development of the Alfvén eigenmodes central to this thesis.

This thesis progresses to an overview of the Alcator C-Mod tokamak and the PCI diagnostic in chapter 2. A theory of RSAEs is developed in chapter 3 with additional commentary on the use of codes for the solution of the eigenmodes in toroidal geometry. Chapters 4 and 5 investigate RSAEs during the current ramp phase and the sawtoothing phase, respectively. The main body of the thesis is concluded in chapter 6 with a brief discussion of a one dimensional model of current diffusion based on observations of RSAEs, followed by closing remarks in chapter 7.

Regarding the analysis and equations presented in this work, the author has attempted to convert all formula to the MKS system of units. The only exception to this is that energies are reported in terms of the keV rather than the proper MKS unit of the Joule. Generally, a bold-face character refers to a vector quantity as in the magnetic field, $\mathbf{B}$, and a subscripted variable as a vector component as in B_r.

Chapter 2

Experiments and Diagnostics

Alcator C-Mod, located at the Massachusetts Institute of Technology, is a high-field, high current, compact tokamak, regularly operating at reactor relevant densities at or above $1 \times 10^{20}\,\mathrm{m}^{-3}$ and magnetic fields up to 8 Tesla [32]. Like other contemporary tokamaks, Alcator C-Mod utilizes a "divertor", a first wall region designed to handle high heat loads and is actively pumped to help reduce impurity accumulation and control density. The magnetic field topology is most often configured such that magnetic field lines just outside of the last closed flux surface of the plasma intersect the first wall in the divertor region. Exceptions to this are the so-called "wall limited" configurations where the plasma position is limited by contact with a portion of the inner wall, a circumstance which is necessarily present in the early current ramp phase of Alcator C-Mod experiments. Typically, a plasma may become "diverted" around 200 ms into an experiment, though this has been pushed as early as 140 ms in some aggressively shaped cases. An ion cyclotron resonance heating (ICRH) antenna system located within the vacuum vessel on the outboard wall provides auxiliary heating in excess of 5 MW of coupled power [33]. Electron temperatures in the range of 3 – 6 keV are regularly achieved with ICRH. Alcator C-Mod will be discussed in greater detail in section 2.1 of this chapter.

The harsh environment of the plasma essentially dictates that measurements of the plasma core must utilize radiation or beams as a probing medium. The Thomson scattering diagnostic, for example, collects the scattered light from an incident laser beam to measure the plasma electron density and temperature. X-ray and infrared imaging diagnostics, on the other hand, are passive diagnostics which collect radiation emitted by the plasma. This chapter focuses on the two primary diagnostics used for the measurement of Alfvén waves in Alcator C-Mod. The phase contrast imaging (PCI) diagnostic, a type of laser interferometer utilizing an internal reference beam, is particularly sensitive to fluctuations of the electron density and comprises the core of the diagnostic effort. Many of the measurements from this diagnostic are compared to and complemented by measurements from the Mirnov coils, wall-mounted magnetic pick-up coils designed for optimal sensitivity to fluctuations of the poloidal magnetic field. The phase contrast imaging and Mirnov coil diagnostic systems will be discussed in sections 2.2 and 2.3.

2.1 Alcator C-Mod

With regard to this thesis work, the most important aspects of the Alcator C-Mod tokamak are its size, toroidal magnetic field, plasma current and characteristic values of the central density and temperature. Representative parameters of Alcator C-Mod operating parameters for the Alfvén eigenmode studies are presented in Table 2.1. The energy confinement time is derived from the ratio of the stored energy in the plasma to the total input power. A typical total plasma energy is in the range of 50 – 100 kJ for these experiments, with total input power in the range of

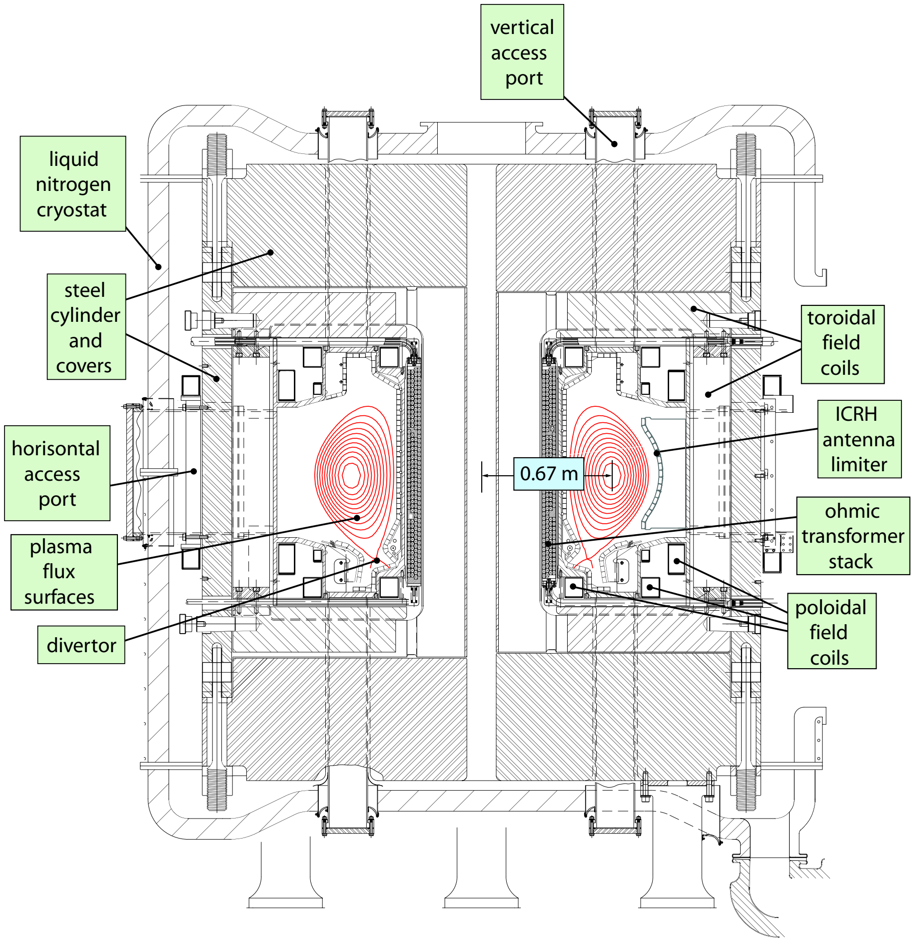

Figure 2-1: Cross section of the Alcator C-Mod tokamak, adapted from Ref. [34].

$3-6\,\mathrm{MW}$. The resistive diffusion time (τ_η) is a scale factor derived from the resistive diffusion coefficient and a characteristic length scale, $D_\eta = \eta/\mu_0 \sim r_{eff}^2/\tau_\eta$, where $\eta \approx m_e Z e^2 \ln\Lambda/12\pi^{3/2}\epsilon_0^2 T_e^{3/2}$ is some average measure of plasma resistivity based on classical Coulomb collisions only, and m_e is the electron mass, Z is the ion charge state, $\ln\Lambda \sim 17$ is the Coulomb logarithm, and in this expression T_e is in units of Joules [35]. This form is numerically equivalent to $\eta \approx 3 \times 10^{-8}\, Z T_e^{-3/2}\,\Omega\,\mathrm{m}$, with T_e in keV. The value of τ_η in Table 2.1 used an average temperature of 2 keV and $r_{eff} = a/2$ to model the current ramp-phase, which expresses the fact that the time scale should be weighted by the hotter plasma core because of the $T_e^{3/2}$ scaling of τ_η.

major radius	R_0	$0.67\,\mathrm{m}$
minor radius	a	$0.21\,\mathrm{m}$
elongation	κ	≤ 1.6
triangularity	δ	≤ 0.55
toroidal magnetic field at R_0	B_0	$5.4\,\mathrm{T}$
total plasma current	I_p	$800\,\mathrm{kA}$
central current density	j_0	$\leq 15\,\mathrm{MA\,m^{-2}}$
central electron density	n_{e0}	$\leq 1.5\,10^{20}\,\mathrm{m^{-3}}$
central electron temperature	T_{e0}	$\leq 6\,\mathrm{keV}$
ICRH power	P_{ICRH}	$2-5\,\mathrm{MW}$
majority ion species		deuterium
minority ion species		hydrogen
pulse length	τ_{pulse}	$\leq 3\,\mathrm{s}$
energy confinement time	τ_E	$\sim 20\,\mathrm{ms}$
resistive time scale	τ_η	$\sim 200\,\mathrm{ms}$

Table 2.1: Characteristic operating parameters for Alcator C-Mod during the Alfvén eigenmode experiments.

There are two main aspects of tokamak operation which concern these studies: the diffusion or relaxation of the current within the plasma, and the auxiliary heating of the plasma with the ICRH system. With regard to the latter, it is really the development of an energetic ion population, the drive for the Alfvén eigenmodes, that is most important. We will examine each of these topics in more detail.

2.1.1 Current Penetration

Following the initial breakdown of the deuterium gas, the plasma current increases due to the application of a toroidal electric field beyond that required to balance the internal resistivity. The loop voltage ($= 2\pi R E_\phi$) during this phase peaks at approximately 5 Volts. In tokamaks, pressure balance is achieved through the Hall force arising from the induced current, that is $\nabla p = \mathbf{j} \times \mathbf{B}$ [36]. We may derive a simple scaling relation for the central pressure by balancing the ∇p force with the $\mathbf{j} \times \mathbf{B}$ force, and assuming the latter is approximated by the $j_\phi B_\theta$ term. In this approximation we may think of the plasma as a bundle of wires, carrying current in the toroidal direction, attracting each other through their mutual $\mathbf{j} \times \mathbf{B}$ forces. While this certainly overlooks the important contribution from the poloidal current and the toroidal field, it serves to derive the scaling. Using Ampere's Law and assuming a reasonable gaussian current density profile peaking at the magnetic axis, we have $p_0 \sim (\mu_0 F / 4\pi^2) I_p^2 / a^2$ where p_0 is the value of the pressure at the magnetic axis and F is a function of the current density profile and is approximately 3. Using values representative of Alcator C-Mod, with $a = 0.2$ m, a central electron density of $n_{e0} \sim 2 \times 10^{20}\,\mathrm{m}^{-3}$, a central electron temperature of $T_{e0} \sim 5$keV and assuming $T_i = T_e$, we derive a requirement of $I_p \sim 0.5$ MA, which is not far from the typical operating current of 0.8 MA.

The finite resistivity of the plasma causes the current to penetrate on a time scale proportional to $T_e^{3/2}$. The deviation from the steady-state configuration may be quite large when one considers the resistive time scale and that approximately 1

MA of current must diffuse through the plasma. A current profile peaking away from the magnetic axis is known as a "hollow" current density profile, or equivalently, a "reversed shear q profile". Most often, the temperature profile peaks on axis, so that the conductivity profile also peaks on axis which induces a transient pile-up of current off axis [37]. In the special case of early application of ICRH, starting around 100 ms in the experiments reported here, the temperature profile may increase rapidly much more quickly than the current profile, causing the current to lag further behind and maintaining the reversed shear state for a longer than usual period. The parameter q describes the ratio of the winding of the magnetic field in the toroidal direction to the winding in the poloidal direction, and near the core can be approximated by $q = rB_0/R_0B_\theta$. The approximate $1/R$ form of the toroidal field implies that a global factor like q should be properly defined as a flux surfaced averaged quantity, hence the toroidal field in the former definition of q uses the central value as an average. During the current ramp phase of the experiments, q_{min} decreases to 2 in the first 100 msec and then to 1 over the next 150 msec, approximately. It is this period, when both a reversed shear q profile and an energetic ion population are present, that the reversed shear Alfvén eigenmodes are typically excited.

Following the current ramp phase of operation, when $q \approx 1$, the plasma enters a period of quasi-steady-state operation. In most operating scenarios there exists a periodic oscillation of the central equilibrium called the "sawtooth cycle" [16]. From the presence of reversed shear Alfvén eigenmodes during some sawteeth cycles, the presence of a reversed shear q profile has been inferred [18, 19]. This may be anticipated by considering the resistive time scale relevant to relaxations of the current profile on a smaller internal scale, say using $a/3$ and $T_e \sim 4\,\text{keV}$, giving $\tau_\eta \sim 30\,\text{msec}$. This time scale is longer than most sawtooth periods in Alcator C-Mod, suggesting that the current never fully reaches steady-state with respect to the resistivity profile. This topic is discussed in more detail in chapters 5 and 6.

The scaling of the central pressure derived earlier suggests that a large device, such as ITER, with a minor radius nearly an order of magnitude larger than Alcator C-Mod will need a comparably larger plasma current to achieve similar pressures. The ITER design calls for a nominal plasma current of approximately 10 MA. Operation in these regimes may require the development of a large “bootstrap” current, an internally generated current [13, 38, 39, 40]. The resistive time scale, proportional to a^2, should be at least 20 seconds for ITER and possibly much longer depending on the temperature of the plasma core. This suggests that there will be a large window of operation in which to explore the interesting physics of reversed shear configurations in reactor scale plasmas. It is likely that a range of Alfvén eigenmodes, including RSAEs, may be excited during this period and could provide additional information on the core alpha particle population [41].

2.1.2 Ion Cyclotron Resonance Heating

Auxiliary heating on Alcator C-Mod is supplied primarily by the ion-cyclotron resonant heating (ICRH) system. Three separate antenna systems, composed of two groups of two-strap antennas (D-port and E-port) and one four-strap antenna (J-port), launch waves at 80.5, 80.0 and 78.0 MHz respectively [33]. The ICRH system can couple as much as 5 MW, with fairly reliable operation at 4 MW or less. As the main heating source for the Alfvén wave experiments in this thesis, a brief outline of ion-cyclotron resonant heating (ICRH) is provided. The main regime of operation is the so-called “minority heating” case, where minority ions, in our case hydrogen in a deuterium majority, are accelerated at the layer where the launched frequency equals the minority cyclotron frequency, a function of $B_\phi \sim B_0(R_0/R)$ [42, 43]. By adjusting the magnitude of the toroidal field, one may select the major radius of the resonance and hence a particular value of $v_\perp/v_\parallel$ in velocity space which is preferentially heated. The subset of the minority population whose orbits stagnate near (have banana orbit tips near) the resonant layer will be most strongly accelerated. At $B_0 = 5.4\,\mathrm{T}$ the E-port antenna is resonant at a radius of about 68 cm, the D-port antenna about 0.5 cm to the high-field side (HFS) and the J-port antenna about 1.5 cm to the low-field side (LFS). The energetic ion population resulting from this heating scheme has been explored with a neutral particle analyzer on Alcator C-Mod where it was found that even with on-axis heating, the energetic ion profile tended to peak off-axis, an effect explained by the greater number of orbits which are trapped at larger minor radii [44]. A typical tail temperature of approximately 100 keV was found for an injected power of about 0.5 MW in a densities in the range of $(0.8 - 1.5) \times 10^{20}\,\mathrm{m}^{-3}$.

Extensive discussions of the physics of ICRH wave propagation can be found in Ref. [42] and [45]. Rather than reiterate these issues in total, we present a brief calculation of the expected energetic ion tail temperatures based on analysis in these references as a consideration for calculations presented in subsequent chapters which use a model ICRH distribution to calculate the growth rate of Alfvén eigenmodes. A steady-state energetic ion distribution is found by balancing the source of accelerated ions from the ICRH waves and the loss of energetic ions due to scattering from the electrons (primarily), modeled by the quasi-linear diffusion process. An analytic form of the steady-state distribution function is provided on page 511 of Ref. [42]. Distribution functions for the energetic hydrogen minority population are shown in Fig. 2-2, calculated with a numerical routine provided by V. Tang [46].

The quasi-linear calculations of the minority tail temperatures depend on the order of 100 keV, possibly smaller or larger depending on the specifics of the equilibrium. The flux-surface averaged power density $(\tilde{P})$ is equal to the input power

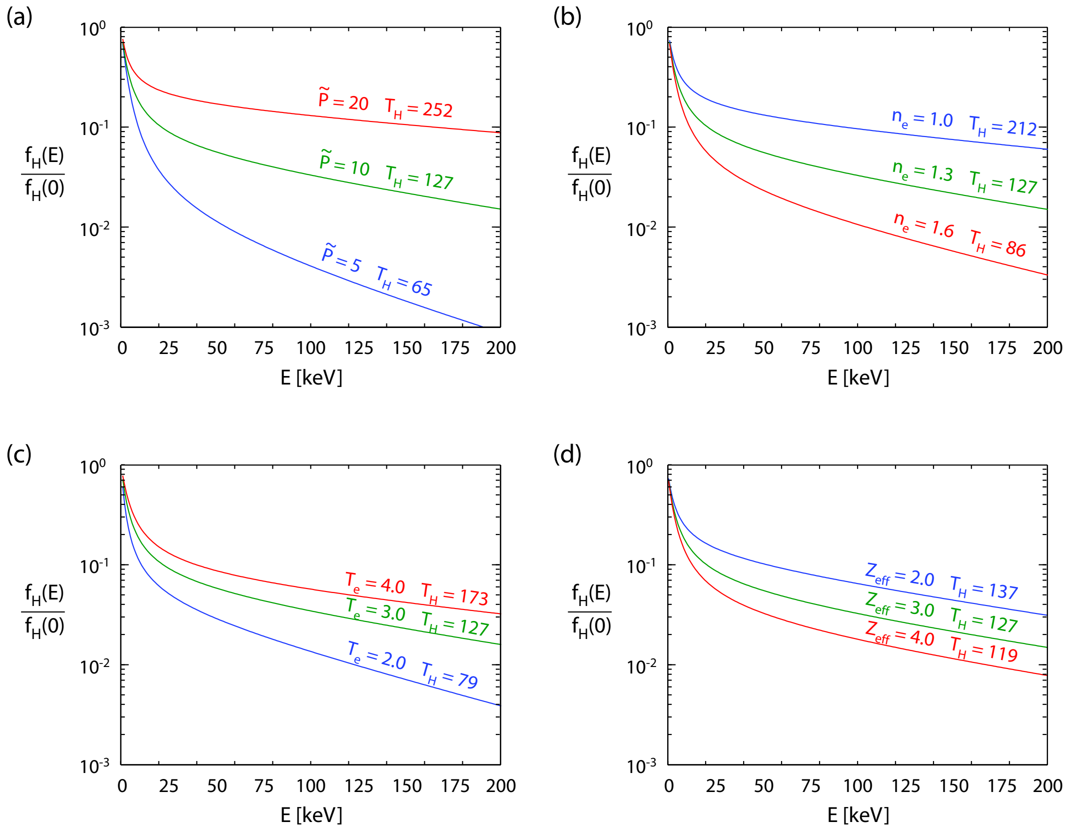

Figure 2-2: Calculations of the steady-state distribution function for a hydrogen minority species in deuterium majority based on quasi-linear estimates from Ref. [42]. $\tilde{P}$ is the flux-surface averaged power density in units of W/cm^3, temperatures are in units of keV, n_e is in units of 10^{20} m^{-3}, and $Z_{eff} = \sum_s n_s Z_z^2 / n_e$ is a sum over ion species and represents the effective charge state of the plasma for collisional processes. Model parameters are (a) $n_e = 1.3$, $T_e = 3.0$, $Z_{eff} = 3.0$ (b) $\tilde{P} = 10$, $T_e = 3.0$, $Z_{eff} = 3.0$ (c) $\tilde{P} = 10$, $n_e = 1.3$, $Z_{eff} = 3.0$ (d) $\tilde{P} = 10$, $n_e = 1.3$, $T_e = 3.0$.

divided by the volume of the flux surfaces over which the power is deposited. For on-axis resonance, the volume can be approximated by $(2\pi R_0)(\pi r_{res}^2)$, where r_{res} is the radial extent of the wave-field above the magnetic axis. Using an injected power of 3 MW we find $\tilde{P} \sim 20\,\mathrm{W/cm^3}$ [47], putting the tail temperature in the range of 100 – 200 keV. These values are likely overestimates of the tail temperatures as the deuterons and electrons also absorb the incident power, perhaps upwards of 30% [43].

2.2 Phase Contrast Imaging

The method of phase contrast imaging developed out of Fritz Zernike's study of imperfections in diffraction gratings [26], a work for which he was awarded the Nobel Prize in Physics in 1953. Prior to his studies, it had been known that periodic imperfections in a diffraction grating produced so-called "Rowland ghosts", faint sidebands (diffracted beams) accompanying each of the fundamental peaks (direct beams). An image of the diffraction grating resulting from a combination of a single direct beam and its companion diffracted beams exhibits a banded pattern, an interference effect. Zernike's key observation was that the Rowland ghosts had a phase difference of $\pi/2$ relative to the direct beam, and therefore, the resulting intensity expressed only a second order modulation arising from the vector addition of the components. This insight led him to the idea that a large enhancement of the interference effect would be realized if the relative phase between the diffracted beams and the direct beam could be modified by $\pi/2$ to produce an image with variations of first order in the diffracted components. Utilizing a method of etching glass developed by Lord Rayleigh, Zernike created an optical element, which he called a "phase strip", composed of a glass plate with a groove of depth $\lambda/2$. In this system, both the direct beam and the diffracted beams pass through the glass, so that the required groove depth to achieve a $\pi/2$ phase shift is a function of the index of refraction of the glass, typically $N_{glass} \approx 1.5$ at optical wavelengths. When the direct beam was focused precisely in the groove, it's phase was retarded by $\pi/2$ relative to the diffracted beams. The resulting image showed clearly the imperfections in the grating.

Applied to the study of plasmas, the phase contrast technique produces images of electron density waves, effective diffraction gratings for the incident beam. This method has been successfully applied on a number of tokamaks, first on TCA by Henry Weisen [48, 49], where one of its early applications was the measurement of the density perturbations from the damping of launched Alfvén waves from which the current distribution was inferred [17]. A phase contrast imaging system was installed on Alcator C-Mod in 1999 [34], and has operated regularly since then. Additional commentary on the history of phase contrast imaging of tokamak plasmas can be found in this same reference. This section presents the theory of diffraction from phase gratings, proceeding to the model of a plasma diffraction grating, and finally to the diagnostic implementation on Alcator C-Mod and its calibration systems.

2.2.1 The Plasma Diffraction Grating

As a development of the theoretical basis of phase contrast imaging, we examine the illustrative case of a one-dimensional diffraction grating, based on similar discussions in Refs. [34, 50]. In the following we use "wave" to refer to the collective structure of the electric field, and distinguish this from a "beam" which refers to a particular directional component of the wave. In principle, the technique of imaging density perturbations in a plasma is the same as Zernike's images of the imperfections in a diffraction grating created from the direct beam and the Rowland ghosts. We will see how the light wave leaving the plasma may be represented as a strong direct beam accompanied by weak diffracted beams which are out of phase (in mean) by $\pi/2$ relative to the direct beam. Before we reach the details of the calculations it will not hurt to emphasize a simple, but essential, detail of the technique: the $\pi/2$ phase difference which is central to the technique arises from the fact that the bending, or diffraction, of the incident beam is due the retardance or advancement of phase imposed on the incident beam by the variation in the index of refraction. It is not the case that the $\pi/2$ phase difference between the direct beam and the diffracted beams is the result of these components traversing different paths, such an effect effectively counteracts the phase contrast technique.

The following analysis treats the electric field as a scalar, an approximation justified in the limit of small scattering angle where the variation in the vector will enter as a correction of $\cos\theta$, where θ is the angle of propagation relative to incidence. For small θ, the corrections are of order θ^2 and may be ignored. In this limit, it is convenient to use the Huygens' superposition of wavelets to determine the wavefronts [29]. The Huygens' model represents each point in space as a source which radiates spherical waves, preserving the incident phase. The representation of the outgoing wave in terms of a direct beam and diffracted beams allows a reduction of the problem of wave propagation to that of geometric optics, with the additional accounting of the relative phases of the separate component beams.

Four approximations are made in the subsequent analysis: ideal phase grating, small angle scattering, thin scattering volume, and one-dimensional variation. Before proceeding, we qualify each of these approximations.

- <u>Ideal phase grating</u>: The ideal phase grating does not absorb or reflect any energy from the incident wave, which is equivalent to saying that the transmission coefficient has a complex phase with unit magnitude. For a wave passing through a region of free electrons, the total scattered power along a ray is approximated by $\epsilon_0 E_0^2 \sigma_e \int n_e dz$, where σ_e is the Thomson scattering cross section equal to $(8\pi/3)r_e^2$ where $r_e \approx 3\times10^{-15}$ m is the classical electron radius, and the integral of n_e is over the beam path [51]. Using a typical density of $10^{20}\mathrm{m}^{-3}$ we have a fractional radiated power of about 10^{-9}, validating the approximation of the plasma as an ideal phase object.

- Small angle scattering: Wave diffraction from an ideal phase grating is equivalent to a spatial variation in phase of the outgoing electric field at the surface of the grating. The spatial variation in phase can be found by integrating $\int k(\mathbf{r})\,\mathrm{d}z$ where z is the coordinate along the beam path. At infrared frequencies, the phase variations due to the plasma fluctuations are of order 10^{-2} or less, resulting in a very small scattering angle, justifying the use of the scalar representation of the electric field. Diffraction by phase variations is illustrated in Fig. 1-4.

- Thin scattering volume: The phase contrast system is designed around an ideal phase shift of $\pi/2$ between the direct and diffracted beams. In order for the technique to work, it is imperative that the direct and diffracted beams traverse the same background plasma so that their phase accumulation from the background plasma can be effectively subtracted during image formation. This is possible when the angle between the direct and diffracted beams is small enough. A “thin” object is one in which the scattering from all layers may be considered collectively as originating from a single surface. The direct and diffracted components begin to experience significant differences in plasma structure when their paths deviate from each other by a distance of approximately $1/k_p$, where k_p is the wavenumber of a plasma fluctuation. Using

$\theta_{scattering} = \lambda_0/\lambda_p$, we have that the separation between the top and bottom of the plasma should be no more than $L < \lambda_p^2/2\pi\lambda_0$. For the shear Alfvén waves, $\lambda_p \sim 6$ cm, giving $L < 60$ m, a value well within the limits of the optical configuration for Alcator C-Mod which has plasmas approximately 60 cm in height. As noted in Ref. [34], the maximum detectable wavenumber beyond which the plasma must be considered "thick" (also known as scintillation) corresponds to about $k_{max} \sim 10\,\text{cm}^{-1}$ ($\lambda \sim 0.6\,\text{cm}$). The plasma waves of interest for this work have wavenumbers well below this limit, on the order of $1\,\text{cm}^{-1}$.

- One-dimensional variation: The vertical port window through which the PCI laser beam passes is approximately 18.5 cm in the radial direction by 3.5 cm in the toroidal direction. Given that the beam can only sample about 3 cm of the plasma in the toroidal direction and that toroidal wavelengths are generally much larger than the radial or poloidal wavelengths, the plasma is effectively uniform along the toroidal direction. Combined with the thin object approximation, toroidal uniformity across the viewing window means that the plasma may be considered a one dimensional object.

To begin, we consider a plane wave traveling in the $+\hat{z}$ direction incident on a one-dimensional phase grating located at $z = 0$ with variation in the $\hat{x}$ direction. Let the grating have a complex valued transmission coefficient $\tau(x) = e^{i\delta(x)}$, representing and ideal phase grating. Note that the function τ describes the modification of the electric field, not the intensity. Modeling our phase object as a delta function grating at $z = 0$, the electric field of the outgoing wave at the surface of the grating becomes $E(x) = \tau(x)\, E_0$, where E_0 is the electric field of the spatially uniform incident wave, where without loss of generality, the incident wave has a phase of zero at the grating plane.

Consider an ideal phase grating whose phase variation in the $\hat{x}$ direction can be approximated by a finite Fourier representation of the form

$$\delta(x) = \sum_p \Delta_p \cos\left(k_p x - \omega_p t + \phi_p\right), \tag{2.1}$$

where p is a summation index and the ω_p and k_p are the angular frequencies and wavenumbers of the plasma perturbations. The ϕ_p term is a general phase required for Fourier decomposition in this form. We may expand τ in powers of Δ_p,

$$\begin{aligned} \tau &= 1 + i\sum_p \Delta_p \cos\left(k_p x - \omega_p t + \phi_p\right) + \mathcal{O}\left(\Delta^2\right) & (2.2)\\ &= 1 + \frac{i}{2}\sum_p \Delta_p \left[e^{i[k_p x - \omega_p t + \phi_p]} + e^{-i[k_p x - \omega_p t + \phi_p]}\right] + \mathcal{O}\left(\Delta^2\right). & (2.3) \end{aligned}$$

When $|\Delta_p| \ll 1$ for all p we may neglect the $\mathcal{O}(\Delta^2)$ terms. With this approximation, τ has the simple interpretation of a direct ($k = 0$) component plus a set of traveling waves. The time dependent, outgoing electric field can now be simply expressed as the product of τ and $E_0 e^{-i\omega_0 t}$, where ω_0 is the frequency of incident wave. That is,

$$E(x,t) = E_0 e^{-i\omega_0 t} + \frac{iE_0}{2}\sum_p \Delta_p \left[e^{i[k_p x - (\omega_0 + \omega_p)t + \phi_p]} + e^{i[-k_p x - (\omega_0 - \omega_p)t - \phi_p]}\right]. \tag{2.4}$$

We see now that the incident plane wave couples to each of the traveling plasma waves in τ to produce an outgoing system composed of a direct beam (first term on the RHS of Eq. 2.4) and a set of diffracted beams. The diffracted beams have a mean phase which is shifted by $\pi/2$ relative to the direct beam. It is tempting to consider this effect from the single particle point of view. Recall however, that

$E_{rad} \propto a$ and $a \propto E_{in}$ for a free charge so that the radiated electric field is in phase with the incident wave. The answer to this conundrum is that the resultant electric field in Eq. 2.4 arises from a spatial *variation* of phase and is ultimately a collective phenomenon, as illustrated in Fig. 1-4. In the phase contrast method, the phase at any particular point is meaningful only in relation to the other phases in the object. Indeed, a transmission grating does not exhibit this effect and cannot be imaged effectively with the phase contrast technique [26]. The meaning of this mysterious phase shift is apparent when we remember that the model of a direct beam plus two diffracted beams is a convenient representation of an outgoing wave whose spatially dependent phase has been advanced or retarded by the phase grating. In a phasor representation, the outgoing wave is equivalent to a superposition of the direct beam plus a small perturbation out of phase with the incident beam by $\pi/2$, an effect illustrated in Fig. 2-3. Alternatively, a small phase shift (δ) in a sine wave may be approximated by $\sin(\theta+\delta) \approx \sin(\theta)+\delta\cos(\theta)$, which shows that the term proportional to δ is out of phase with the main wave by exactly $\pi/2$.

The linearity of Maxwell's equations in vacuum makes no distinction between propagation of the collection of beams as in Eq. 2.4, or a superposition of the separate components individually propagated. The latter approach allows us to consider the trajectory of the diffracted components of Eq. 2.4 on their own. Let us isolate a single conjugate pair from Eq. 2.4, call this E_p, and look at its propagation along $\hat{z}$. Requiring that $|\mathbf{k}| = \omega/c$ in vacuum, we have that $k_z = \sqrt{k_0^2 - k_p^2}$, where $k_0 = \omega/c$ is the free space wavenumber, with the result that

$$E_p(x,z,t) = \frac{iE_0}{2}\Delta_p \left[e^{i[k_p x + k_z z - (\omega_0+\omega_p)t + \phi_p]} + e^{i[-k_p x + k_z z - (\omega_0-\omega_p)t - \phi_p]}\right]. \tag{2.5}$$

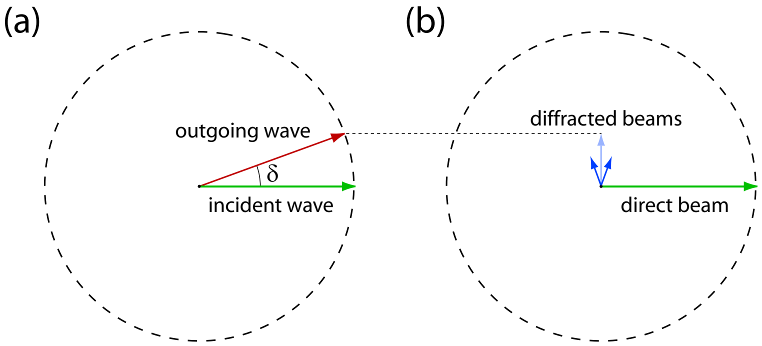

Figure 2-3: (a) A perturbation in the index of refraction changes the phase of the incident wave by δ. The outgoing wave may be approximated as (b) the superposition of a direct beam plus two diffracted beams which have a mean phase shift of $\pi/2$ relative to the direct beam. This model is only illustrative and does not represent an actual measurement.

It is now apparent that the incident wave couples to the plasma waves, conserving energy and momentum as seen by the selection rules for the diffracted waves: $\omega_{diffracted} = \omega_0 \pm \omega_p$ and $\mathbf{k}_{diffracted} = \pm k_p \hat{x} + k_z \hat{z}$. The angle of propagation relative to incidence ($\hat{z}$) is given by $\theta_{diffraction} = \pm k_p / k_z$. Considering plasma waves in the limit required for the thin object approximation, we may neglect the contribution of k_p to k_z and arrive at $\theta = \pm\lambda_0/\lambda_p$, where λ_0 is the incident laser wavelength and $\lambda_p = 2\pi/k_p$. When the frequency of the incident wave is sufficiently high that this light-like treatment of the waves in the plasma is justified, we have $\lambda_0 \ll \lambda_p$ and the scattering angle is indeed very small.

We may consider now the effect of image formation using these beams. If the diffracted and direct beams are imaged on a detector without any manipulation of phases, the electric fields from the diffracted beams will contribute in the following manner,

$$\begin{aligned} I_{image} &= \epsilon_0 |E(x)|^2 = \epsilon_0 |E_0 + \frac{iE_0}{2} \sum_p \tilde{\Delta}_p \,|^2 \\ &\approx \epsilon_0 E_0^2 \left[1 + \frac{1}{4} \sum_p \sum_l \tilde{\Delta}_p \, \tilde{\Delta}_l \, \right], \end{aligned} \tag{2.6}$$

where now j and l are dummy indices for the summations and for shorthand we have used $\tilde{\Delta}_p$ in place of $\Delta_p \left[e^{i[k_p x + k_z z - (\omega_0 + \omega_p)t + \phi_p]} + e^{i[-k_p x + k_z z - (\omega_0 - \omega_p)t - \phi_p]} \right]$. Equation 2.6 shows that the result of imaging the direct beam plus diffracted beams without manipulation results in a second order dependence on the small quantity $\tilde{\Delta}$, and furthermore, is highly nontrivial to interpret when multiple Fourier components are present. However, if the phase of the direct beam is advanced by $\pi/2$, that is $E_0 \rightarrow e^{i\pi/s} E_0 = iE_0$, we have the essence of the phase contrast imaging technique. The intensity of the image in the phase contrast method is

$$\begin{aligned} I_{PCI} &= \epsilon_0 |E(x)|^2 = \epsilon_0 |iE_0 + \frac{iE_0}{2} \sum_p \tilde{\Delta}_p \,|^2 \\ &\approx \epsilon_0 E_0^2 \left[1 + \sum_p \tilde{\Delta}_p \, \right]. \end{aligned} \tag{2.7}$$

The phase contrast technique transforms small variations of phase into linear intensity variations. Recalling that $\sum_p \tilde{\Delta}_p$ is just the Fourier transform of τ, the phase contrast method produces an image of the phase grating. In the implementations of this method for plasma physics, the optical component which modifies the phase of the direct beam is called a "phase plate", the practical equivalent of Zernike's phase strips. It has been found that a reflective phase plate, rather than a transmissive one, is preferable for these studies. In essence the phase plate is a glass substrate with a highly reflective gold or aluminum surface, except for a groove along a diameter of the surface which reveals the substrate. The depth of the groove is nominally $\lambda/8$ so that when the direct beam enters the groove and is reflected from the glass surface it travels an additional distance of $\lambda/4$, introducing a $\pi/2$ phase shift, while the diffracted beams reflect off of the surrounding surface. The phase contrast technique using this method is illustrated in Fig. 2-4, and the phase plates described in greater detail in section 2.2.4.

A further enhancement of the phase contrast method may be achieved if the phase plate also reduces the intensity of the direct beam. The particular substrate used in the present experiments is ZnSe, chosen for its fairly low cost and low coefficient of reflection at $10.6\,\mu$m, $R \approx 0.17$ (with respect to the intensity). Including this effect, the phase contrast technique becomes

$$I_{PCI+ZnSe} = \epsilon_0 R E_0^2 \left[1 + \frac{1}{\sqrt{R}} \sum_p \tilde{\Delta}_p \right]. \tag{2.8}$$

A ZnSe substrate enhances the phase contrast by about a factor of 2.4 over a purely reflective phase plate, though the overall intensity of the image is reduced. The net result however, is a significant increase in the signal to noise ratio for the system [34].

To conclude the discussion of phase gratings as a model for plasma perturbations, we need only to relate the coefficients Δ_p to a physical observable. The light source used for these studies is a $10.6\,\mu$m CO_2 laser, which has a frequency of approximately 28 THz, well above the plasma and electron cyclotron frequencies. In this regime, the appropriate dispersion relation is that of plasma light waves. Expressed in terms of the index of refraction, $N = ck/\omega$, the dispersion relation is $N^2 = 1 - \omega_{pe}^2/\omega_0^2$. The

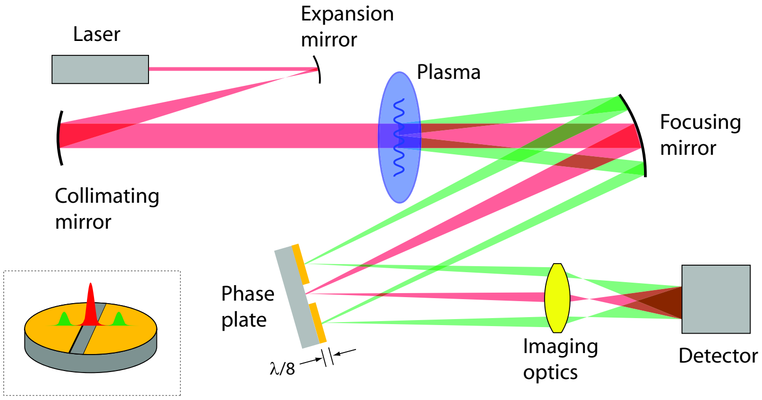

Figure 2-4: Schematic representation of the PCI system. The incident laser beam (red) is expanded, collimated and sent through the plasma. A plasma wave produces two diffracted beams (orange). The direct beam acquires a $\pi/2$ phase shift as it traverses the $\lambda/8$ groove in the phase plate. Finally, the beams are imaged onto the detector to produce a phase contrast image of the plasma wave.

index of refraction is a function of the plasma electron density, and hence, the phase contrast method is sensitive to perturbations in this quantity. The accumulated phase of the wave as it passes through the plasma is $\delta_{total}(x) = \int k(x,z)\,\mathrm{d}z$, equivalent to

$$\delta_{total}(x) = \frac{\omega_0}{c}\int N(x,z)\,\mathrm{d}z,$$

where the limits of integration are the boundaries of the plasma along a ray of the incident beam. Note that because we are operating in the limit of small scattering angle, a direct beam and the scattered beam traverse the same path through the plasma so that the retarded time may be neglected. When a density perturbation $(\tilde{n}_e)$ is present we have $N \rightarrow N_0 - \tilde{N}$, where N_0 is evaluated at the equilibrium density and $\tilde{N} = e^2\tilde{n}_e/\epsilon_0 m_e \omega_0^2$. Assuming that the background electron density profile changes sufficiently slowly in time and space, variations in these quantities can be ignored and the integral of $N_0 \, \mathrm{d}z$ adds a constant offset phase to δ_{total} with no consequence for the phase contrast technique. The information regarding the grating is carried in the density perturbations alone. Using a first order Taylor expansion of N around n_e, the final result is

$$\delta(x) = -r_e \lambda_0 \int \tilde{n}_e(x,z) \, \mathrm{d}z, \tag{2.9}$$

where we have used the classical electron radius, $r_e = \mu_0 e^2 / 4\pi m_e \sim 3 \cdot 10^{-15}$ m in MKS units ($r_e = e^2/m_e c^2$ in CGS units). When this integral is performed for each chord along the incident beam we have $\delta(x)$, which is related to the Δ_p coefficients by the Fourier transform of Eq. 2.1. The image created at the detector is proportional to $\int \tilde{n}_e \, \mathrm{d}z$.

A large plasma fluctuation might have $\tilde{n}_e / n_e \sim 10^{-2}$, which for Alcator C-Mod plasmas results in $\delta < 10^{-2}$ and validates the earlier assumption that the $\mathcal{O}(\Delta^2)$ terms can be ignored. The output signal depends largely on the specific structure of the density perturbations within the plasma. An interesting effect arises when the beam passes through regions of positive and negative density fluctuations leading to "phase cancelation", whereby the observed density fluctuation may be much lower than the peak fluctuation. This is an important effect in the study of Alfvén eigenmodes and will be discussed in greater detail in section 3.6 regarding the synthetic PCI analysis.

2.2.2 Phase Contrast Imaging on Alcator C-Mod

The PCI system implemented on Alcator C-Mod saw first operation in 1999 [34], and has been operating regularly since then. An overview of the PCI system in relation to the tokamak structure is shown in Fig. 2-5. All mirrors in the system are located external to the vacuum vessel, allowing for easy maintenance and operation, at least compared to other systems where mirrors must be mounted in-vessel as in, for example, the PCI system on the DIII-D tokamak [50]. The PCI beam path passes vertically through the plasma, including the core region, as shown in Fig. 2-5(b). One of the great advantages of the Alcator C-Mod design is that the system is sensitive to perturbations on all flux surfaces, at least for plasma waves which extend over a flux surface. This allows the PCI system to be used for the study of edge modes such as the quasi-coherent (QC) oscillation, modes in the core plasma such as the ion temperature gradient (ITG) driven turbulence, and core localized phenomena such as Alfvén eigenmodes [24].

The detector is composed of 32 photoconductive HgCdTe elements, with a ideal frequency range of 0−10 MHz. The signals are amplified at the detector with a gain of approximately 250 before being sent to digitizers capable of 40 MHz signal processing, though the standard operation uses 10 MHz digitization. With the acquisition of new phase plates multiple magnifications are possible, covering the range $0.5 - 60\,\mathrm{cm}^{-1}$. The new phase plates will be discussed in greater detail in the following section.

The transmitting table which houses the laser and expansion optics measures $3.04\,\mathrm{m} \times 0.91\,\mathrm{m}$, is shown in Fig. 2-6. The laser source is a 60 W Firestar CO_2 laser manufactured by Synrad. The laser is cooled by a closed system water supply at 20°C, regulated by a Merlin chiller located approximately 3 meters away. This water supply also cools the acousto-optical modulators (AOMs) used in the heterodyne detection of ICRF waves. These units are not used in the study of Alfvén eigenmodes and will not be discussed further. The $10.6\,\mu$m light from the laser is in the far infrared regime and not visible to the human eye. Alignment of the optics is performed with a 25 mW HeNe laser (λ = 632 nm). The HeNe and CO_2 laser beams are made coaxial through a mirror which is reflective at $10.6\,\mu$m but transparent in the visible

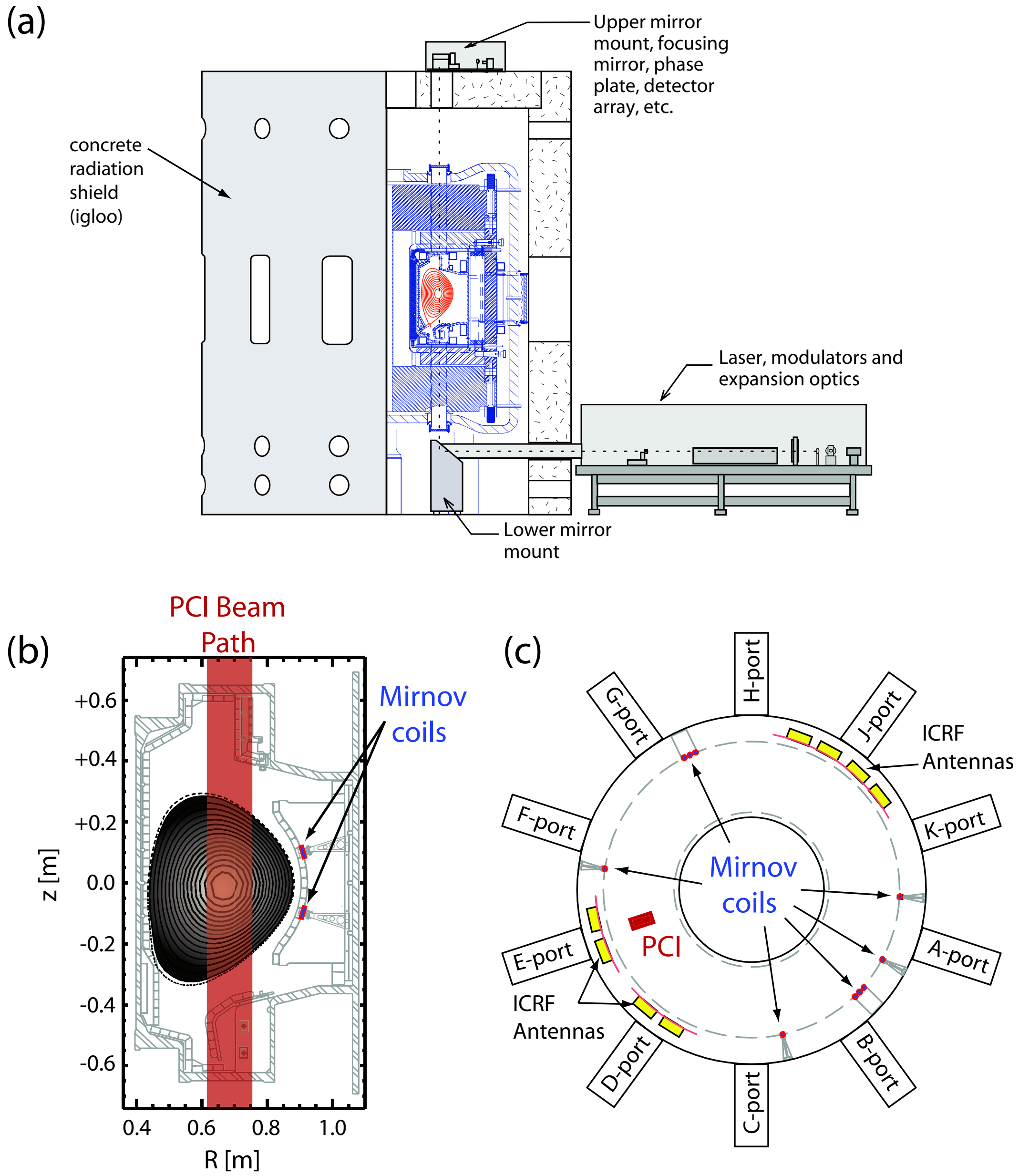

Figure 2-5: (a) The PCI transmitting and receiving tables in relation to the Alcator C-Mod superstructure, adapted from Ref. [34]. (b) A vertical cross section showing the path of the laser beam for the PCI system and the poloidal position of the Mirnov coils and (c) a plan view of the torus showing the positions of the PCI beam, the Mirnov coils, and the ICRH antennas.

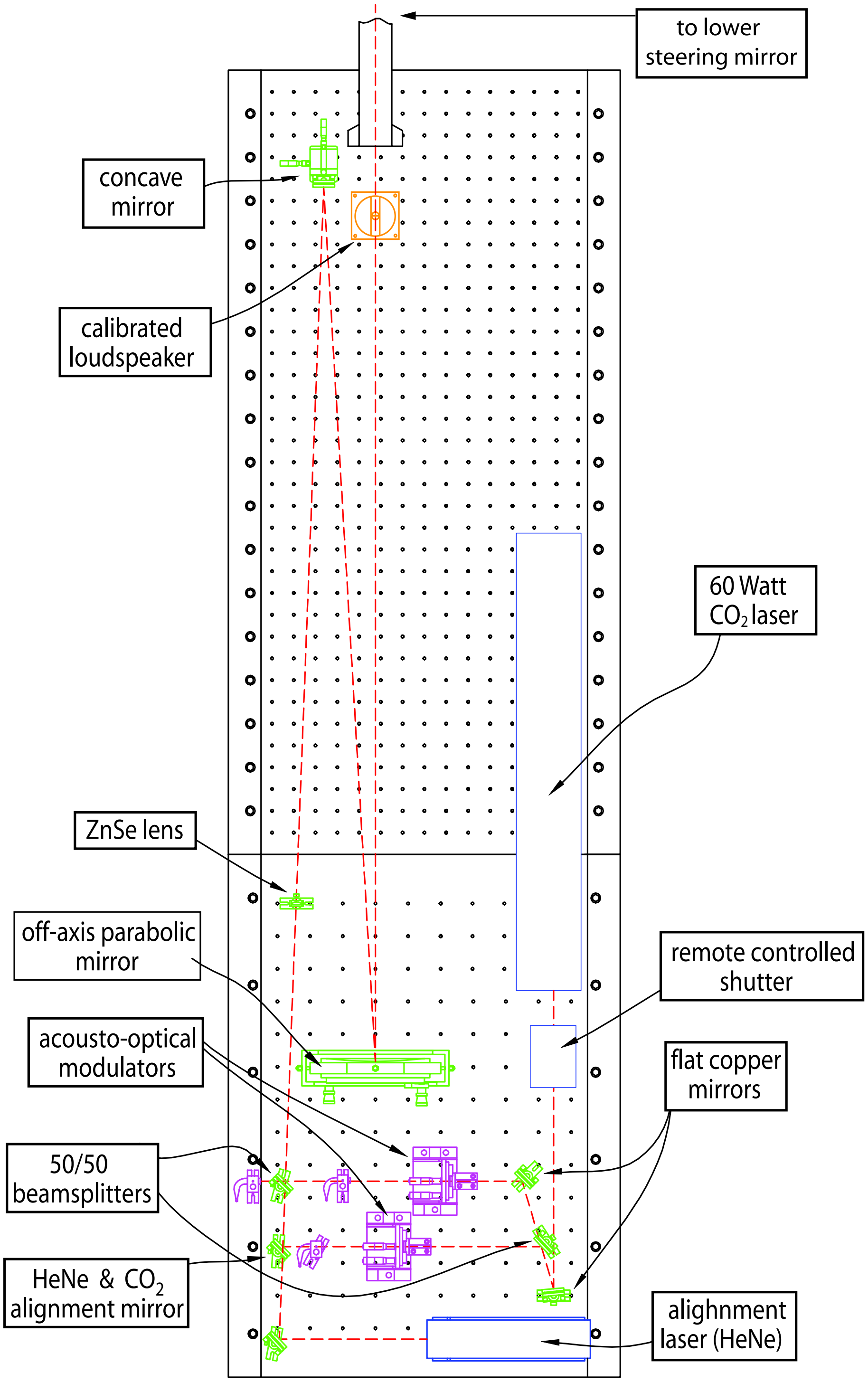

Figure 2-6: The PCI transmitting table layout, adapted from Ref. [34].

spectrum, allowing the HeNe beam to pass through and join the CO_2 beam. This element is labeled in Fig. 2-6 as the "HeNe & CO_2 alignment mirror".

For the study of Alfvén waves, a large beam width is desired to capture as much of the spatial extent of the eigenmodes as possible. In the dedicated experiments described in the following chapters, a $1/e$ beam width of approximately 20 cm was generated by using a 1 inch focal length concave mirror prior to collimation by the off-axis parabolic mirror. Studies requiring a higher k range often use the 2 inch focal length mirror to reduce the beam diameter by a factor of 2 and increase the intensity by a factor of 4. In the low-k configuration, a magnification giving a maximum k of approximately $8\,\mathrm{cm}^{-1}$ is used. The image region was typically about 10 cm wide so that the beam intensity was relatively uniform over this span. During these experiments, calibration was provided by a 15 kHz sound burst from the speaker.

2.2.3 PCI Calibration

As part of the original operation, a speaker was installed and configured to launch a 2 msec burst, at a frequency of 15 kHz, prior to each shot. The data acquisition system is configured to capture this event. Analysis of the sound burst signal can be analyzed to determine a calibration coefficient which scales the measured signal in terms of absolute density perturbations. The sound waves create pressure perturbations which are related to a density perturbation through an equation of state for air. As absolute fluctuation levels are not calculated by any of the codes used in this work, we focus on the use of the calibration system primarily as a relative calibration to account for channel-to-channel differences in the detector, alignment, and non-uniform beam profiles. The relative calibration factors derived from a gaussian fit to the experimental calibration amplitudes multiply the output of a synthetic

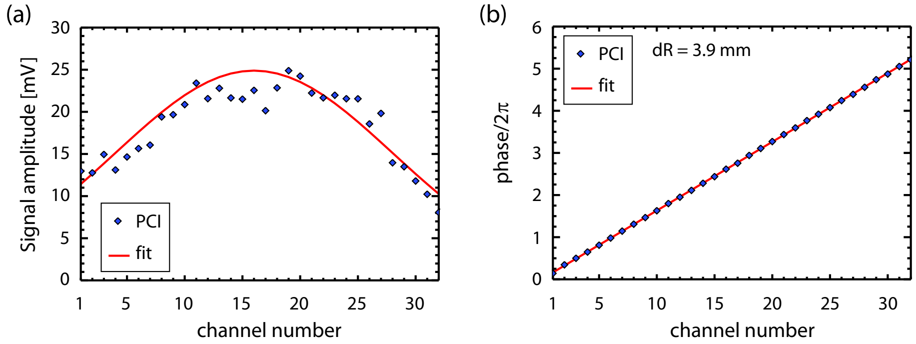

Figure 2-7: PCI measurements of the sound burst show (a) a nearly gaussian beam profile from which an absolute calibration is found and (b) phase measurements from which the channel spacing can be inferred.

diagnostic signal. This method is used, in contrast to dividing the experimental data by these values, so that the noise on low-signal channels is not amplified. Representative calibration curves are presented in Fig. 2-7.

The channel spacing can be derived from the measured phase of the sound waves. The phase difference between two channels separated by a distance dR normal to the wavefront is $\mathrm{d}\Phi = (\omega_{sb}/c_s)\,\mathrm{d}R$, where ω_{sb} is the frequency of the sound burst and $c_s = 344\,\mathrm{m/s}$ is the speed of sound in air at $25°C$. Inverting this equation for dR and using $\omega_{sb} = 2\pi \times 14.5$ kHz gives $\mathrm{d}R = (c_s/f_{sb})\,\mathrm{d}\Phi/2\pi \approx 24$ mm $\times\, \mathrm{d}\Phi/2\pi$. The sequence of phase measurement may be easily fit to this linear form to derive the chord spacing for the experiment.

2.2.4 Phase Plates

A new generation of phase plates was introduced to the experiment in 2008. The former generation of plates had been in service for many years and the surface quality of these pieces was showing signs of wear, and more importantly, they had a 1”

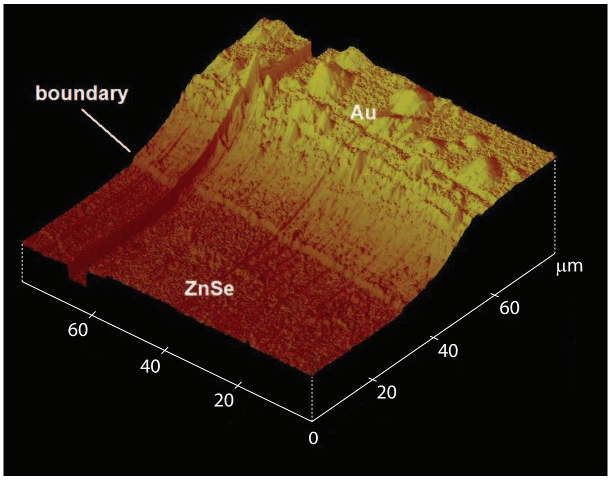

Figure 2-8: AFM surface scan of the older 1" diameter phase plate. A mean difference in height between the groove bottom and the reflective surface is 1.327 μm. The width of the transition zone (region between the groove bottom and flat surface of the reflective coating) is approximately 20 μm. The RMS surface height variation of the gold coating, away from the groove, is about 3 nm. The groove extending across the transition zone at approximately 65 μm is an error of the measurement device and not a real feature.

diameter substrate which limited the upper range of the detectable wavenumber to approximately 30 cm^{-1}. The search for high k turbulence motivated the development of new 2" diameter phase plates. Though the 2" diameter phase plates were not necessary for the experiments reported in this thesis, the author played a significant part in the development of these plates and some important details of their manufacture are recorded here.

Two instruments were used in the study of the surface quality of the phase plates: an atomic force microscope (AFM) [52] and a profilometer. Both instruments were rented on an hourly basis through the MIT Center for Materials Science and Engineering. While the AFM measurements reveal fine structure details of the surface quality, the utility of this instrument for testing phase plates is limited on account

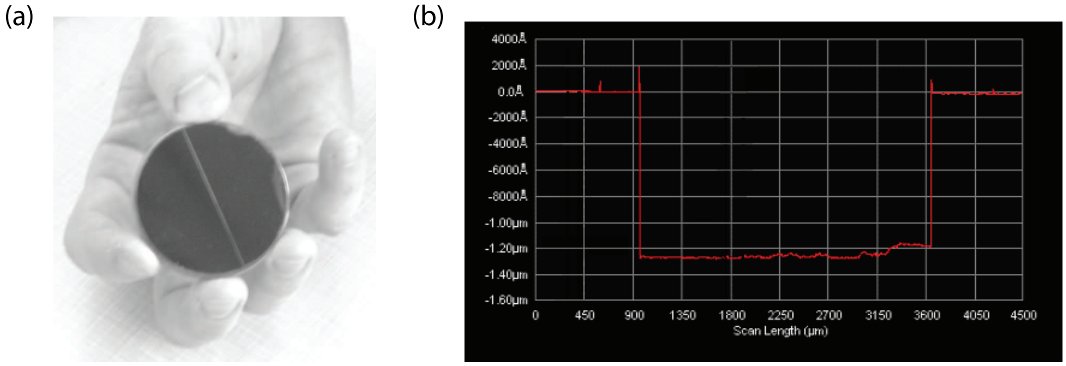

Figure 2-9: (a) A picture of a production piece with a 2.5 mm wide groove. (b) Profilometer measurements of the same piece showing a groove depth of 1.27 μm and a transition zone smaller than the instrument resolution.

of the small area accessible during a single scan. Figure 2-8 presents an AFM scan of the surface features of the older generation phase plate, showing the broad transition from the groove to the reflective surface. Later tests used a Tencor profilometer because of its ability to scan a range of up to 5 mm, though only in one dimension.

The new phase plates were manufactured by Bandwidth Semiconductor Inc. (now Spire Inc.) based out of Hudson, NH. The substrates, 2" diameter and 0.200" thick ZnSe windows, were purchased from II-VI Inc. An anti-reflective coating for 10.6 μm was applied to one side by the manufacturer. As in the former plates, ZnSe was selected for its desirable reflection coefficient at infrared wavelengths and moderate cost. To accommodate a range of optical configurations tailored to a particular k range, phase plates with different groove widths were manufactured. The final order of six parts was split between the Alcator C-Mod PCI group and the DIII-D PCI group. The Alcator C-Mod group ordered phase plates with groove widths of 0.4 mm, 1.1 mm, and 4.0 mm, and acquired a 2.5 mm plate from the initial R&D effort.

Former attempts to manufacture phase plates largely failed due to the inability to provide good adhesion of the gold coating to the ZnSe substrate. Tests performed at Bandwidth determined that a bonding layer was necessary to achieve good adhesion between the gold and the ZnSe. The final design used a 300 $\AA$ thick layer of SiO_2 on the ZnSe surface, followed by a 200 $\AA$ thick layer of titanium, capped with a 300 $\AA$ thick layer of platinum and finished with the gold coating. The design for the front-side coating specifies a nominal $\lambda_0/8$ groove depth at $1.32\,\mu$m (±10%). Measurement of the surface quality of the final production pieces with a profilometer showed that all final production pieces were well within the design specifications with groove depths of approximately $1.27\,\mu$m. A picture of a phase plate and a profilometer measurement of the groove profile are presented in Fig. 2-9. *In situ* tests of the phase plates show exceptional performance.

2.3 Mirnov Coils

Two sets of Mirnov coils in the Alcator C-Mod tokamak are designed for measuring the toroidal mode numbers of low-n MHD phenomena. One set is located at 10 cm above the midplane, and the other at 10 cm below the midplane. In the present system Mirnov coils are located at six toroidal locations, as illustrated in Fig. 2-5. In practice it is often the upper set which is used due to the better signal to noise ratio of those coils.

The response of the coils is generally highly non-linear as a function of frequency. A typical coil has 144 turns over four layers. The internal capacitance of such a design unfortunately introduces a coil resonance near 750 kHz. Away from the resonance, we may take the coils to have an approximate linear response function over a small enough region. To account for the resonant effect, we relate the output voltage to the magnetic field through

$$\frac{V_{out}}{NA\omega\tilde{B}} = -iH(\omega), \tag{2.10}$$

where N is the number of turns of the coil, A is the effective cross sectional area of a single turn, and $\tilde{B}$ is the fluctuating magnetic field we want to measure. Assuming all coils have nearly similar response functions with regard to phase relationships, we may take the modulus of Eq. 2.12. The function $|H(\omega)|$ may be modeled by a Lorentzian form,

$$|H(\omega)| = \frac{\omega_0^2}{\left[\left(\omega^2 - \omega_0^2\right)^2 + 4\gamma^2\omega^2\right]^{1/2}}, \tag{2.11}$$

where $\omega_0 = 1/LC$ and $\gamma = LR$, and L is the coil self-inductance, C is the self-capacitance, and R is the coil resistance. Numerically, $\omega \approx 2\pi \times 750\,\mathrm{kHz}$ and $\gamma \approx 2\pi \times 100\,\mathrm{kHz}$. We may invert this relationship to solve for $\tilde{B}$ in terms of the output voltage,

$$\tilde{B} = \frac{V}{\omega_0 NA}\, G(\omega). \tag{2.12}$$

In this last form we have defined a function $G(\omega) = (\omega_0/\omega)H^{-1}$. The functions $H(\omega)$ and $G(\omega)$ are shown in Fig. 2-10, where instead of ω we have used $f = 2\pi\omega$ as the abscissa. The function $G(\omega)$ shows that the coil response may change significantly over the range of $(200 - 600)\,\mathrm{kHz}$, so that it is necessary to include these calibration factors in the calculations when determining the absolute fluctuation level, or even a relative change in fluctuation level between two frequencies.

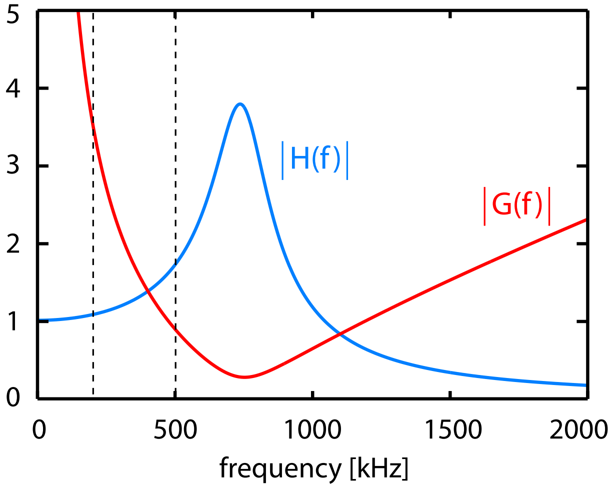

Figure 2-10: The frequency response curve for the Mirnov coils exhibits a resonance near $f = 750\,\mathrm{kHz}$. The measurements of interest in this work occur in the region of approximately $200 - 600\,\mathrm{kHz}$.

Chapter 3

Alfvén Waves

The study of Alfvén waves in this thesis follows two major approaches: excitation in tokamak plasma experiments and modeling by way of numerics and theory. The meeting of these two branches occurs through the development and application of a "synthetic", or simulated, PCI diagnostic. The former chapter discussed the diagnostics. This chapter defines the theoretical basis for interpretation of the observations and the development of tools for comparing theory to experiment, namely, the synthetic PCI.

Beginning with a simple slab geometry and progressing to toroidal geometry, this chapter develops a model of Alfvén eigenmodes from ideal MHD theory. This work focuses on a particular class of Alfvén eigenmode, the reversed shear Alfvén eigenmode (RSAE) [6, 7, 8, 9] which is localized to a region near a maximum in the current density profile. We will see that the eigenmodes appearing in slab geometry present many of the fundamentals which appear in toroidal geometry, but do not contain the essential physics required for instability. The topics of mode frequency, spatial structure, growth and damping will be discussed separately. Ultimately, the complex mathematics imposed by toroidal geometry requires advanced numerical tools for the solution of the eigenmodes. The final section of the chapter will be devoted to the discussion of the synthetic PCI analysis which is the fulcrum of comparison of the spatial structures from simulations and experiments.

3.1 Alfvén waves in the MHD model

In homogeneous plasmas, low-frequency ideal MHD waves can be represented as superpositions of two characteristic branches: the shear Alfvén wave and the magnetosonic wave. Unlike the magnetosonic branch, the shear Alfvén wave is nearly incompressible, meaning that the perturbations to the magnetic energy and internal energy of the plasma enter in second order [53]. The following system of equations comprise the basis for analysis of ideal MHD modes, where in the following γ is the adiabatic index.

$$\frac{\mathrm{d}}{\mathrm{d}t}\rho\mathbf{v} = \mathbf{j}\times\mathbf{B} - \vec{\nabla}p \qquad \text{momentum equation} \tag{3.1}$$

$$\nabla\times\mathbf{B} = \mu_0\mathbf{j} \qquad \text{Ampere's Law} \tag{3.2}$$

$$\nabla\times\mathbf{E} = -\frac{\partial}{\partial t}\mathbf{B} \qquad \text{Faraday's Law} \tag{3.3}$$

$$\mathbf{E} + \mathbf{v}\times\mathbf{B} = 0 \qquad \text{Ohm's Law} \tag{3.4}$$

$$\frac{\mathrm{d}}{\mathrm{d}t}\rho + \nabla\cdot(\rho\,\mathbf{v}) = 0 \qquad \text{continuity} \tag{3.5}$$

$$\frac{\mathrm{d}}{\mathrm{d}t}\left(\frac{p}{\rho^\gamma}\right) = 0 \qquad \text{equation of state} \tag{3.6}$$

The displacement current in Ampere's Law is neglected with the limitation that

$v_{phase}^2 \ll c^2$, which is well satisfied for the modes of interest. The absence of finite Larmor radius (FLR) corrections signifies that the frequencies of concern are restricted the regime $\omega \ll \omega_{ci}$ and $k_\perp \rho_i \ll 1$, where $\rho_i = \sqrt{T_i/m_i}/\omega_{ci}$ is the ion Larmor radius. In the ideal MHD limit, the $\mathbf{E} \times \mathbf{B}$ drift dominates the plasma motion, where $\mathbf{E}$ arises predominantly from an electromagnetic source. In the following analysis, we expand these equations to first order in the perturbed quantities (see Ref. [36] for a more complete description of this technique) and perform a Fourier decomposition of the quantities. The particular form of the Fourier decomposition depends on the geometry of the problem, hence in the first step we take only the temporal Fourier representation, that is, $\partial/\partial t \to -i\omega$. In making these expansions we assume that there is no zeroth order velocity, a good approximation for core-localized modes. With a change of variables from the fluid velocity to the fluid displacement via $\mathbf{v} = -i\omega\boldsymbol{\xi}$, using Ampere's Law to remove $\mathbf{j}_1$ and Faraday's Law to remove $\mathbf{E}_1$, and employing standard vector identities, equations 3.1 through 3.6 are reduced to the following set of four first order equations,

$$\begin{aligned}
-\mu_0\rho\omega^2\boldsymbol{\xi} &= (\mathbf{B}_1 \cdot \boldsymbol{\nabla})\mathbf{B}_0 + (\mathbf{B}_0 \cdot \nabla)\mathbf{B}_1 - \nabla(\mathbf{B}_0 \cdot \mathbf{B}_1 + \mu_0 p_1) && (3.7)\\
\mathbf{B}_1 &= -(\boldsymbol{\xi} \cdot \nabla)\mathbf{B}_0 + (\mathbf{B}_0 \cdot \nabla)\boldsymbol{\xi} - \mathbf{B}_0(\nabla \cdot \boldsymbol{\xi}) && (3.8)\\
\rho_1 &= -(\boldsymbol{\xi} \cdot \nabla)\rho_0 - \rho_0(\nabla \cdot \boldsymbol{\xi}) && (3.9)\\
p_1 &= -(\boldsymbol{\xi} \cdot \nabla)p_0 - \gamma p_0(\nabla \cdot \boldsymbol{\xi}), && (3.10)
\end{aligned}$$

where the subscript "0" refers to the equilibrium and the subscript "1" refers to the first order perturbation. Notice that the density perturbations, essential for detection with PCI, arise only with finite density gradient or fluid compression. The presence of the magnetic field and a pressure gradient perpendicular to the magnetic field define a natural coordinate system: $\hat{\mathbf{b}}_\parallel = \mathbf{B}/|\mathbf{B}|$, $\hat{\mathbf{r}} = \vec{\nabla} p/|\vec{\nabla} p|$, and $\hat{\mathbf{b}}_\perp = \hat{\mathbf{b}}_\parallel \times \hat{\mathbf{r}}$. It is typical to decompose the wave vector into components parallel to the field, $\mathbf{k}_\parallel = (\mathbf{k} \cdot \hat{\mathbf{b}}_\parallel)\hat{\mathbf{b}}_\parallel$, and perpendicular to the field, $\mathbf{k}_\perp = (\mathbf{k} \cdot \hat{\mathbf{b}}_\perp)\hat{\mathbf{b}}_\perp$. Even though $k_\parallel^2/k_\perp^2 \ll 1$, it is critical that terms of this order be retained in the analysis of the shear Alfvén waves. The limit $k_\parallel \to 0$ is more subtle than the case of finite $k_\parallel$, requiring consideration of finite $\nabla \cdot \boldsymbol{\xi}$ and is not considered here.

Before proceeding to specific application of this system of equations, it is worthwhile to comment on the importance of compressibility in relation to wave stability. Mathematically, incompressibility amounts to taking $\nabla \cdot \boldsymbol{\xi} = 0$, which is formally derived by taking the limit $\gamma \to \infty$, where γ is the adiabatic index (see Eqs. 3.6 and 3.10). Physically, the most unstable modes are those which respond with incompressible motion [36]. The following argument illustrates this point. The energy density of a wave is an important parameter in considering its stability in relation to accessible free energy sources. Including the first order perturbations from a wave, the magnetic energy density is proportional to $B^2 = B_0^2 + B_1^2 + 2\mathbf{B}_0 \cdot \mathbf{B}_1$. Clearly then, the wave energy is carried by the second two terms on the RHS. Assuming that a strong guide field is present, as is the case in tokamak plasmas, the wave energy becomes a second order quantity in the perturbation when $\mathbf{B}_0 \cdot \mathbf{B}_1 = 0$. Consider a cylindrical system with a strong guide field in the $\hat{z}$ direction as an approximation to the tokamak. The first order perturbation of B_z is composed of three parts,

$$B_{1,z} = -\xi_x \frac{\partial}{\partial r} B_z + i k_\parallel B \xi_z - B_z(\nabla \cdot \boldsymbol{\xi}), \tag{3.11}$$

where $k_\parallel = (\mathbf{k} \cdot \mathbf{B})/B$ is the magnitude of the parallel wave vector. The first term represents the compression of the guide field due to its non-uniformity, which is small for low β plasmas, where $\beta = 2\mu_0 p_0/B^2$ is the ratio of the plasma pressure to magnetic pressure, and furthermore, tends to cancel with other terms in $\mathbf{B}_0 \cdot \mathbf{B}_1$ and can be ignored. The second term accounts for the compression of the plasma due to parallel fluid displacement and is small when ξ_z is small compared to ξ_x. It can be shown that $\xi_z \approx (ik_z/k_y^2)\xi_x'$, so that typically $\xi_z \ll \xi_x$ as $k_z/k_y \sim 0.1$ in magnitude. Using the result that $B_{1,x} = ik_\parallel B\xi_x$ and $\xi_x' \sim k_y\xi_x$, we have that the second term scales as $(k_z/k_y)B_{1,x}$ so that it is effectively a quantity of second order and can be ignored. The only term with a possibility of contributing in first order is the third term, proportional to $\nabla \cdot \boldsymbol{\xi}$. Hence, the wave energy is minimized when $\nabla \cdot \boldsymbol{\xi}$ is minimized, which is the original statement we sought to prove. We have only to show that the incompressible approximation is justified for the shear Alfvén waves. Using a slab geometry to derive the rough scaling of compressibility by eliminating ξ_y and ξ_z in favor of ξ_x, we have

$$\nabla \cdot \boldsymbol{\xi} \approx \frac{-1}{1+\gamma\beta}\left[\frac{B_y}{B} + \frac{k_\parallel^2}{k_y^2}\frac{\omega^2 - \omega_A^2}{\omega_A^2}\right]\frac{\partial}{\partial x}\xi_x, \tag{3.12}$$

where $\omega_A^2 = k_\parallel^2 v_A^2$. As stated before, the vanishing of $\nabla \cdot \boldsymbol{\xi}$ in the limit $\gamma \to \infty$ is now apparent. Notice however, that the term in brackets in Eq. 3.12 is small so that $\nabla \cdot \boldsymbol{\xi}$ can only be significant when $\mathrm{d}\xi_x/\mathrm{d}x$ becomes large. The summary point is that the wave energy increases to a quantity of first order from second order when the gradients of the fluid displacement become large, which occurs approximately for $(\mathrm{d}/\mathrm{d}x)\ln\xi_x > k_y$. An increase in the wave energy can be thought of as an increase in the effective damping rate [54]. Additionally, mode conversion to short wavelength electrostatic waves occurs near resonant layers and contributes directly to wave damping [55, 56, 57]. As we will see in the following sections, large gradients in the displacement result when the eigenmode encounters a resonance in the plasma.

To briefly forecast the results of the subsequent analysis, the waves of greatest interest to this body of work are the shear Alfvén waves which are characterized by dominant fluid displacements in a direction perpendicular to the magnetic field such that $\mathbf{B}_0 \cdot \mathbf{B}_1 \approx 0$. While this term is near zero, it cannot be exactly zero, and it is this small remainder which determines the shape of the shear Alfvén eigenmodes. In particular, incompressible motion requires a displacement in the $\hat{y}$ direction, or equivalently the poloidal direction, which means that there will be some first order magnetic perturbation parallel to B_y. Recalling the discussion from chapter 1, we will see the mathematical development for the formation of the Alfvén eigenmodes around regions of maxima in the Alfvén continuum.

3.2 Slab Geometry and the definition of the Alfvén continuum

A homogenous slab plasma with a background magnetic field permits two electromagnetic wave branches. There are the additional electrostatic waves, such as the ion sound wave, but those do not concern us here. The directions perpendicular to the magnetic field are degenerate, and thus we need to specify only a $k_\perp$ and $k_\parallel$ to fully described the waves. Keeping only the leading terms, the two branches are,

$$\omega^2 = k_\parallel^2 v_A^2 \qquad \text{shear Alfvén wave} \tag{3.13}$$

$$\omega^2 = k^2 v_A^2 \qquad \text{magnetosonic wave} \tag{3.14}$$

where $k_\parallel = (\mathbf{k} \cdot \mathbf{B})/B$ is the wave vector parallel to the magnetic field, $v_A^2 = B^2/\mu_0 \rho$

is the Alfvén speed, B is the modulus of the magnetic field, μ_0 is the permeability of free space, and ρ is the mass density. For the remainder of the analysis, we will neglect the magnetosonic wave and focus on the shear Alfvén wave branch.

The degeneracy of the homogenous case is broken by including spatially varying equilibrium profiles, which in the examples presented here will be in the $\hat{x}$ direction as shown in Fig. 3-1. The most relevant case for modeling a tokamak plasma includes the possibility of spatially varying density and magnetic field profiles. A sheared magnetic field in slab geometry can be represented as $\mathbf{B} = B_0\hat{z} + B_y(x)\hat{y}$. As described in the first section of this chapter, wave energy is minimized when the dominant displacement is perpendicular to the equilibrium magnetic field, which in this case is the $\hat{x}$ direction. It then follows from Ohm's Law that $\mathbf{E}$ is dominantly in the $\hat{y}$ direction, and from Faraday's Law that $\mathbf{B}_1$ is dominantly in the $\hat{x}$ direction. In deriving the following relation for ξ_x with eigenvalue ω^2 we have used the incompressible approximation and also $|\xi_z|/|\xi_x| \ll 1$ to eliminate ξ_z from the outset. This also decouples the density perturbation (Eq. 3.9) from the Eqs. 3.7 and 3.8, resulting in the second order differential equation,

$$\rho(\omega^2 - \omega_A^2)\xi_x = \frac{\partial}{\partial x}\left(\frac{\rho(\omega^2 - \omega_A^2)}{k_y^2}\frac{\partial}{\partial x}\xi_x\right), \tag{3.15}$$

where as before $\omega_A^2 = k_\parallel^2 v_A^2$. Note that the terms on the RHS of Eq. 3.15 arise from the $\nabla \cdot (\mathbf{B}_0 \cdot \mathbf{B}_1)$ term in Eq. 3.7, showing that the departure from an ideal shear Alfvén wave ($\mathbf{B}_0 \cdot \mathbf{B}_1 = 0$) is essential to the formation of Alfvén eigenmodes. Equation 3.15 has singular points where the coefficient of the highest derivative vanishes, which occurs when $\omega^2 - \omega_A^2 = 0$. While the singularity may be resolved by considering physics neglected in this derivation, possibly including effects outside of the ideal MHD model [55], it nonetheless describes the dominant trend of the solutions and

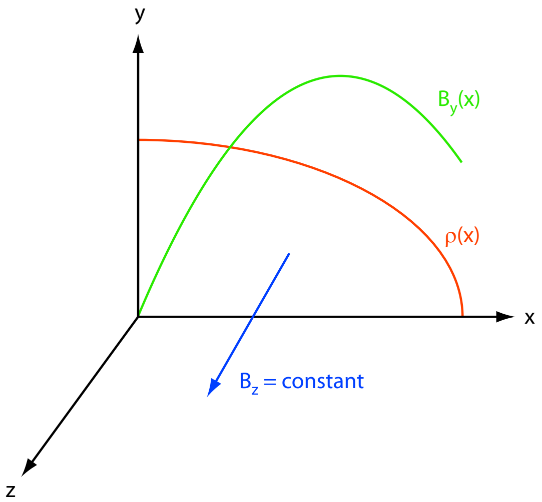

Figure 3-1: The slab geometry model has B_y and ρ profiles with spatial dependence in the $\hat{x}$ direction, and hence, Fourier decomposition is allowable only for the $\hat{y}$ and $\hat{z}$ directions.

can be used to develop an approximate picture of the eigenmodes, if not an entirely accurate one. The singular nature of Eq. 3.15 can be observed more clearly in the following form

$$g\left(\xi_x - \frac{1}{k^2}\xi_x''\right) = \frac{g'}{k_y^2}\xi_x', \tag{3.16}$$

where $g = \rho(\omega^2 - \omega_A^2)$ and the prime notation signifies a derivative with respect to the spatial variable x. Notice that as the singularity is approached ($g \to 0$) g' in general remains finite. Except for the extraordinary case where $\xi_x' \to 0$ at the singular layer, it must be that the finiteness of the LHS of Eq. 3.16 is maintained by $\xi_x'' \to \infty$. In other words, the eigenfunction ξ_x becomes strongly peaked at the point where $\omega^2 = \omega_A^2$. Near the singular layer, the ξ_x term can be ignored and the remaining equation integrated once to yield $\xi_x' \approx A\,\omega^2/(\omega^2 - \omega_A^2)$ where A is an arbitrary scale factor, which again illustrates the peakedness of the displacement function near the singular points. The function ω_A^2 is the "Alfvén continuum" which should be interpreted as the frequency-space map of the resonance, or singular, points of the system. A similar function will appear in cylindrical and toroidal geometries. In the following sections, solutions to Eq. 3.15 are examined with three approaches: a variational analysis, direct numerical integration and transformation to a Schrödinger potential representation.

3.2.1 Variational Analysis

Equation 3.15 is amenable to a variational analysis whereby an estimate of the eigenvalue (ω^2) can be derived from an appropriate integral over a trial function in place of an actual eigenfunction. A nice discussion of variational theory and its derivation can be found in the text "Ideal Magnetohydrodynamics" by Freidberg [36]. Variational analysis of Eq. 3.15 shows that the integrating function is simply ξ_x^*, the complex conjugate of ξ_x, which gives for the estimate of the eigenvalue

$$\omega^2 = \frac{\int \omega_A^2 \left(|\xi_x|^2 + \frac{1}{k^2} |\xi_x'|^2 \right) \mathrm{d}x}{\int \left(|\xi_x|^2 + \frac{1}{k^2} |\xi_x'|^2 \right) \mathrm{d}x}, \tag{3.17}$$

where the limits of the integrals cover the entirety of the eigenfunction. The particular value of ω^2 derived by this method depends on the shape of the function ω_A^2. In the presence of a strong guide field defined by $B_z^2 \gg B_y^2$ the parallel wavenumber is $k_\parallel \approx (B_y/B_z)\, k_y + k_z$. For the purposes of illustration which will become more clear in the discussion of cylindrical geometry, k_y and k_z are chosen such that $k_\parallel^2$ has a strong local maximum (k_y is negative and k_z is positive in this example). Profiles of B_y and $\omega_A^2 = k_\parallel^2 v_A^2$ are illustrated in Fig. 3-2.

Using a test function localized about the maximum in the Alfvén continuum, the

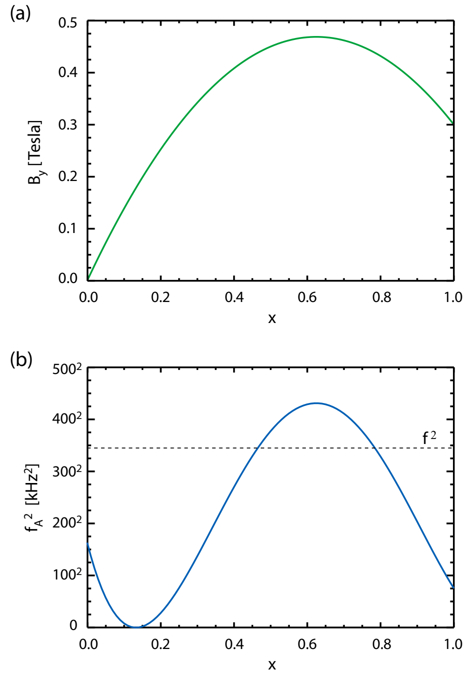

Figure 3-2: (a) The vertical ($\hat{y}$) magnetic field and (b) the associated Alfvén continuum ($f_A = \omega_A/2\pi$) using $B_z = 5$ Tesla, $k_y = -0.8\,\text{cm}^{-1}$ and $k_z = 0.03\,\text{cm}^{-1}$. The variational method shows that the eigenvalues f^2 (dashed line) are less than the value of the peak of the continuum.

variational analysis finds ω^2 to be some value less than the maximum of the Alfvén continuum. That this should be so can be seen in Eq. 3.17 where the eigenmode effectively averages the Alfvén continuum over its distribution, which necessarily results in an estimate less than the peak value. The variational analysis then tells us that any solution in this system must encounter the Alfvén continuum and hence should be peaked at the associated singular points.

3.2.2 Numerical Integration

Solutions of Eq. 3.15 may be found by direct numerical integration of the discretized system. In the case at hand, we take fixed boundary conditions such that $\xi_x(\bar{x} = 0) = \xi(\bar{x} = 1) = 0$ where $\bar{x} = x/a$ is a normalized coordinate for a slab which extends from $x = 0$ to $x = a$. Cast in discrete form, Eq. 3.15, being second order, can be solved for the i^{th} point as a function of the $(i-1)^{th}$ and $(i-2)^{th}$ points. The singularities must properly be dealt with by using a linear expansion and analytic solution near the singular layer and matching this to the numerical solution some distance away. Near the singular layer, ξ_x'' and ξ_x' dominate over ξ_x which remains finite. Expanding about the singular point, we let $\omega^2 - \omega_A^2 = \nu\left(\bar{x} - \bar{x}_s\right)$, where $\bar{x}_s$ is the position of the singular point and ν is some coefficient determined by continuity conditions. Ignoring the minor contributions from ξ_x near the singular point, an approximate solution in the singular layer (ξ_s) is

$$\xi_s = A + B\left(\bar{x} - \bar{x}_s\right)^{1-\nu}, \tag{3.18}$$

where A and B are unknown coefficients which must be found by matching ξ_x to ξ_s away from the singular layer. Combining the singular solutions with a standard recursion relation away from the singular layer, solutions can be constructed for different values of the eigenvalue. Defining $D = k_y^2 a^2$ and using $g = \rho(\omega^2 - \omega_A^2)$, Eq. 3.15 can be cast as a discretized recursion relation of the form,

$$\xi_i = (2 + D\,\mathrm{d}\bar{x}^2)\,\frac{4\,g_{i-1}}{g_i + 4\,g_{i-1} - g_{i-2}}\,\xi_{i-1} + \frac{g_i - 4\,g_{i-1} - g_{i-2}}{g_i + 4\,g_{i-1} - g_{i-2}}\,\xi_{i-2}. \tag{3.19}$$

One of the boundary conditions in the numerical solution of ξ can be trivially satisfied by starting the integration at a boundary. The results of the procedure presented here started the integration at $\bar{x} = 0$ with $\xi = 0$. Most likely, a guess ω^2 used in the integration scheme will result in a ξ which does not satisfy the $\bar{x} = 1$ boundary condition. However, eigenmodes may be found from test solutions which are not themselves eigenfunctions through an implementation of the so-called "shooting method" [58] involving a scan over test eigenvalues. In a system with multiple eigenvalues, proper implementation of this method requires having sufficiently fine resolution of the eigenvalues such that only a single solution is in the neighborhood of the test functions used in the shooting method. The problem of finding eigenmodes is in general nonlinear on account of the product of the eigenfunction and the eigenvalue appearing in the differential equation (Eq. 3.15).

Proper eigenfunctions of the system can be separated from the larger body of solutions by scanning the eigenvalue (ω^2) and observing the behavior of the solutions at the position $\bar{x} = 1$. One can generate a plot of $\xi_x(\bar{x} = 1)$ as a function of ω^2, call this $W(\omega^2)$. In a discretized scan of ω^2, one can identify eigenmodes of the system by finding the roots of $W(\omega^2)$. This technique is employed by advanced non-variational codes which will be used for analysis of modes in toroidal geometry and are discussed in more detail in section 3.5. To illustrate the technique, let us assume that we have scanned a number of eigenvalues and enter a region where $W(\omega^2)$ varies nearly linearly with ω^2. Taking two solutions in this approximately linear neighborhood,

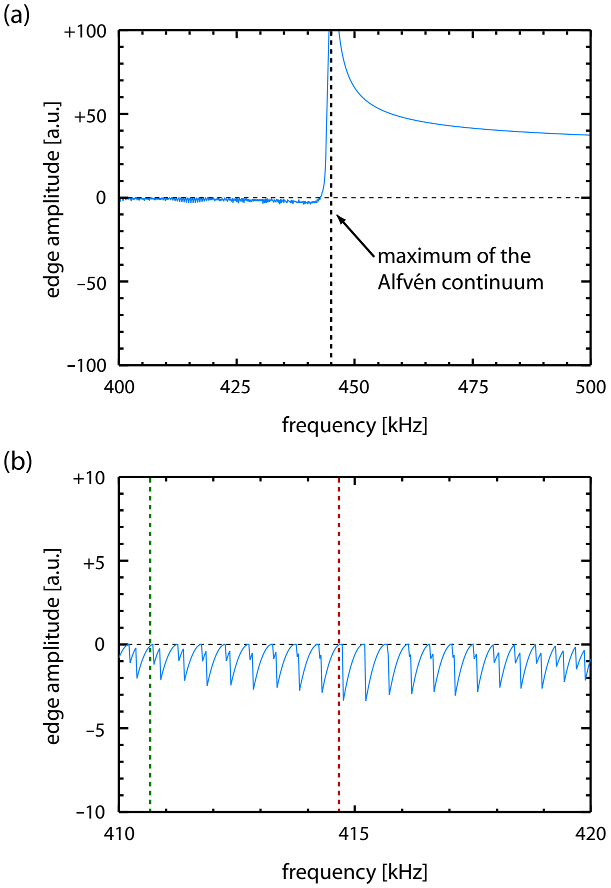

Figure 3-3: Plots of the edge amplitude of the function ξ_x as the eigenvalue (ω^2) is scanned. Eigenfunctions correspond to zero crossings of this curve. Plots (a) and (b) show the spectrum at two different resolutions. Note that the spectrum of solutions is very dense at values less than the maximum of the Alfvén continuum, with no solutions for $\omega^2 > \omega_A^2$. The vertical dashed lines in (b) identify the frequencies of solutions presented in Fig. 3-4.

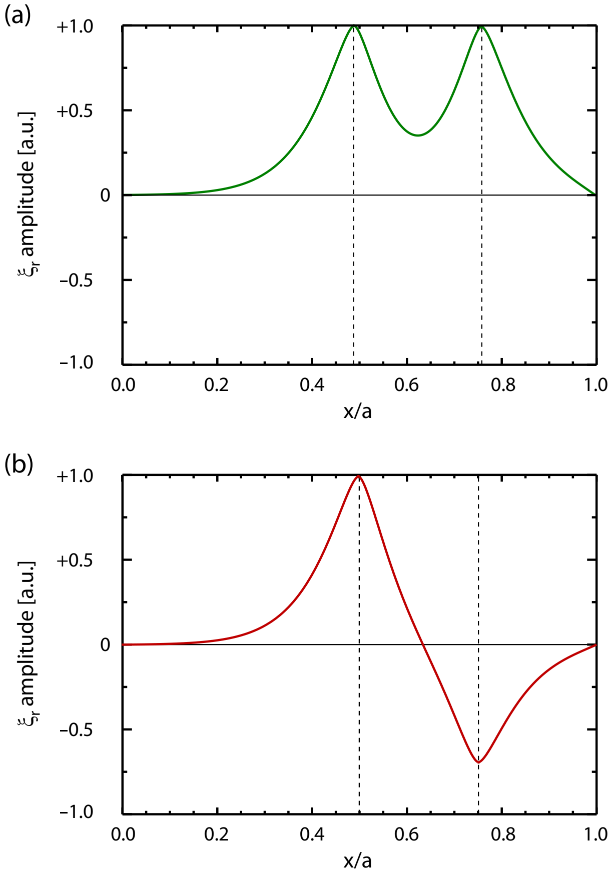

Figure 3-4: Representative "continuum" eigenmodes found through numerical analysis of Eq. 3.15. The solutions can be classified as (a) symmetric or (b) antisymmetric, general features that appear in solutions in toroidal geometry. The eigenmode in (a) corresponds to a frequency of 410.7 kHz and (b) to a frequency of 414.7 kHz in the roots of Fig. 3-3(b).

call them ξ_a and ξ_b with eigenvalues ω_a^2 and ω_b^2 respectively, we have

$$W(\omega^2) = W_a + \frac{W_b - W_a}{\omega_b^2 - \omega_a^2}\Delta\omega^2 + \mathcal{O}(\Delta\omega^2)^2, \tag{3.20}$$

where $\Delta\omega^2 = \omega^2 - \omega_a^2$. It is rather straight forward to determine from Eq. 3.20 the value of $\Delta\omega^2$ which satisfies $W = 0$, accurate to order $(\Delta\omega^2)^2$. From this form, a guess for the eigenvalue (ω_c^2) and eigenfunction (ξ_c) can be derived,

$$\omega_c^2 = \frac{W_b\omega_a^2 - W_a\omega_b^2}{W_b - W_a}, \tag{3.21}$$

$$\xi_c = \frac{W_b\xi_a - W_a\xi_b}{W_b - W_a}. \tag{3.22}$$

$$\tag{3.23}$$

The interpolated function ξ_c can now be compared to the exact solution derived from the differential equation using ω_c^2, and if the two solutions are deemed close enough by some measure, then we can stop, if not, this technique is iterated upon until convergence is reached. Certainly this technique could be combined with a predictor-corrector technique, or other advanced root solving algorithm, but the essence is the same. Plots of $W(\omega^2)$ resulting from a scan of ω^2 are shown in Fig. 3-3. Interestingly, there are no eigenfunctions above the maximum of the continuum as can be seen in Fig. 3-3, and all solutions have $\omega^2 < \omega_A^2$ in agreement with the variational analysis. It is apparent that the number of roots is very dense when $\omega^2 < \omega_A^2$. Representative eigenmodes corresponding to the frequencies at the dashed lines in Fig. 3-3(b) are presented in Fig. 3-4. These eigenmodes are strongly peaked at the points of continuum crossing, marked by the vertical dashed lines, which causes them to suffer large continuum damping and are not excited in experiment. This analysis shows that unstable Alfvén eigenmodes cannot be modeled in slab geometry, but illustrates some fundamental properties of the solution space. It is also important to note that the position of the maximum of the Alfvén continuum identifies a point of near symmetry in the solutions, and that this symmetry is reflected in the eigenmodes. We anticipate that eigenmodes in cylindrical and toroidal geometry will also exhibit this general feature.

3.2.3 Potential Formulation

An alternative representation of the problem may be derived through a change of variables which presents the question of eigenmode formation in the more familiar and intuitive representation of a quantum particle in a well. Using again a normalized spatial variable $\bar{x} \equiv x/a$, and $g = \rho(\omega^2 - \omega_A^2)$, and utilizing a change of variables through $\xi_x = g^{-1/2}\Psi$ gives

$$\Psi'' = V_{eff}\Psi \tag{3.24}$$

where

$$V_{eff} = D + \frac{1}{2}\frac{g''}{g} - \frac{1}{4}\left(\frac{g'}{g}\right)^2 \tag{3.25}$$

where $D = k_y^2 a^2$ and the primes denote derivation with respect to the normalized variable $\bar{x}$. Equation 3.24 can be interpreted as the Schrödinger equation for a steady-state wave function Ψ for an "Alfvén particle" with energy $E = 0$ in a potential well V_{eff} [8]. Whereas the classic quantum problem is formulated as one of finding the energy eigenvalues for a given potential, in the case of the Alfvén eigenmodes the problem is reversed in that the Alfvén particle has a fixed energy and the problem is instead one of finding the corresponding potential through variation of ω^2, which enters through the function $g = \omega^2 - \omega_A^2$ in Eq. 3.25. A similar procedure can be applied to the eigenvalue equations derived for cylindrical and toroidal geometries.

Three potential functions and the corresponding eigenfunctions are presented in Fig. 3-5. Panel (a) shows the potential function for an eigenmode which intersects the continuum at two points, similar to those presented in Fig. 3-4. This potential exhibits two deep wells, as expected based on the discussion of the singular behavior of the Alfvén continuum in Eq. 3.15. Panel (b) is the potential function for a case with $\omega^2 > \omega_A^2$ and admits no solutions. Panel (c) explores a hypothetical case under the assumption that we have neglected some essential physics in the derivation of Eq. 3.15 which modifies the coefficient of the LHS. Taking this modification to be the simplest imaginable form, that is, $g \rightarrow \rho(\omega^2 - \omega_A^2 - Q)$ where Q is some positive constant. The effect on the potential is the addition of the second term in the following expression,

$$V_{eff} = D - D\frac{Q}{g} + \frac{1}{2}\frac{g''}{g} - \frac{1}{4}\left(\frac{g'}{g}\right)^2. \tag{3.26}$$

The addition of this ad hoc term results in a negative potential when $Q > 0$ and has dramatic consequences for eigenmode formation. Indeed, without this term there can be only a potential hill for $\omega^2 > \max(\omega_A^2)$ and consequently no viable solutions. The addition of Q may generate an effective potential well in which an eigenmode may form. Notice that the structure of the eigenmode in Fig. 3-5c is gaussian-like, and does not exhibit the strong peaking as in case (a) with $\omega^2 < \max(\omega_A^2)$. There is of course, a critical value of Q below which proper eigenmodes do not form. It is a rather straightforward exercise to include Q in the variational theory, which indeed shows that ω^2 may rise above $\max(\omega_A^2)$ when Q is large enough.

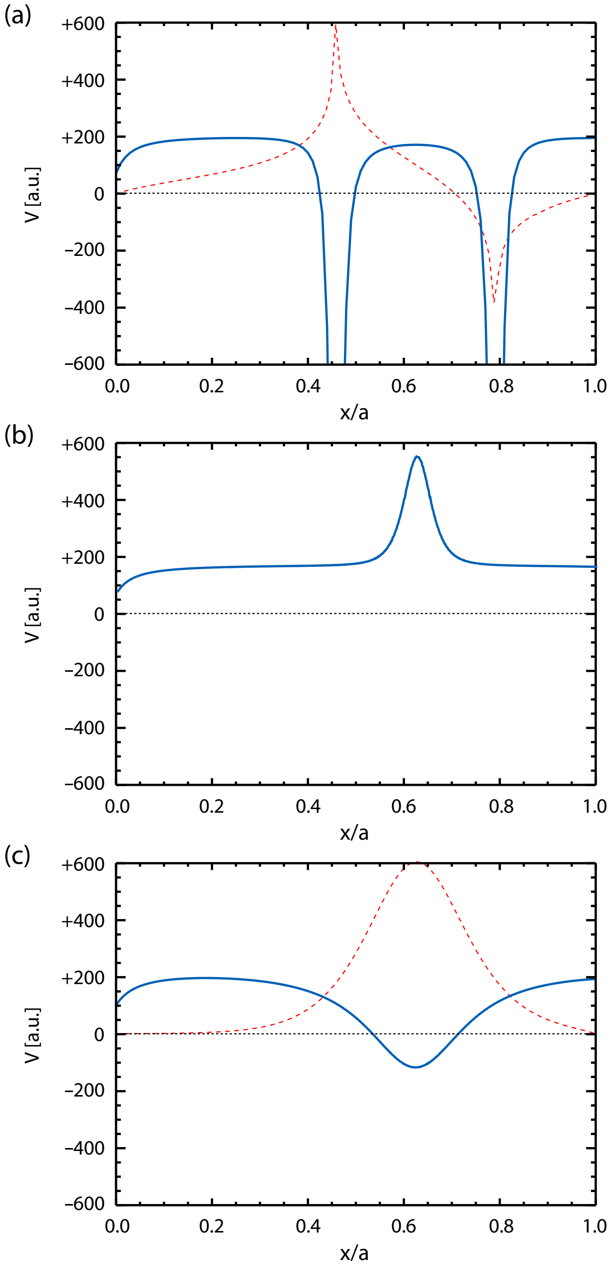

Figure 3-5: Potential functions (solid blue) and eigenfunction (dashed red) for three cases. Case (a) has $\omega^2 = \omega_A^2$ at two points which generates the deep potential wells, and case (b) has a $\omega^2 > \max(\omega_A^2)$ which creates a potential hill that does not admit eigenmodes. Case (c) uses the same value of frequency as case (b), but includes an ad hoc physics term which generates a potential well and allows an eigenmode to form.

3.3 Cylindrical Geometry

In moving to cylindrical geometry from slab geometry we let $\hat{x} \to \hat{r}$ and $\hat{y} \to \hat{\theta}$, which means that the differential operator changes as $\mathrm{d}/\mathrm{d}y \to (1/r)\mathrm{d}/\mathrm{d}\theta$. The so-called "screw pinch" is the most general representation of a cylindrically symmetric equilibrium [36]. In this system, the next order approximation of a tokamak plasma, the guide magnetic field is in the $\hat{z}$ direction and pressure balance is effected by currents in the $\hat{\theta}$ and $\hat{z}$ directions, generally with $|j_\theta| \ll |j_z|$. In such a configuration the guide magnetic field will be a weak function of radius due to the diamagnetic current, but within the accuracy of the ordering used here can be taken as constant, as can be seen in Fig. 3-6. Foreseeing the eventual step to the toroidal model, we take the screw pinch to be periodic in z with period $L = 2\pi R_0$ where R_0 will be interpreted as the major radius of the magnetic axis in toroidal geometry. In the periodic screw-pinch there is a well-defined parameter describing the winding ratio of the equilibrium guide field to the poloidal field, a function of the radial coordinate only. This parameter we define as $q = q(r)$, where

$$q(r) = \frac{r\,B_z}{R_0\,B_\theta}. \tag{3.27}$$

Note that q is finite at $r = 0$ because the poloidal field is proportional to r near the magnetic axis. A Taylor expansion of the current density near the axis, $j_z(r) \approx j_{z,0} + j'_{z,0}\,r$, shows that the poloidal field is approximated by $B_\theta \approx \frac{1}{2}\mu_0 r(j_{z,0} + \frac{2}{3}j'_{z,0}r)$. Taking the limit $r \to 0$, q at the magnetic axis (q_0) becomes,

$$q_0 = \frac{2\,B_z}{\mu_0 R_0 j_0}. \tag{3.28}$$

These definitions will carry over to the toroidal case, except that q will be properly defined as a flux surface averaged quantity, and $B_z \rightarrow B_\phi$, where ϕ is the toroidal angular coordinate. When q is large, the winding of the guide field is large relative to the winding of the poloidal field, meaning that the field lines may wrap many times in the $\hat{z}$ (toroidal) direction before closing once in the poloidal direction. The parameter qR_0 approximates, to within a few percent, the length required to circulate the torus once along a magnetic field line to return to the initial poloidal position. From the definition $k_\parallel = (\mathbf{k} \cdot \mathbf{B})/B$ we have

$$k_\parallel = \frac{1}{R_0}\left(n - \frac{m}{q}\right), \tag{3.29}$$

where, importantly, we see that $k_\parallel$ is inversely dependent on q. As noted in the prior section, eigenmodes may form near regions of local maxima in the Alfvén continuum. In cylindrical geometry, a maximum in $k_\parallel$ may form for certain values of m and n and for particular q profiles. Recalling $\omega_A^2 = k_\parallel^2 v_A^2$, we observe that a minimum in q (q_{min}) can create a local maximum in ω_A^2 for an appropriate choice of m and n, and thus expect that there may exist modes near q_{min}. This observation provides the basis for anticipation of the reversed shear Alfvén eigenmode (RSAE) which comprises the focus of this thesis.

Periodicity of the θ and z coordinates requires that eigenmodes of the system also exhibit a periodic structure and hence, the Fourier representation takes the form,

$$\tilde{A}(r,\theta,z,t) = \sum_{m,n} A(r) e^{-im\theta + i\frac{2\pi n}{L}z - i\omega t}, \tag{3.30}$$

where $\tilde{A}$ is a generalized perturbed quantity, $A(r)$ is the radial function, m is the poloidal mode number and n is the azimuthal (toroidal) mode number. The negative sign in front of m is a matter of convention, the reason being that a choice of positive

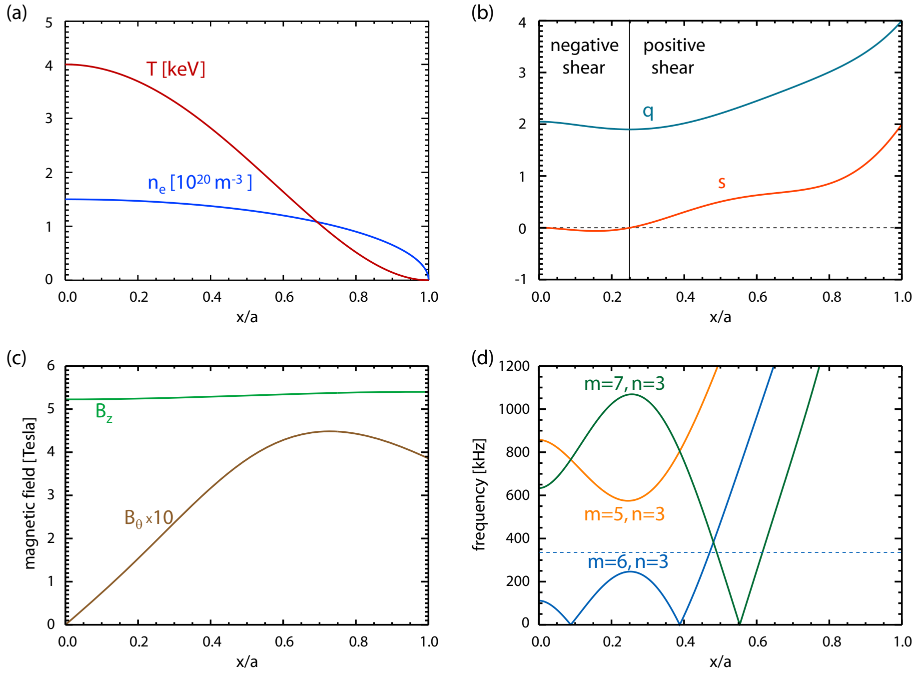

Figure 3-6: Representative profiles for a cylindrical screw pinch equilibrium showing (a) temperature and density, (b) q and magnetic shear, (c) B_z and B_θ, and (d) the absolute value of the Alfvén continua for three mode number combinations. The $m = 6$, $n = 3$ continuum exhibits a strong local peak in the Alfvén continuum at the radial location of q_{min}. The dashed line in (d) marks the frequency eigenvalue of the eigenmode in Fig. 3-7(a).

m and n corresponds to wave propagation in the ion diamagnetic drift direction. The ion diamagnetic velocity is $\mathbf{v}_D = \mathbf{B} \times \nabla p_i / n_i Z_i e B^2$, where p_i is the ion pressure, n_i is the ion density, and $Z_i e$ is the ion charge [35]. Taking B_z and I_p (the plasma current) to be in the positive $\hat{z}$ direction, and assuming a monotonic decreasing pressure profile, gives $v_{D,\theta}$ in the $-\hat{\theta}$ direction and $v_{D,z}$ in the $+\hat{z}$ direction.

The poloidal and guide magnetic fields of a screw pinch are easily reconstructed when the pressure and q profiles are specified. Using the prior definition of q which allows us to express B_θ in terms of B_z, and using the pressure balance equation for equilibrium $\nabla p = \mathbf{j} \times \mathbf{B}$ with Ampere's Law, and defining a new variable $Y = B_z^2$ we have

$$(1 + h) Y' + \left(h' + 2\frac{h}{r} \right) Y + k = 0, \tag{3.31}$$

where $h = 4\pi^2 r^2 / L^2 q^2$ and $k = 2p'/\mu_0$ and primes denote derivatives with respect to the coordinate r. Given a boundary condition, Eq. 3.31 can be integrated to solve for $B_z(r)$, from which we may determine $B_\theta(r)$ through the known form of q. In this way, specific screw pinch equilibria may be constructed from experimental data or theoretical models, as is illustrated in Fig. 3-6. Looking toward the analysis of eigenmodes in toroidal geometry, we map the Alfvén continua in cylindrical geometry for a single n and a range of m, as is done in Fig. 3-6(d). There are two main features of importance in Fig. 3-6(d). The first is that the $m = 6$, $n = 3$ continuum exhibits a local maximum at the radial position of q_{min}, from which we can expect that this may allow an $m = 6$, $n = 3$ eigenmode to form. Secondly, there are points where the continua are degenerate, which is important for toroidal geometry where strong coupling between poloidal harmonics arises at points of degeneracy.

The following set of equations comprise the basis for the development of the eigenvalue equation. When we employ the same approximations used in the former analysis of the slab configuration, namely $\nabla\cdot\boldsymbol{\xi} = 0$ and $\xi_z = 0$, and using $B_\theta/r - (\partial/\partial r)B_\theta = sB_\theta/r$ where $s = \mathrm{d}\ln q/\mathrm{d}\ln r$ is the magnetic shear, the eigenvalue equation for ξ_r is very similar to that derived for slab geometry. To the order of approximation used here, $k_\perp = -m/r - nB_\theta/R_0B_0 \approx -m/r$, allowing ξ_θ to be used in place of $\xi_\perp$. Furthermore,

$$\begin{aligned}
-\mu_0\rho\omega^2\xi_r &= iBk_\parallel B_{1,r} - 2\frac{B_\theta}{r}B_{1,\theta} - \frac{\partial}{\partial r}h, &(3.32)\\
-\mu_0\rho\omega^2\xi_\theta &= iBk_\parallel B_{1,\theta} + 2\frac{B_\theta}{r}B_{1,r} + i\frac{m}{r}h, &(3.33)\\
B_{1,r} &= iBk_\parallel\xi_r, &(3.34)\\
B_{1,\theta} &= iBk_\parallel\xi_\theta, &(3.35)\\
\nabla\cdot\xi &= \frac{1}{r}\frac{\partial}{\partial r}(r\xi_r) - i\frac{m}{r}\xi_\theta = 0. &(3.36)
\end{aligned}$$

The quantity $h = \mathbf{B}_0\cdot\mathbf{B}_1 + \mu_0 p_1$ need not be solved for directly, but can be eliminated by inverting Eq. 3.33 to solve for $h = h(\boldsymbol{\xi})$. Defining new variables $\bar{r} = r/a$ and $\chi = \bar{r}\xi_r$, the system of equations 3.32 - 3.36 can be reduced to an eigenvalue equation of the form

$$G\chi = \frac{\partial}{\partial\bar{r}}\left[F\frac{\partial}{\partial\bar{r}}\chi\right], \tag{3.37}$$

where,

$$F = \rho \bar{r} \left(\omega^2 - \omega_A^2 \right), \tag{3.38}$$

$$G = m^2 \left[\frac{F}{\bar{r}^2} - \frac{2B^2}{\mu_0 R_0^2} \frac{s}{\bar{r} q^2} \right]. \tag{3.39}$$

We see now the development of a term on the LHS of Eq. 3.37 which we may identify as similar to the Q from the discussion of the potential formulation in section 3.2.3. Also, recall that the leading term in the potential scales as G/F, using the terms defined here, so that it has a dominant r^{-2} form near the axis, similar to the effective potential arising from conservation of angular momentum in classical mechanics, reinforcing the image of the Alfvén particle in a central force potential. Interestingly, there is a direct correspondence between the mode number m and the angular momentum quanta of quantum systems. The presence of the m^2 component (angular momentum) of the effective potential has important consequences for eigenmode formation. In effect, the m^2 term prevents eigenmodes from forming very close to the axis, so that translation of conditions which generate a solution at a mid-range value of $\bar{r}$ to a lesser value of $\bar{r}$ may result in no solution. This point may have particular importance to the study of RSAEs which are sometime seen to develop between sawteeth and is discussed in more detail in chapter 5. To further explore Eq. 3.37 we define, as before, an effective potential function V_{eff}.

$$\begin{aligned} V_{eff} &= \frac{G}{F} + \frac{1}{2}\frac{F''}{F} - \frac{1}{4}\left(\frac{F'}{F}\right)^2 \qquad (3.40) \\ &= \frac{m^2}{\bar{r}^2} - \frac{2\,m^2\,V_A^2}{R_0^2(\omega^2 - \omega_A^2)}\,\frac{s}{\bar{r}^2 q^2} + \frac{1}{2}\frac{F''}{F} - \frac{1}{4}\left(\frac{F'}{F}\right)^2 \end{aligned}$$

The potentials corresponding to the three continua from Fig. 3-6 are presented in Fig. 3-7 using a value of ω^2 which corresponds to the eigenfunction shown. The width of the potential well is due solely to the second term in Eq. 3.41. The presence of the deep trench in the well, arising due to a singularity where $\omega^2 - \omega_A^2 = 0$, causes the eigenmode to form a secondary peak. Such solutions have significant continuum damping, and furthermore, the double-peaked structures typically have very small growth rates and are unlikely to be excited in experiment (discussed in greater detail in section 3.5.3).

The dispersion relation for the cylindrical RSAE mode can be derived from a variational analysis of Eq. 3.37. As before, we use ξ^* for an integrating function, with the result,

$$\omega^2 \approx \omega_A^2 \left[1 + \frac{\Delta q}{mq(m-nq)^2} \left(\frac{r_0^3}{2m} - \frac{1}{3}(m-nq) \right) \right] \tag{3.41}$$

where the terms $\bar{r}_0 = \bar{r}$ and $\Delta q = (\mathrm{d}^2/\mathrm{d}\bar{r}^2) q\, \bar{r}_0^2$ are evaluated at q_{min}. We see that a critical value of shear exists, which enters through the relation that $r_0^3 > \frac{2m}{3}(m-nq)$, which requires very small values of $k_\parallel$ to be effective, and does not represent a viable solution for experimental conditions. Nonetheless, Eq. 3.41 illustrates how an undamped eigenmode may in principle be generated. If such modes were excited, the leading dependence on ω_A^2 includes a strong dependence on q_{min}, such that the frequency of the mode will increase rapidly as q_{min} decreases. Recall that $\omega_A^2 = k_\parallel^2 v_A^2$ and $k_\parallel \sim m/q{-}n$, a feature which suggests a method for inferring $q_{min}(t)$ by measuring the frequency as a function of time.

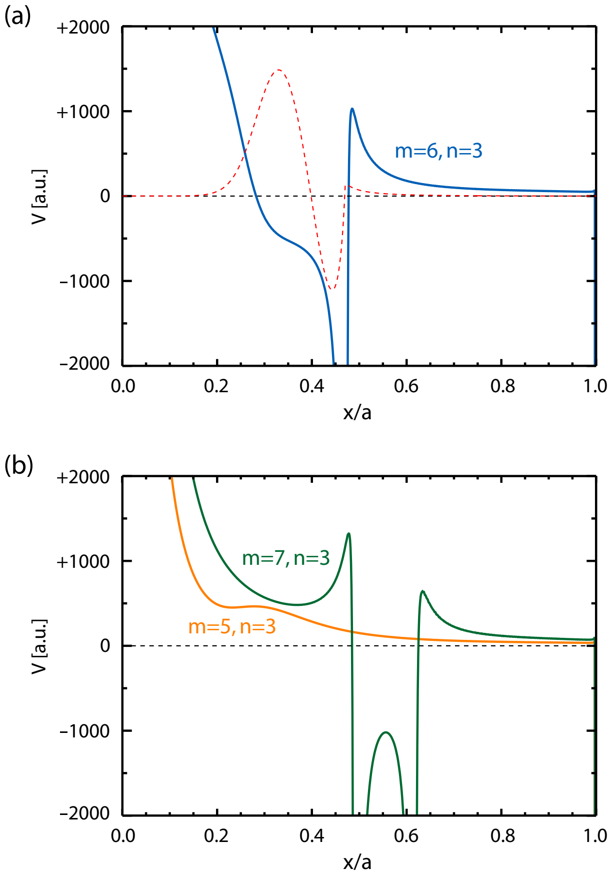

Figure 3-7: Potentials for the cases (a) $m = 6$, $n = 3$ mode and (b) the $m = 5$, $n = 3$ and the $m = 7$, $n = 3$ modes. The dashed curve in panel (a) is the eigenmode found by numerical integration.

3.4 Toroidal Geometry

The goal of this section is to outline the steps by which one can construct an eigenmode expression similar to 3.37 which is applicable for toroidal geometry. In moving from cylindrical geometry to toroidal geometry, the z coordinate becomes the ϕ coordinate. The $\hat{r}$ and $\hat{\theta}$ basis also become ϕ dependent, though the variation enters as functions of θ. The details of the eigenmode analysis are considerably more involved in toroidal geometry on account the coupling of many poloidal harmonics (m) due to the presence of equilibrium and first order quantities which depend on θ. It should be noted that toroidal symmetry leaves the system of equations invariant under translations in ϕ, and hence we can look for eigenmodes which are solutions of a single n, though now containing perhaps many m. The general analytic strategy is to find an appropriate expansion parameter to simplify the system to a small number of coupled equations.

The small parameter $\epsilon = r/R_0$ naturally arises in the equations and can be used to distinguish orders of coupling between poloidal harmonics. The result of such an analysis is that, within some parameter space limits imposed by approximations, an expression for the RSAE eigenmode is described through a second order differential equation, similar to that derived in cylindrical geometry. The largest effect as we move from cylindrical to toroidal geometry is that the guide magnetic field develops an approximate $1/R$ dependence. The coupling of poloidal harmonics can be observed in the first order terms like $B_\phi \boldsymbol{\xi}$ (see Eqs. 3.7 and 3.8). Approximating the toroidal field as $B_\phi \sim B_0(R_0/R) \sim B_0(1-\epsilon\cos\theta)$, and taking as our basis a set of functions of the form $\boldsymbol{\xi}_{m,n}(r,\theta,\phi,t) = \boldsymbol{\xi}(r)\exp(-im\theta + in\phi - i\omega t)$, coupling between m and $m \pm 1$ takes the form,

$$\begin{aligned}
B_\phi \, \boldsymbol{\xi}_{m,n} &= B_0 \left(1 - \epsilon \cos\theta\right) \; \boldsymbol{\xi}(r) \, e^{-im\theta + in\phi - i\omega t} \\
&= B_0 \left(1 - \frac{1}{2}\epsilon \left(e^{i\theta} + e^{-i\theta}\right)\right) \boldsymbol{\xi}(r) \, e^{-im\theta + in\phi - i\omega t} \\
&= B_0 \, \boldsymbol{\xi}_{m,n} - \frac{1}{2} \, \epsilon B_0 \left(\boldsymbol{\xi}_{m-1,n} + \boldsymbol{\xi}_{m+1,n}\right). \qquad (3.42)
\end{aligned}$$

Coupling between m and $m \pm 1$ is of order ϵ and hence we anticipate that modifications to the differential equation will enter as corrections of order ϵ^2. Rigorous derivations of the RSAE dispersion relation can be found in Refs. [8, 59]. Extensions to the theory accounting for energetic ions [59, 60] and finite pressure effects [6, 61] have also significantly added to the understanding of RSAEs across a range of conditions. The following discussion of Alfvén eigenmodes in toroidal geometry merely outlines some of the essential physics regarding these modes, adapted from reference [60].

We note that in addition to the toroidal field's $1/R$ dependence, the poloidal field also develops high-field-side (HFS) to low-field-side (LFS) asymmetry. The poloidal magnetic flux develops an approximate $1/R$ dependence from the hoop force, as well as an outward shift due to finite pressure effects, known as the Shafranov shift [62, 36]. These effects result in a scaling of the poloidal magnetic field by a factor of $[1 + \epsilon \cos\theta - \Delta' \cos\theta]^{-1}$, where Δ' is the derivative of the Shafranov shift, and can be approximated as $\Delta' \approx (\frac{1}{4} + \beta_\theta)\epsilon$, where $\beta_\theta = 2\mu_0 p_0 / B_\theta^2$ is the poloidal beta [62]. We consider here the special case where the Shafranov shift and hoop force cancel in B_θ, leaving only a $1/R$ dependence in B_ϕ.

Inspection of Eqs. 3.7 through 3.10 in toroidal geometry shows the primary effect then enters through the calculation of $k_\parallel$ in the terms $\mathbf{B}_0 \cdot \nabla$ and $\mathbf{B}_0 \cdot \mathbf{B}_1 + \mu_0 p_1$. Using the aforementioned approximate form for B_ϕ, we find the parallel wavenumber for the m^{th} poloidal harmonic to be

$$\begin{aligned} k_\parallel &= \frac{\mathbf{k}\cdot\mathbf{B}_0}{B_0} \\ &= \frac{1}{B_0}\left(-\frac{m}{r}B_\theta + \frac{n}{R_0}B_\phi\right), \end{aligned}$$

where B_0 is the modulus of the magnetic field. Using the definition of q (Eq. 3.27), and taking $B_0 \approx B_\phi$ and $B_\phi \approx B_0(1-\epsilon\cos(\theta))$ we have

$$\begin{aligned} k_\parallel &\approx \frac{1}{R_0}\left(-\frac{m}{q}+n\right) - \frac{m\,\epsilon}{qR_0}\cos\theta \qquad (3.43) \\ &\equiv k_{\parallel,m} - \frac{m\,\epsilon}{2qR_0}\left(e^{i\theta}+e^{-i\theta}\right). \qquad (3.44) \end{aligned}$$

In a rather straightforward fashion, Eq. 3.44 may replace the former definitions of $k_\parallel$ entering in ω_A^2. Had we stopped the analysis at Eq. 3.43 instead of 3.44, we might be led to believe that the value of $k_\parallel$ has a strong θ dependence, which can be of such a magnitude to cause $k_{\parallel,m}$ to change sign unless $q < m/n(1+\epsilon)$ everywhere. Clearly this condition on $q(r)$ cannot be satisfied for all radii. The solution to this problem is provided by way of Eq. 3.44, which shows that instead of a variation of $k_\parallel$, the θ dependence should be interpreted as a coupling of poloidal harmonics as per Eq. 3.42. The presence of the θ dependent terms in Eq. 3.44 then specifies a constraint on the amplitudes of the $m \pm 1$ terms. Requiring that $k_\parallel$ have the same sign everywhere implies that $\xi_{m\pm1}/\xi_m \sim 2(m-nq)/nq \sim \epsilon$. Considering that $\epsilon \sim 10^{-1}$ for typical experimental values, the coupling between ξ_m and $\xi_{m\pm1}$ can be considered weak. Extending this argument to the next order shows that the coupling between m and $m \pm 2$ will be of order ϵ^2, allowing a reasonable truncation of the coupling to

m and $m \pm 1$, at least for regions where $q(r)$ does not vary rapidly, which is the case for the RSAEs localized near the minimum in q.

With the introduction of coupling between m and $m \pm 1$, imposing the condition that $m \gg 1$ and truncating at order ϵ^1 we develop a system of three coupled equations in place of the former differential equation Eq. 3.37. Using the notation $\xi_r(m,n) \to \xi_m$ and $\xi_r(m \pm 1, n) \to \xi_{m\pm1}$ for the radial displacements the system of equations is,

$$\begin{pmatrix} \hat{G}_{m-1,m-1} & \hat{G}_{m-1,m} & 0 \\ \hat{G}_{m,m-1} & \hat{G}_{m,m} & \hat{G}_{m,m+1} \\ 0 & \hat{G}_{m+1,m} & \hat{G}_{m+1,m+1} \end{pmatrix} \begin{pmatrix} \xi_{m-1} \\ \xi_m \\ \xi_{m+1} \end{pmatrix} = 0 \tag{3.45}$$

where the $\hat{G}$ operators are differential operators. The diagonal terms have coefficients of $\mathrm{d}^2/\mathrm{d}r^2$ proportional to $\omega^2 - \omega_{A,m}^2$ which can be small for only one of the terms, at least when we are looking for RSAE solutions of this system. Without loss of generality, we take this term to be smallest for the $\hat{G}_{m,m}$ term.

An analytic solution of this system of equations requires that the operators $\hat{G}_{m,m+1}$ and $\hat{G}_{m,m+1}$ be inverted, which in general results in an integro-differential equation for ξ_m. Breizman *et al.* (Ref. [60]) note however, that for the given regime, the integral operators resulting from the inverse transformations cancel exactly with the differential operators. A full analysis of this system of equations will not be presented here. The interested reader can find detailed analysis in Refs. [6, 8, 60, 61]. The result of such analysis, using $\bar{r} = r/a$ as in the cylindrical analysis, is summarized here:

$$G\chi = \frac{\partial}{\partial \bar{r}}\left[F \frac{\partial}{\partial \bar{r}}\chi\right], \tag{3.46}$$

where,

$$F = \rho \bar{r} \left(\omega^2 - \omega_A^2 \right), \tag{3.47}$$

$$G = \frac{m^2}{\bar{r}^2} \left[F - 6\rho\, \bar{r} \omega^2 \frac{\epsilon^2}{1 - 4 \left(m - nq \right)^2} \right]. \tag{3.48}$$

And as before we construct an effective potential, defining $\epsilon_a = a/R_0$,

$$V_{eff} = \frac{m^2}{\bar{r}^2} - \frac{6\, m^2\, \epsilon_a^2\, \omega^2}{\left(\omega^2 - \omega_A^2 \right) \left(1 - 4 \left(m - nq \right)^2 \right)} + \frac{1}{2} \frac{F''}{F} - \frac{1}{4} \left(\frac{F'}{F} \right)^2 . \tag{3.49}$$

As is often done in theoretical works, Eqs. 3.46 or 3.49 can be expanded in the parameter $\Delta \bar{r} = \bar{r} - \bar{r}_0$ where $\bar{r}_0$ is the radial position of q_{min}[60]. The Alfvén continuum may be locally approximated by a parabola, and in this way the problematic intersections with the continuum are avoided. The result is that smooth solutions are found, free of any compressional effects arising from continuum interaction, though this may not fully represent the experimental reality.

An approximate dispersion relation can be derived from Eq. 3.46, based on a variational analysis [60]. As mentioned at the beginning of this chapter, consideration of finite pressure effects has been considered in the RSAE theory. Finite pressure has significant effects in the limit $k_\parallel \to 0$, where the dispersion relation becomes coupled to the geodesic acoustic modes [59, 63], but has only a very minor role in the Alfvénic dominated regime. The effect of finite pressure is the addition of a minimum frequency offset to the dispersion relation, which is expressed as

$$\omega_{RSAE}^2 \approx \omega_0^2 + \omega_A^2 + (\Delta\omega)^2, \tag{3.50}$$

where ω_0^2 is a function of the temperature, $\omega_A^2 = v_A^2\,(m/q_{min} - n)^2/R_0^2$ and $(\Delta\omega)^2$ is a function of finite pressure gradients and energetic ion effects. For q_{min} close to m/n, the dispersion relation may be expanded as

$$\omega_{RSAE}^2 \approx \omega_0^2 + \omega_A^2 n^2(\delta q)^2 + (\Delta\omega)^2, \tag{3.51}$$

where $\delta q = m/n - q_{min}$. Comparisons of experimental data to approximate dispersion relationships including finite pressure effects are explored in chapter 4.

As a last note, the issue of spectral "gaps" is discussed. The analysis of the RSAE-like modes considered the case of weak coupling between m and $m \pm 1$. However, the strength of the coupling increases as the spectral "distance" between the Alfvén continua decreases, much like line splitting in atomic systems. The coupling reaches a maximum at the point where $\omega_{A,m}^2 = \omega_{A,m+1}^2$, a condition satisfied at $q_{TAE} \equiv (m + \frac{1}{2})/n$. This coupling process results in a gap structure, of width approximately $\Delta\omega \approx 2\epsilon_a \bar{r}^2 |k_{\parallel,m}| v_A$ [20]. The gap generated by toroidal effects is known as the toroidicity-induced Alfvén eigenmode (TAE) gap and is responsible for the development of undamped eigenmodes characterized by large radial extent and strong coupling of m and $m \pm 1$ poloidal harmonics. The second order effects (ϵ^2) in this analysis also allow coupling between the m and $m \pm 2$ modes, though as noted earlier, this coupling is very weak. However, higher order geometric effects induce coupling between a broader range of harmonics. For example, elongation couples m and $m \pm 2$ at order ϵ and produces the ellipticity-induced Alfvén eigenmode (EAE) gap. In theory, an infinite number of gaps exist, however, in practice the magnetic geometry is dominated by toroidicity and elongation, and therefore it is usually only the TAE and EAE gaps which allow unstable modes. Additionally, eigenmodes forming in gaps of higher order require higher energy for instability, reducing the likelihood of their excitation.

3.5 NOVA

NOVA is a set of programs which solves for eigenmodes and eigenvalues (ω^2) in the shear Alfvén regime for full toroidal geometry. Additionally, it calculates the associated perturbations of density, temperature and magnetic field [64]. NOVA employs a non-variational algorithm for identifying eigenmodes, similar to that illustrated in section 3.2.2. Restriction to the frequencies well below the ion cyclotron frequency allows finite Larmor radius (FLR) corrections to be ignored, a requirement for the single fluid MHD model. The RSAEs and TAEs which are the focus of this thesis are characterized by one or two dominant poloidal harmonics and are localized to the plasma core.

The first part of this section describes the input parameters for NOVA calculations and the experimental sources for this data. The second part presents an overview of typical NOVA calculations with representative solutions, followed by a discussion of the sensitivity studies. The primary focus of the sensitivity studies will be on the influence of various parameters on the eigenfrequencies, an important aspect for utilizing NOVA calculations as a means of inferring the evolution of q_{min}. The sensitivity of the spatial structure will be examined in greater detail in section 3.6 regarding the synthetic PCI analysis.

3.5.1 NOVA Input Parameters

NOVA is composed of essentially three separate programs. The first generates the MHD equilibrium and magnetic topology. The second calculates the Alfvén continuum for a given toroidal mode number and range of poloidal mode numbers. The third solves the first-order linear perturbation equations for the eigenmodes in the calculated equilibrium. A kinetic extension of NOVA for the calculation of growth rates is discussed in section 3.5.3. The equilibrium (in the absence of flows) is determined by solution of the equation $\vec{\nabla} p = \mathbf{j} \times \mathbf{B}$. The pressure profile can be specified either as an experimentally determined profile or through a composition of the electron density profile, electron temperature profile and ion temperature profile. In the analysis used in this thesis the separate density and temperature profiles are specified, which are taken from the Thomson scattering, electron cyclotron emission (ECE) and neutron flux diagnostics, respectively. Similar to the procedure outlined in section 3.3 the separate components of $\mathbf{B}$ may be found once the pressure profile and q profile are specified with additional boundary shape constraints. The plasma shape is specified through four geometric parameters: the tokamak major radius (R_0), the minor radius (a), the edge elongation (κ) and the edge triangularity (δ). The experimental triangularity is often specified as distinct upper and lower values, usually with $\delta_l \approx 0.5$ and $\delta_u \approx 0.3$ for lower-single-null configurations. The calculations in this thesis use an average value of the triangularity, though the sensitivity to this parameter is discussed here. The presence of the external control coils, operated in the "push" configuration (current directed opposite to the plasma current), are responsible for the plasma shaping and also for the enhancement in the magnitude of q toward the plasma edge, beyond that of the MHD value (Eq. 3.27). At large enough values of shaping coil current, a magnetic "X-point" can be created at the plasma edge where the poloidal field vanishes, causing q (formally defined as a flux surface averaged quantity) to go to ∞. The modeling of the edge plasma is somewhat problematic in NOVA for this reason. The analysis presented in this thesis employs the fixed-boundary solutions, that is, the eigenmodes are forced to vanish at the plasma edge so that no magnetic perturbation exist in the vacuum region. This is, of course, known to be incorrect because of the very existence of signals on the Mirnov coils which register the presence of magnetic perturbations arising from core-localized eigenmodes. This interesting aspect is discussed in section 4.4.

While NOVA's equilibrium solver requires only a pressure profile, the solution of the Alfvén continuum and eigenmodes requires separate knowledge of the density and temperature. This arises because the Alfvénic and acoustic wave branches are determined by the density and temperature separately. With the assumption of charge neutrality and specification of the plasma composition the mass density is well defined. The NOVA plasma is specified by three ion species: a majority species, a minority species, and an impurity species. The number density of each ion species is taken to be proportional to the electrons, with the mass density thereby determined through specification of the plasma Z_{eff} and minority fraction. For the cases of interest, those pertaining to the Alcator C-Mod experiments in $D(H)$ plasmas, the hydrogen minority fraction can be lumped together with the deuterium for the accounting of the number densities. Defining the quantities $\alpha_i = n_i/n_e$ and $\alpha_I = n_I/n_e$ for the majority species (m_i, Z_i) and the impurity species (m_I, Z_I), respectively, results in the following expressions for the mass density (ρ_m) and plasma pressure (p_{tot}).

$$\rho_m = n_e \left(\alpha_i m_i + \alpha_I m_I \right), \tag{3.52}$$

$$p_{tot} = n_e T_e \left(1 + \tau \left(\alpha_i + \alpha_I \right) \right), \tag{3.53}$$

where in the pressure expression we have introduced the variable $\tau = T_i/T_e$, in which the majority and impurity species are assumed to be at the same temperature. For the case of deuterium plasma with carbon impurity, the mass density is independent of Z_{eff}. This effect arises because the ratio m/Z is the same for deuterium and carbon, equal to 2. The presence of Mo^{+32} which may heavily influence Z_{eff} in the core of Alcator C-Mod plasmas, in contrast, has $m/Z = 3$ and will therefore cause an increase in the mass density at constant electron density. This effect may be rather small however, for even with a large value of $Z_{eff} = 5$, the mass density increases by only 6%, which translates to an approximate 3% change in the Alfvén frequencies, or a value in the range of 5 – 10 kHz. Plasma composition in Alcator C-Mod may be determined by multiple methods. Assuming that everywhere the impurity species' densities are proportional to the electron density, we may estimate Z_{eff} from calculation of the plasma resistivity. This method of course ignores the differences in ionization and source rates which will affect the higher Z impurities (like Mo^{+32}) and makes many assumptions about the resistivity profile. In fact, it is likely that the impurity density profiles deviate strongly from the electron density, and may significantly influence the diffusion of the toroidal electric field and the Ohmic current [18, 65].

It should be noted that while the input profiles for NOVA are reported as a function of the normalized toroidal flux coordinate ($\sqrt{\Psi_{tor}}$), the output profiles are reported as a function of the normalized poloidal flux coordinate ($\sqrt{\Psi_{pol}}$), both of which are approximately linear in the physical minor radial coordinate. In the following presentations of NOVA calculations, the data will be presented in the $\sqrt{\Psi_{pol}}$ coordinates. Near the magnetic axis, the differences in these coordinate systems may be on the order of 20%, which is significant when comparing the synthetic diagnostic signal to the experimental data. Given below are approximate forms of the toroidal and poloidal flux functions, to illustrate the differences between the radial coordinate:

$$\Psi_{pol}(r) = \int_0^r \mathbf{B}_{pol} \cdot d\mathbf{A}_{pol}, \tag{3.54}$$

$$\Psi_{tor}(r) = \int_0^r \mathbf{B}_\phi \cdot d\mathbf{A}_{tor}, \tag{3.55}$$

where in both cases the area element is understood to be the area of the bounding flux surface. For the sake of clarity, a flux surface boundary is defined to be the projection onto the poloidal plane of an equilibrium magnetic field line originating at a midplane radius of r. The gross features of these relations can be extracted with a few simplifying assumptions. Regarding the poloidal flux, the magnitude of $\mathbf{B}_{pol}$ is equal to rB_0/R_0q when q is known. As q is formally calculated as a flux surface average of the quantity $d\phi/d\theta$ of the magnetic field lines, resulting in a replacement of the spatial quantity B_ϕ by the constant B_0, the differential area should reflect this averaging and use the cross section passing vertically through the magnetic axis. Specifically, we take $\mathrm{d}\mathbf{A}_{pol} = 2\pi R_0(\kappa + r\kappa')\,\mathrm{d}r$, where κ' denotes the derivative of κ, the vertical elongation, with respect to r and captures the expansion of the flux surfaces due to the elongation. Thus, we have

$$\Psi_{pol}(r) \approx B_0 \int_0^r \frac{2\pi r}{q}\ (\kappa + r\kappa')\ \mathrm{d}r, \tag{3.56}$$

from which the relation $\sqrt{\Psi_{pol}} \propto r$ is seen to be true near the plasma core where q and κ are relatively flat. In NOVA, the poloidal flux is normalized such that it is equal to 0 at the magnetic axis and equal to 1 at the plasma edge. The dominant effect in the calculation of the toroidal flux arises from the change in the flux surface shape due to the elongation. Typically Alcator C-Mod plasmas in the flattop current phase have an edge elongation of about 1.6 decreasing to a value of about 1.2 at the axis with an approximate r^4 dependence, that is, $\kappa \approx 1.2 + 0.4(r/a)^4$. The approximate $1/R$ magnetic field dependence is to first order canceled out by the fact that the flux surfaces are approximately symmetric to the high and low field side of the magnetic

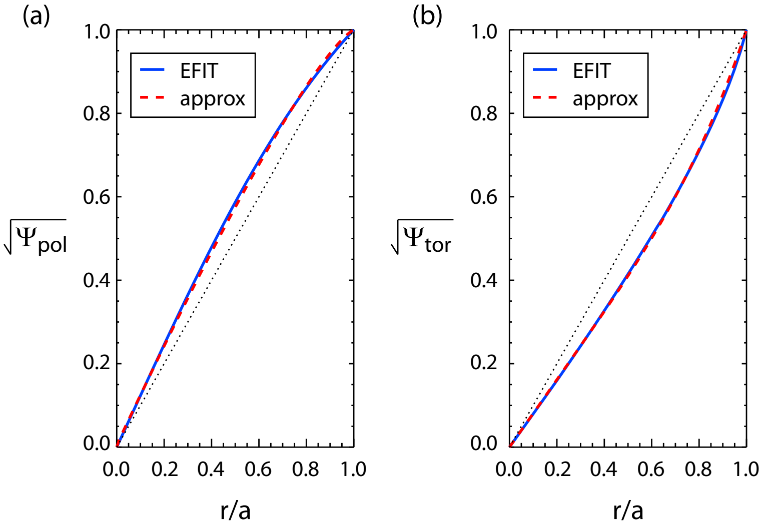

Figure 3-8: Approximate flux functions calculated from Eqs. 3.56 and 3.57 compared to relations calculated by EFIT for (a) the poloidal flux and (b) the toroidal flux. The dotted line in each case is the line $\sqrt{\psi} = r$, for reference.

axis. Strongly shaped "D" plasmas will of course break this approximation, and due to the fact that triangularity vanishes on-axis, tends to increase the relative fraction of the toroidal flux in the outer flux surfaces. With regard to the toroidal flux, the differential area element is approximated by $\mathrm{d}A \approx 2\pi\kappa r \mathrm{d}r$, ignoring the effect of triangularity. Expanding the field as $B_\phi \approx B_0(1 - \epsilon\, cos\theta)$ and recognizing that the $\cos\theta$ term vanishes in the integration, we have

$$\Psi_{tor}(r) \approx B_0\, \pi r^2\, \kappa. \tag{3.57}$$

A comparison of the $\sqrt{\Psi_{tor}}$ and $\sqrt{\Psi_{pol}}$ functions based on the previous approximations and the values calculated by EFIT is presented in Fig. 3-8. The simple approximations derived here agree with the EFIT relations within 4% and can be used as a general guide for converting between the various coordinates.

Sensitivity studies of NOVA have been performed to provide numerical uncertainties to the analysis of the RSAEs. The input parameters with the largest uncertainty are the plasma triangularity, plasma composition (Z_{eff}), the density profile, central q profile, and plasma rotation. The influence of each of these factors is discussed separately below. The remaining input parameters (temperature, central density, elongation, B_0, R_0, a) are thought to be well known and do not represent a major source of uncertainty. It should be mentioned that the pressure profile can have a significant effect on the Alfvén continuum, though this effect is more complicated and is explored in the subsequent chapters. Using a sum of squares uncertainty, $\Delta f_{tot}^2 = \Delta f_{tri}^2 + \Delta f_Z^2 + \Delta f_{dens}^2 + \Delta f_{rot}^2$, the sensitivity studies discussed subsequently have identified a net numerical uncertainty of approximately $20kHz$ for the RSAE solutions. This uncertainty in frequency translates to an uncertainty in q_{min} of order 10^{-3}, which means that inferences of q_{min} from MHD spectroscopic methods are quite accurate under the assumption that we have are including all relevant physics and have input parameters within the stated uncertainties.

Triangularity

While NOVA employs a full toroidal model, it operates with the simplifying assumption of an up-down symmetric plasma boundary. The dominant shaping effect is the elongation, followed by triangularity. Alcator C-Mod plasmas typically exhibit some degree of up-down asymmetry due to the development of diverted configurations which require a magnetic x-point (the vanishing of the poloidal magnetic field) created through the influence of the external magnetic coils. While the outer flux surfaces can be strongly triangular or "Dee" shaped, the plasma triangularity vanishes toward the center of the plasma so that the inner flux surfaces, and hence the

RSAEs are rather insensitive to these changes. This should be contrasted to the elongation which has a typical value of about 1.2 at the magnetic axis. The plasma triangularity has been scanned from $\delta = 0.0$ to $\delta = 0.6$ in 0.1 increments, and studied for $n = 3, 4, 5, 6$. This study found that the frequency of the modes increases approximately linearly with δ with an approximate 30 kHz spread over this range. Typically the difference in upper and lower triangularity is about 0.2 with an average value of about 0.45. Taking the average of these values, we can assign a practical uncertainty in δ of 0.1 to the equilibria which is equivalent to an uncertainty of about 5 kHz for the RSAE frequency.

Density Profile

The density profile enters as a source of uncertainty because of the temporally sparse measurements from the Thomson scattering system relative to the RSAE lifetimes. In Alcator C-Mod, a typical rise time for the RSAE to evolve from the minimum frequency to the TAE frequency is about 10 ms. The Thomson Scattering system measures profiles at 33 ms intervals. This effect is especially important during sawteeth, which with a typical period of about $(10-20)$ ms may have only one Thomson measurement. The density profile is not only important in the frequencies of the modes through its modification of v_A, but also in the measured density perturbations which scales as $\xi_r \rho_0' + \rho_0 (\nabla \cdot \xi)$, of which both terms are thought to be important for correctly modeling the density perturbations [11]. Assuming an error of 10% in the core density, we have an approximate 5% error in the frequency. Given an average frequency of approximately 300 kHz for the RSAEs, the uncertainty in the density profile amounts to a 15 kHz uncertainty in the frequency.

Rotation

The plasma rotation is an experimental uncertainty due to its rather sparse temporal and spatial measurements. The effect of plasma rotation is managed rather simply in NOVA, being taken as a simple Doppler shift of the frequency using the value of toroidal rotation at the peak of the eigenmode. A full account of rotation in the MHD equations considerably complicates the analysis and is often neglected under the assumption that the rotation contributes to a trivial Doppler shift and has small shear and can be neglected in the analysis. Near the core we expect the toroidal rotation velocity to be between 10 and 30 km/sec in the counter-current (ion-diamagnetic) direction during the current flattop phase [66]. This type of rotation produces a positive Doppler shift of between about $2 - 6\,\mathrm{kHz} \times n$, where n is the toroidal mode number. However, during the current ramp-up phase, with $q_{min} \approx 2$, the minimum frequency of the RSAEs can often be distinguished and the separate branches are seen to coalesce within a few kHz of each other, suggesting a negligible rotation during this period. Because the Alcator C-Mod plasmas do not exhibit a strong rotation and the Doppler shift may be of the order of the other uncertainties, we take the uncertainty from the Doppler shift to be $< 5\,\mathrm{kHz}$.

Central q profile

As will be shown later, the value of q_{min} and r_{min} can be well constrained by the PCI measurements. The value of q_0, however, does not have such strict constraints nor is it measured and is a source of uncertainty in the analysis. At this time, the best constraint on the q_0 comes from analysis with NOVA, which shows windows of viability for the RSAEs. Scans of q_0 while holding the other profile parameters fixed has resulted an approximate 5 kHz uncertainty over the range of viability.

Edge q profile

Due the strongly shaped edge profiles where a magnetic X-point may form, the q profile may become very large or even infinite. Because NOVA does not model such configurations an approximation or truncation for the edge q profile must be used. To study the effect on the RSAEs the value of the edge q profile has been scanned while keeping the central q profile fixed out to a radius of $r/a \approx 0.5$. This scan found that the RSAE frequency changes less than 2 kHz when q_a changes from 4 to 10. The physical interpretation of this scan is that the central current density is held constant while the total plasma current is decreased by nearly a factor of 2, meaning that the difference in current is confined to the region $0.5 \leq r/a \leq 1.0$. This study is more important for the operation of NOVA than it is in estimating a numerical uncertainty. In practice, one can never fully match the average β and the total plasma current (I_p) simultaneously for a given q profile. In this regard, a choice must be made to emphasize certain parameters over others. The relatively weak dependence of the RSAE frequency on edge parameters, including q_a, suggest that it is better to match the core q, density and pressure profiles. This means that the total plasma current is an effective free parameter which is used to provide global force balance. As will be discussed in chapter 4, the edge profiles have a significant impact on the edge amplitude of the RSAE eigenmodes, an important property for understanding detection of these modes by magnetic pick-up coils.

3.5.2 Overview of NOVA Solutions

The RSAEs appear to be most sensitive to the value of q_{min} and its radial position, here defined as r_{min}. While q_{min} determines to large extent the frequency of the mode, r_{min} strongly modifies the spatial scale of the RSAEs which results in a detectable difference in the synthetic PCI signal [18].

The remainder of this thesis will present an analysis of RSAEs excited during the current ramp phase and sawtoothing phase of tokamak plasma experiments. The current ramp phase is characterized by a state with a hollow current profile, equivalent to a reversed shear q profile, which arises because of the finite diffusion time for the electric field which, because it is imposed on the plasma by the Ohmic transformer, must diffuse in from the plasma edge. The RSAEs during the current ramp are most strongly observed when $q_{min} \approx 2$ and are often accompanied by strong TAE activity. In contrast, the RSAEs observed during the sawtooth cycle are localized near the $q = 1$ surface and are rarely accompanied by TAEs.

An Alfvén continuum from NOVA is shown in Fig. 3-9, representative of the profiles found during the current ramp-up phase. Multiple gaps are present with a collection of eigenmodes within each gap. The growth rates for these modes have been calculated with the result that the most unstable modes reside in the TAE gap, for minority tail temperatures up to 300 keV. Within the TAE gap, the most unstable mode is the RSAE with the gaussian-like radial displacement function. A series of higher order RSAE solutions, identified by the index l which measures the number of nodes in the radial eigenmode, may exist in theory, though in practice it is the $l = 0$ that is the most unstable. A few representative TAE gap eigenmodes, including $l = 1$ and $l = 0$ RSAE solutions, are presented in Fig. 3-10. The RSAEs are composed of a single dominant poloidal harmonic, and in the examples presented in Fig. 3-10 this is $m = 8$, with relatively weak sideband poloidal modes of $m = 7$ and $m = 9$. The scaling of the sideband amplitude derived in section 3.4, that is $\xi_{m\pm1}/\xi_m \sim 2(m - nq)/nq$ which is of order 0.1, is in agreement with the solutions shown in Fig. 3-10. In general, RSAEs exist near all rational values of q_{int}, and are characterized by a dominant mode number $m = nq_{int}$.

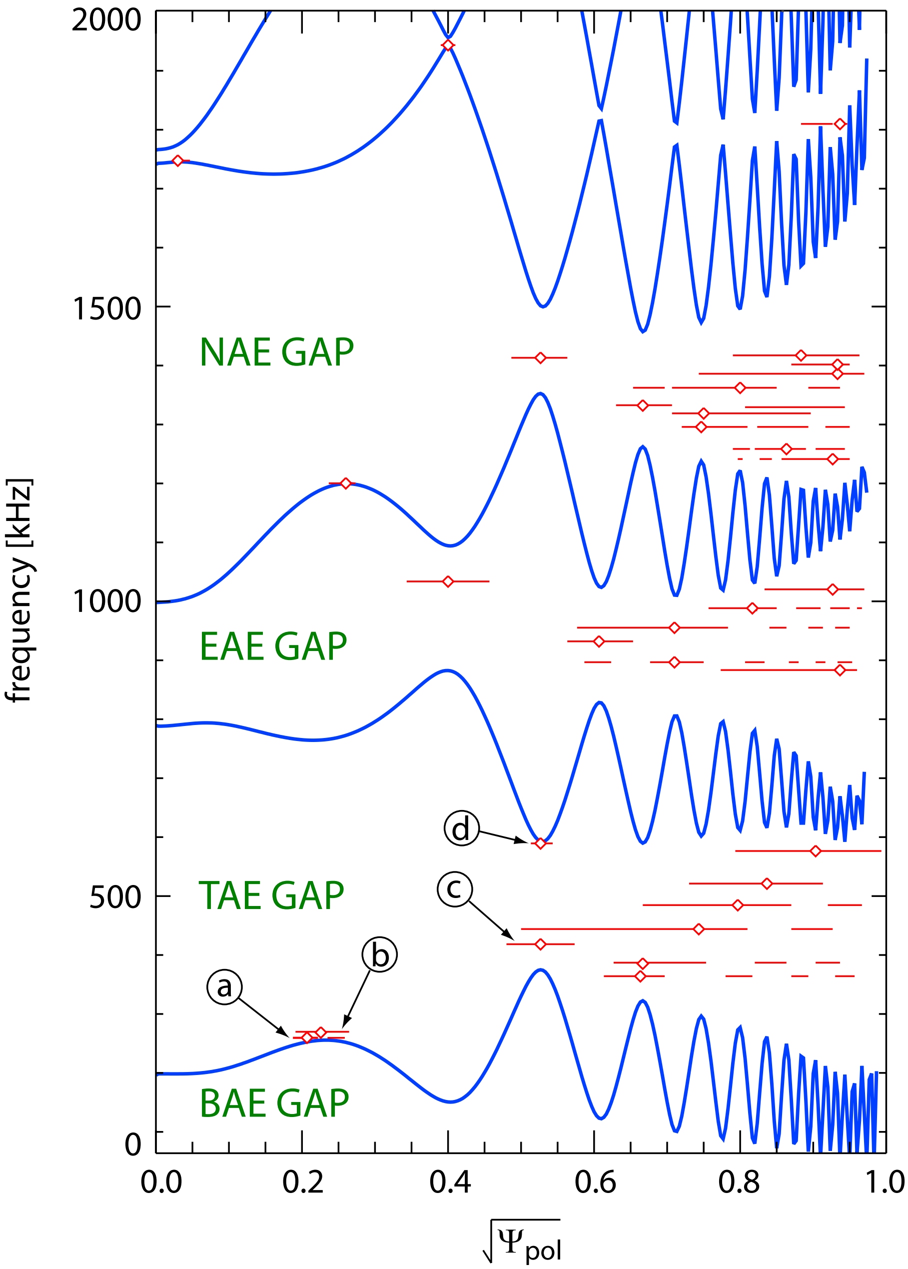

Figure 3-9: The n=4 Alfvén continuum calculated for current ramp-up conditions with $q_0 = 2.00$, $q_{min} = 1.95$ and $r_{min}/a = 0.25$. The overlaid mode lines represent the full-width half-max measure of the radial displacement eigenfunction, the diamonds denote the peak of the mode. The modes marked identified by (a), (b), (c) and (d) correspond to those shown in Fig. 3-10.

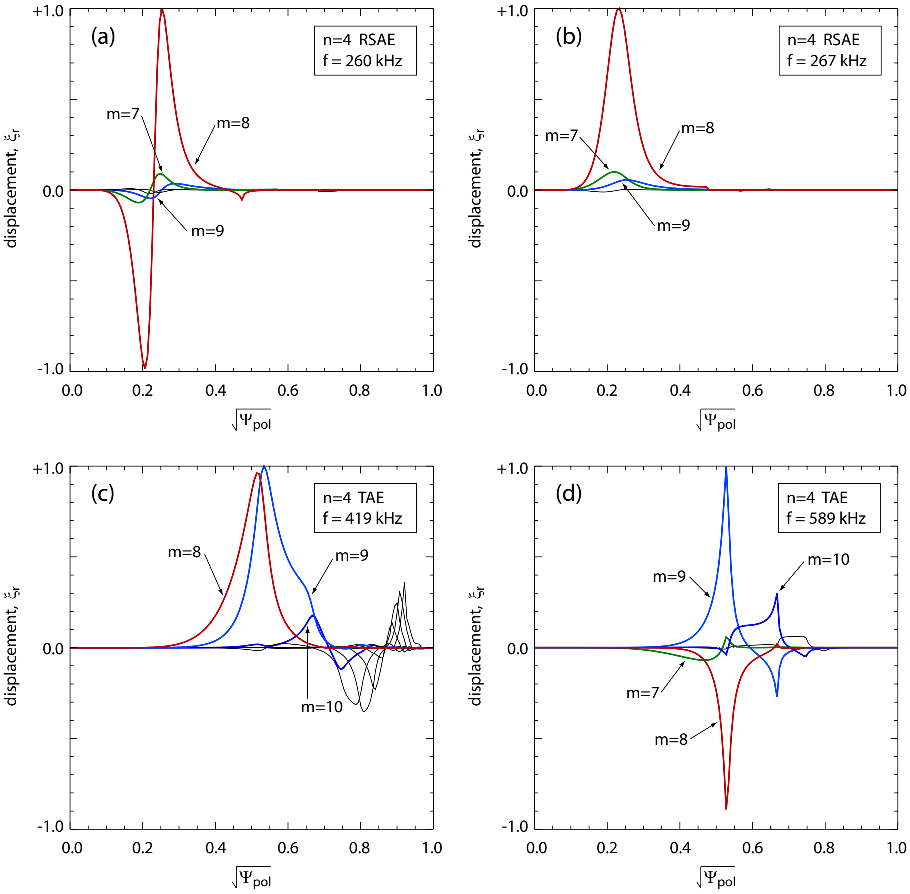

Figure 3-10: A set of representative solutions for the case presented in Fig. 3-9. Two RSAE and two TAE solutions are shown. Stability calculations show that only modes (b) and (c) can be unstable under experimental conditions.

3.5.3 NOVA-K

NOVA-K is the kinetic extension of NOVA which calculates the growth and damping rates of the eigenmodes [67]. Theoretical interpretations of the Alfvén wave-particle resonance can be found in [5, 68]. The energetic ion component, which is responsible for the drive of the Alfvén eigenmodes, can be specified in NOVA-K as either an ICRH distribution, beam distribution, or isotropic alpha particle distribution. For the purposes of modeling Alcator C-Mod experiments we use the ICRH distribution. The growth rates of the modes marked a-d in Fig. 3-10 have been calculated for an energetic ion population created with on-axis ICRH and a monotonically decreasing pressure profile, presented in Fig. 3-11. In this study the tail temperature (T_H) was scanned at constant energetic ion beta (β_H). This scaling means that as the temperature is increased, the particle density is decreased in equal proportion. The growth rates calculated by NOVA-K are linear in the number density, and hence linear with β_H for fixed T_H. As detailed information of the energetic ion distribution is fraught with uncertainties and is not well diagnosed in Alcator C-Mod at this time, this thesis will not focus much on these calculations. The summary of the growth rate studies is that the RSAEs observed both during the current-ramp and sawtoothing phases are calculated to be unstable under experimental conditions.

The net stability of the eigenmodes must also account for the damping, which is primarily due to Landau damping on the electrons and the majority ions. The minority and impurity ions will also contribute some damping, though this is usually much smaller on account of their relatively lower densities. The so-called “continuum damping”, properly a mode conversion process to kinetic Alfvén waves, should also be considered, but is not fully implemented in the present version of NOVA-K. Consideration of the growth rate and damping rate calculations show that of the

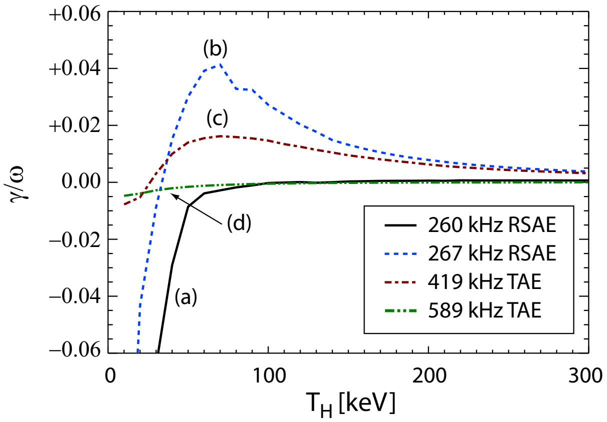

Figure 3-11: Growth rates calculated for the four modes identified in Fig. 3-10, using a monotonically decreasing energetic ion pressure profile.

four modes presented in Fig. 3-10, only cases (b) and (c) have a net positive growth rates. This calculation is in agreement with experiments in which only the $l = 0$ RSAE and the core TAE are observed. The maximum net growth rates (γ_{net}/ω) for these modes is calculated to be approximately 0.038 and 0.015, respectively, occurring at $T_H = 70keV$ for both.

The model distribution in NOVA-K is a 3-parameter function, given in Ref. [69] as,

$$F_H = F_0\, n(r)\ \exp\left[-\frac{E}{T_H}\right]\ \exp\left[-\frac{(\lambda-\lambda_0)^2}{\Delta\lambda^2}\right], \tag{3.58}$$

where F_0 is a normalization constant, $n(r)$ is the spatial density profile at the midplane, E is the particle energy, T_H is the distribution temperature, $\lambda = \mu B_0/E$ where $\mu = mv_\perp^2/2B$ is the magnetic moment, $\lambda_0 = R_{res}/R_0$ specifies the ICRH resonance radius, and $\lambda = \Delta R/R_0$ is the normalized resonance layer width. Two major effects combine to produce a finite resonance width: the finite frequency band of the

ICRH system (ΔR_{ICRH}), and the resonance width broadening due to thermal effects (ΔR_{th}). The finite spread in the launched wavenumber spectrum by the ICRH antennas do not significantly change the resonance width as the spectrum is approximately symmetric about the peak. The ICRH system on Alcator C-Mod typically employs frequencies of 80.5 MHz, 80.0 MHz, and 78.0 MHz for the D, E, and J antennas respectively. The launched waves are resonant with the plasma when the frequency equals (approximately) the minority ion cyclotron frequency ($f = f_{cH}$). The differences in antenna frequencies define different resonant layers which gives a maximum ΔR_{ICRH} of about 2 cm when all three antennas are used, and about 0.5 cm when only the D and E antennas are used. To calculate the resonance width due to the thermal broadening (Doppler shift) we consider the more accurate resonant condition, $\omega - \omega_{cH} - k_{\parallel} v_{th} = 0$. The parallel wave spectrum is set by the antenna structure and typically peaks around $n = 10$ for heating phasing. We define the parameter $\Delta\omega = k_{\parallel} v_{th} \approx n v_{th}/R_0$. As before, the relation between ω and B gives $R_{th}/R_0 \approx 2\Delta\omega/\omega_{cH}$, where the factor of 2 comes from the presence of a spectral peaks at ±10. This condition then gives $\Delta R_{th} \approx 2cm$ for a 3 keV background plasma. These effects should be combined through a convolution, though it will suffice to use a quadratic sum, $\Delta R \approx \sqrt{\Delta R_{ICRH}^2 + \Delta R_{th}^2}$ which gives 3 cm when all antennas are used and about 2 cm when the D and E antennas only are used.

3.6 Synthetic PCI

While the NOVA results presented in the previous sections are useful for assessing the frequency spectra or whether a mode may be unstable, they are not directly comparable to the spatial information which is supplied by the PCI system. To make a quantitative comparison of the spatial structure measured by PCI the two dimensional density perturbations calculated by NOVA are integrated along lines corresponding to the viewing chords of the PCI channels. These integrated signals can then be convolved with a system response function to simulate the effect of signal averaging over the finite detector width and the k-response of the phase plate. The method, and its sensitivities are outlined in the following as a reference for later chapters.

The density perturbation can be derived from the equation of continuity for mass, that is

$$\frac{\mathrm{d}}{\mathrm{d}t}\rho_m + \nabla \cdot (\mathbf{v}\rho_m) = 0, \tag{3.59}$$

where ρ_m is the mass density. The electron density can be calculated through Eq. 3.52 once the fractional densities (α_i, α_I) are known. With the assumption of a constant Z_{eff}, which incidentally is enforced by NOVA, the α_i and α_I parameters are constants and we can write simply $\rho_m = \alpha m_i n_e$, where α is a normalization constant. In this we may use the continuity equation to solve for n_e instead of ρ_m. Expanding to first order and using the plasma displacement we have,

$$\tilde{n}_e = -(\vec{\xi} \cdot \nabla) n_e - n_e(\nabla \cdot \vec{\xi}). \tag{3.60}$$

It can be seen in equation 3.60 that two effects are responsible for the density variation. The first term arises as the displacement accumulates density perturbation due to the non-uniformity of the profile, and the second term represents the effects of the compressibility, which vanishes in the limit $\gamma \to \infty$. As will be shown in chapter 4, the ideal gas approximation may be a decent approximation for shear Alfvén waves with respect to ion motions, but is certainly not satisfied for the electrons whose thermal speed can greatly exceed the phase speed of the wave. In this regard, we may expect γ to be somewhere between 1 and 5/3. This subject is examined further in section 4.3. As outlined in chapter 2, the PCI system measures the line-integrated electron density fluctuations, that is

$$I_{PCI} \propto \int \tilde{n}_e \, \mathrm{d}z. \tag{3.61}$$

Also discussed in the former chapter was the necessity of the diffracted beams to reflect off of the gold surface of the phase plate, while only the direct beam should be focused in the phase plate groove. For the very lowest k waves, the diffracted beams do not wholly land on the reflective surface. That fraction of the diffracted beams entering the groove, arising from scattering off of low-k plasma waves, can be considered effectively lost. The diameter of the incident gaussian beam at the phase plate is

$$d = \frac{4}{\pi} \frac{F \lambda_0}{D} \tag{3.62}$$

where F is the focal length of imaging system, λ_0 is the wavelength of the incident laser beam, and D is the diameter of the beam at the object plane [34]. The PCI system implemented on Alcator C-Mod uses a 203 cm focusing mirror. For a beam size with a diameter of 20 cm, the spot size at the phase plate is 0.4 mm, almost exactly the width of the groove in the phase plates used in these experiments. The separation between the diffracted beam and the direct beam at the phase plate is defined as s, which is related to d by

$$s = F \theta_{diffracted}. \tag{3.63}$$

Perfect imaging will then occur when $s > d$. Recalling that $\theta_{diffracted} = \lambda_0 / \lambda_p$, we

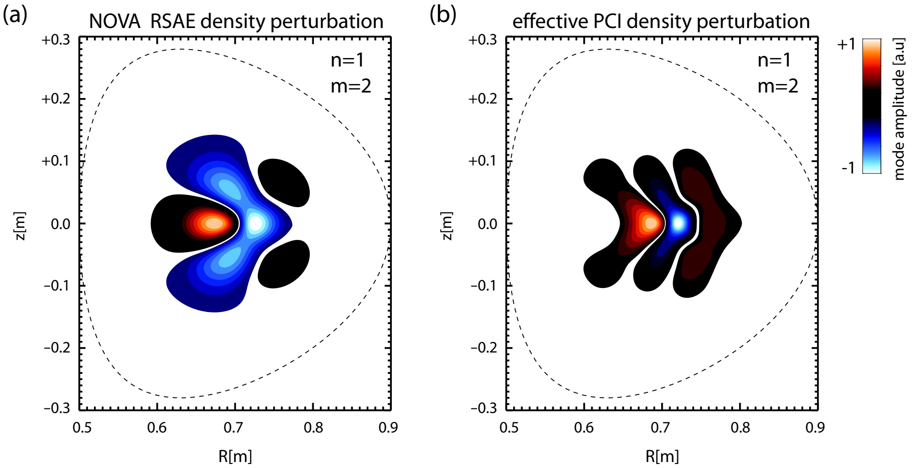

Figure 3-12: (a) The two dimensional density perturbation calculated by NOVA for the case of an n=1 RSAE and (b) the effective perturbation observed by PCI after applying the high-pass k-space filter.

have the requirement that $\lambda_{p,max} < (\pi/4)D$. For our experiments, this condition is $\lambda_{p,max} \approx 15\,\text{cm}$, or equivalently, $k_{min} \approx 0.5\,\text{cm}^{-1}$. Applied to the synthetic PCI, we can apply a gaussian high-pass filter to remove all k_p below this threshold. The effect of this filtering is illustrated in Fig. 3-12 based on NOVA calculations of an $n = 1$ RSAE with a very broad profile. The filtering of the NOVA model produces a more uniform structure, decreasing the peak amplitude and increasing the sidebands.

The general method of constructing the synthetic PCI signal begins with regularizing the two dimensional output of fluctuations from NOVA onto a rectangular grid, which is accomplished with standard IDL routines. Because the PCI beam path is vertical within an angular uncertainty of about 0.3°, the density fluctuations are integrated along vertical chords at the resolution of the grid spacing to produce a one dimensional image. This one dimensional image is then convolved with a gaussian kernel of a width equal to the effective width of the detector element at the system magnification. The PCI system was operated in the low-k configuration for the dedicated RSAE experiments with a $k_{min} \approx 0.5\,\mathrm{cm}^{-1}$ and $k_{max} \approx 8\,\mathrm{cm}^{-1}$ which correspond to a $\lambda_{max} \approx 10\,\mathrm{cm}$ and $\lambda_{min} \approx 0.8\,\mathrm{cm}$ respectively. The peak-to-peak spacing of the observed PCI signals are usually on the order of 2 cm and therefore well within the observational limit set by the optics. Finally, the calibration of the system must be included. As NOVA calculates only relative fluctuation amplitudes from a linear analysis, the absolute value of the signal is unimportant at this level of comparison. The relative channel to channel signal level of the PCI system however must be included. The separate channels on the detector can have different signal levels due to the non-uniformity of the laser beam across the detector and inherent differences in sensitivity. The calibration factor may be either divided into the experimental PCI signal or multiply the synthetic PCI signal. To avoid amplification of noise and background fluctuations the latter approach is followed, thereby making the synthetic PCI signal a full representation of the PCI system. Figure 3-13 shows how the effects of detector element convolution and calibration combine to form a final output signal. Note that integration through positive and negative density perturbations can result in a "phase cancelation" effect resulting in nodes in the observed spatial intensity structure.

The comparison between the synthetic PCI and experimental PCI signals can be quantified through the use of a correlation coefficient. The simplest measure of correlation is the least squares sum, that is, $\chi = \sum_i (A_i^{syn} - A_i^{exp})^2$ where A_i^{syn} and A_i^{exp} are the amplitudes of the i^{th} channel in the synthetic and experimental signals respectively. Two free parameters are used to minimize the value of χ for each comparison. The first is the radial reference point of the experimental PCI. At the time of these experiments the channel to channel spacing was calibrated, but the absolute radial position of the array was not well defined. The second free parameter

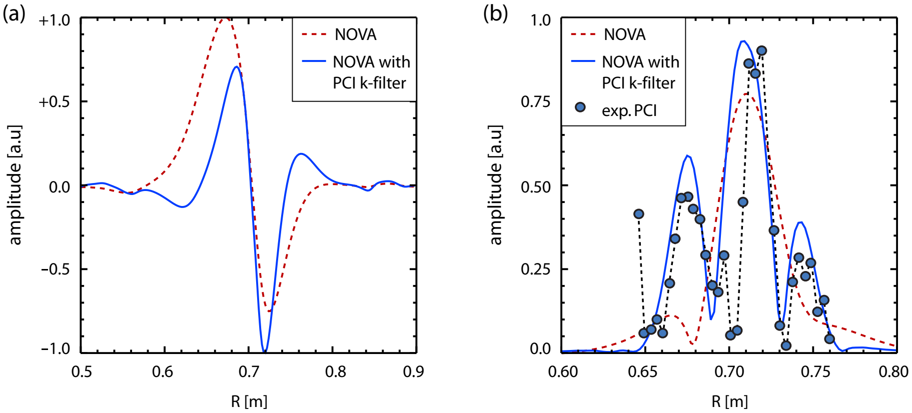

Figure 3-13: (a) The integrated data from Fig. 3-12 comparing the unfiltered and k-space filtered signals, and (b) comparison with experimental data.

is the absolute value of the synthetic PCI signal which is representative of the fact that NOVA calculates only relative fluctuation levels. The example shown in Fig. 3-13 is representative of a "good" fit to the PCI data. The primary feature to match in the data is the peak to peak spacing, which is a strong function of the parameter r_{min} [18]. The relative amplitude of the peaks is related to the magnitude of the LFS/HFS asymmetry which arises because of the competing effects of the density gradient and finite compressibility in the $\tilde{n}$ relation.

Chapter 4

Reversed shear Alfvén eigenmodes during the current ramp

Three goals motivate the study of RSAEs during the current ramp phase of tokamak plasmas. The first is simply that the current ramp provides conditions in which hollow current density profiles (reversed shear q profiles) occur as the Ohmic current diffuses toward the plasma core and therefore provides an excellent opportunity to study RSAEs. The second, an extension of the first, is that analysis of the RSAE frequency spectra results in an independent measure of q_{min} as a function of time, which has utility in verifying the measurements of other diagnostics or for validating models of the current profile evolution. Lastly, these experiments sought to develop a means by which the advanced tokamak (AT) operating regime may be reached rapidly and efficiently. The AT scenario is characterized by a broad, reversed shear q profile with $q_{min} \approx 2$, which is thought to result in enhanced bootstrap current (self-generated current), reduced MHD activity and operation without sawteeth [13, 40, 70]. Attainment of the AT regime, however, is a non-trivial task in high temperature, high current tokamak plasmas. The Ohmic current tends to peak at the magnetic axis in approximate conformance with a $T_e^{3/2}$ profile (modified by neoclassical effects) and consequently results in a monotonic q profile with $q < 1$ (on average) at the magnetic axis, a state far from anything resembling the AT scenario. One path to developing an AT scenario is to use early injection of ICRH to heat the plasma and retard the penetration of the current long enough such that auxiliary current drive mechanisms, such as lower-hybrid current drive (LHCD), can be employed to drive additional current off axis and maintain the AT current profile [37]. Coincidentally, reversed shear q profiles and energetic ions (from the ICRH) are precisely the necessary ingredients for the excitation of RSAEs.

With regard to the goals discussed previously, the RSAE ramp-up experiments in Alcator C-Mod can be considered successful on the first two counts and progress on the latter. The general understanding of Alfvén eigenmodes has progressed significantly over the last six years, both theoretically and experimentally. The effort to arrest the current penetration seems to have encountered difficulties in Alcator C-Mod. Compared to experiments without early ICRH, there is no significant delay in the onset of sawteeth, an unambiguous sign of the presence of a $q = 1$ surface and is a benchmark for assessing the rate of current penetration. Application of early ICRH into low density, wall limited plasmas typical of the start-up phase has the negative consequence of increasing the plasma Z_{eff}, where $Z_{eff} = \sum_j (n_j \, Z_j^2 / n_e)$ and j is an index over ion species. The plasma resistivity is proportional to the product of $T_e^{-3/2}$ and Z_{eff}. A time scale for the resistive diffusion of the plasma current can be derived from Maxwell's equations and the parallel Ohm's Law ($E = \eta j$) to give $\tau_\eta \sim \mu_0 a^2 / \eta$, where η is the plasma resistivity. Taking the diffusion scale length to be the minor radius (20 cm), a profile averaged temperature of 1 keV and $Z_{eff} \approx 4$ as representative of Alcator C-Mod during the current ramp gives $\tau_\eta \sim 100$ msec. This

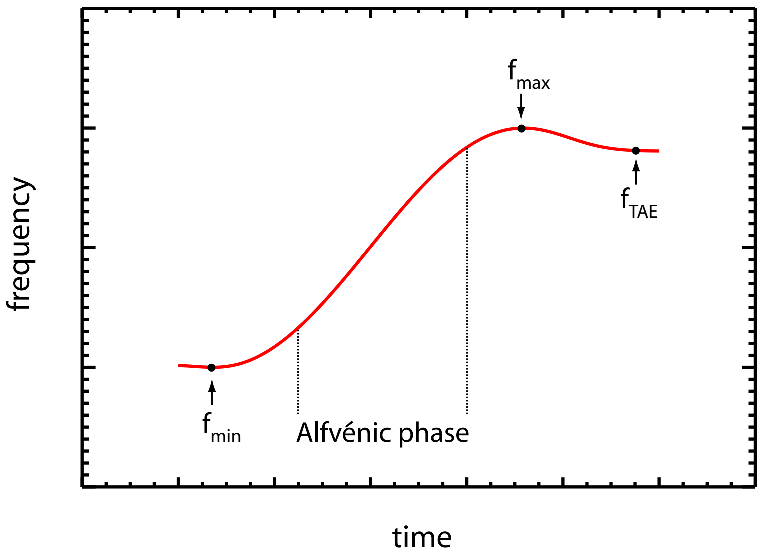

Figure 4-1: The RSAE frequency sweeps upward as the equilibrium evolves and q_{min} decreases. The analysis of the RSAEs can be divided into three main regions: the minimum frequency, the Alfvénic phase where $\omega \approx k_{\parallel} V_A$, and the maximum frequency and transition to the TAE.

fundamental scaling suggests that progress toward development of an AT scenario requires a low Z_{eff} and is best suited to larger devices which have inherently longer resistive time scales on account of the a^2 dependence.

As a means of analysis, the RSAEs provide a very sensitive tool for inference of the evolution of q_{min}. The method of inferring the evolution of equilibrium parameters from the frequency of MHD modes is referred to as "MHD spectroscopy". This method relies on inverting a dispersion relationship, $\omega = \omega(\vec{k}; q, T_e, n_e, ...)$, to solve for an unknown parameter when ω and $\vec{k}$ are known. In the case of Alcator C-Mod experiments the q profile can be considered essentially a free parameter, therefore the RSAE dispersion relationship is inverted to solve for q_{min}(t). The ideal MHD code NOVA [64], the primary theoretical tool used in this work, provides an extension of the method of MHD spectroscopy technique to compare numerical and measured spatial structures which can then provide additional constraints on the shape of the q profile. Analysis of the RSAEs can be split into three major phases: the minimum frequency, the Alfvénic phase, and the maximum frequency phase where the RSAE enters the TAE (toroidicity-induced Alfvén eigenmode) gap, illustrated in Fig. 4-1. This chapter continues with a discussion of the experiments, analysis of the Alfvénic phase and minimum frequency, and followed by two additional interesting physics subjects.

4.1 Overview of Experiments

The experimental approach for the excitation of RSAEs during the current ramp combines a relatively fast current ramp ($dI_p/dt_{max} > 6MA/s$ at 50 msec) with early ICRH starting around 75 to 100 msec. An overview of the experiment comprising the focus of this chapter is presented in Fig. 4-2. Ion cyclotron resonance heating (ICRH) is a critical component of these experiments, creating the energetic ion population which provides the free energy for the modes [5]. The plasma density may be the most important experimental knob, affecting both the energetic ion population and the impurity concentration in opposing trends. Assuming a constant impurity source (perhaps arising from the interaction of the launched ICRH waves and the first wall or antenna structure), Z_{eff} scales approximately as n_e^{-1} which suggests that higher densities are desirable to keep the resistivity low. On the other hand, the slowing down time for energetic ions also scales as n_e^{-1}, indicating a bias for lower densities to achieve high temperature (~100 keV) ion tails necessary for RSAE excitation. Experimentally, the best results have been observed with line integrated densities in the range $0.4 \times 10^{20}\, m^{-2}$ to $0.7 \times 10^{20}\, m^{-2}$ (central densities of approximately

$1.0 \times 10^{20}\, m^{-3}$ to $1.7 \times 10^{20}\, m^{-3}$) and injected power in the range of 2.5 MW to 4.0 MW. Some experiments (see in particular 1080228017) have noted a critical threshold power of about 1.4 MW injected power from the J-port ICRF antenna, after which the radiated power rises steeply, indicating an influx of impurities into the plasma. A delicate balance must be struck between generation of an energetic ion population and the overall machine performance. The most successful experiments in terms of RSAE excitation occurred on July 9, 2003 (1030709) and April 6, 2004 (1040406). Of these experiments, shot 1040406018 is considered the finest example, exhibiting clear RSAEs, good diagnostic response and utilizing only 2.8 MW of injected ICRH power during the current ramp with a line integrated density of approximately $0.4 \times 10^{20} m^{-2}$.

Shot 1040406018 was run with a toroidal field of 5.4 Tesla and used a lower-single null magnetic configuration with the plasma current in the negative direction (parallel to the magnetic field). Most of the diagnostic systems used in this analysis are described in greater detail in Ref. [71]. The line-integrated density is measured by the two-color interferometer (TCI) from which the average density is calculated by dividing by chord length, and the density profile is measured by the Thomson scattering system. The electron temperature profile is measured with the electron cyclotron emission (ECE) diagnostic, and the ion temperature is inferred from the measured neutron flux from D-D fusion reactions. The most uncertain quantity in this collection is the Z_{eff}, which is derived from measurements of the visible Bremsstrahlung. Though Z_{eff} is most certainly a spatially dependent quantity [72, 65], the Z_{eff} reported in Fig. 4-2 is a profile average value. In Alcator C-Mod plasmas with ICRH the main impurity species is molybdenum, which may exist in the core as Mo^{+31} or Mo^{+32}. The presence of high Z impurities means that the Z_{eff} may increase rapidly for a rather modest fraction of impurity, for example, a plasma with a Z_{eff} of 4 and $Z_I = 31$ has an impurity fraction (n_I/n_e) of approximately 3×10^{-3}.

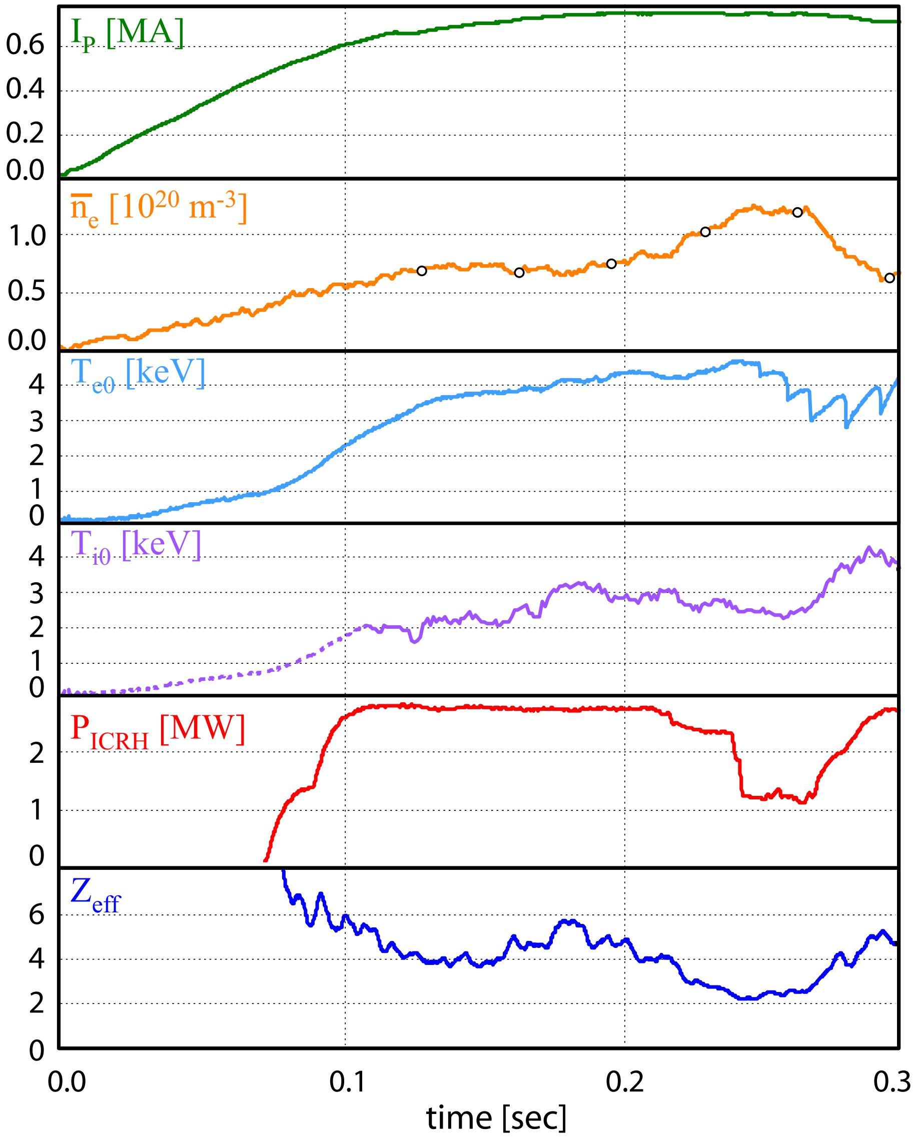

Figure 4-2: Plasma parameters for shot 1040406018. From top to bottom: plasma current (I_p), line-averaged density ($\bar{n}_e$), central electron temperature (T_{e0}), central ion temperature (T_{i0}), injected ICRH power (P_{ICRH}), and average Z_{eff} (Z_{eff}). The circles on the $\bar{n}_e$ trace denote the times at which density profiles measurements are available from the Thomson scattering diagnostic. T_{i0} data is not available for $t < 0.1 sec$ and is taken to be equal to $0.75\,T_{e0}$ for this period (dashed line).

High Z impurities have little impact on the frequency or structure of MHD modes, only slightly modifying the mass density, and hence the Alfvén speed, in proportion to the impurity charge density multiplied by the differences of the impurity and main species mass to charge ratios. The impurities may have more modest changes to the ion Landau damping of the Alfvén eigenmodes, which scales as the ion density, and also the plasma resistivity which is especially significant for modeling the current diffusion.

Representative PCI and magnetic spectrograms for shot 1040406018 are shown in Fig. 4-3, capturing the entirety of RSAE activity during the current ramp. The central feature of these spectrograms is the so called "grand cascade", starting near 0.135 sec and 200 kHz, where multiple RSAEs arise from a common minimum frequency and increase in frequency at rates approximately proportional to their individual toroidal mode number. During the Alfvénic phase of its evolution, the RSAE is well modeled as an eigenmode toroidal of toroidal mode number n and a dominant poloidal mode number m. The simultaneous excitation of multiple modes in the grand cascade pattern is indicative of q_{min} crossing through an integer surface, in the case in Fig. 4-3 it is $q_{min} = 2$. The presence of multiple modes at integer q_{min} arises because the relation $m = nq$ can be satisfied for an infinite set of (m, n) when q is integer. The subject of mode stability is not presented here, rather the discussion of energetic ion distributions in chapter 3, which is based on former experimental and theoretical studies for Alcator C-Mod [44], is referenced as an argument for the general instability of RSAEs under these conditions.

In addition to their utility in providing a method for inferring the evolution of q_{min}, the RSAEs observed during the current ramp present many subtle and complex physics problems, three of which will be the focus of this chapter. The first is a study of the scaling of the minimum frequency of the RSAEs the limit $k_\parallel \to 0$ which provides

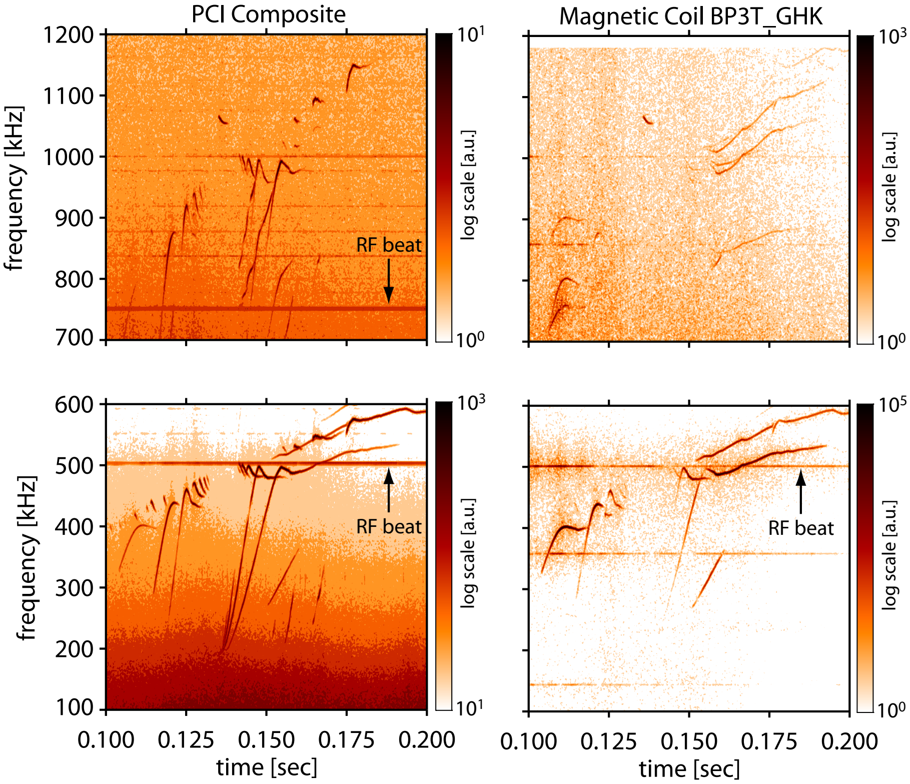

Figure 4-3: Spectrograms of the current ramp phase of shot 1040406018 during which RSAEs are observed. The spectrograms on the left represent the average of all PCI channels and the spectrograms on the right are from magnetic coil BP3T-GHK. The spectrograms are split in frequency to enhance the resolution of the weaker, high frequency modes, a second order plasma response. The blank region above 1180 kHz in the magnetics spectrogram is representative of the Nyquist sampling frequency of the data acquisition system.

constraints on the adiabatic index of the plasma. Another important result is that during the Alfvénic phase, the RSAEs are observed quite strongly with the PCI diagnostic but much more faintly on the Mirnov coils located outside the plasma. The ratio of the magnetics signal to the PCI signal may be interpreted as a measure of a "tunneling" process through a forbidden region. Lastly, the observation of RSAE harmonics are evidence of a second order plasma response.

4.2 MHD spectroscopy

The goal of MHD spectroscopy is to utilize the information in the spectral characteristics of observed modes to infer certain properties of the plasma equilibrium. In the Alcator C-Mod experiments the q profile is not well known, at least in the plasma core where EFIT reconstructions have larger uncertainty, derived from an *a priori* model of the current profile. The presence of multiple RSAEs with different rates of frequency sweep allows the mode numbers to be determined unambiguously by matching the theoretical predictions to the observed pattern of modes, with the results that the evolution of q_{min} may be determined. Even in the absence of direct measurement of the mode numbers (for example with magnetics), the existence of a unique pattern of RSAEs unambiguously links them with a specific set of mode numbers. This technique is illustrated in Fig. 4-4 which uses a collection of 600 NOVA runs to model the evolution of the RSAEs as q_{min} decreases during the current ramp. The set of Mirnov coils used during these experiments were composed of two groups separated by approximately 180° in toroidal angle which is not optimal for the resolution of low n modes. They can however, determine the evenness or oddness of a mode, and within this limitation confirm the mode numbers as determined by fitting the NOVA results to the observed PCI spectra.

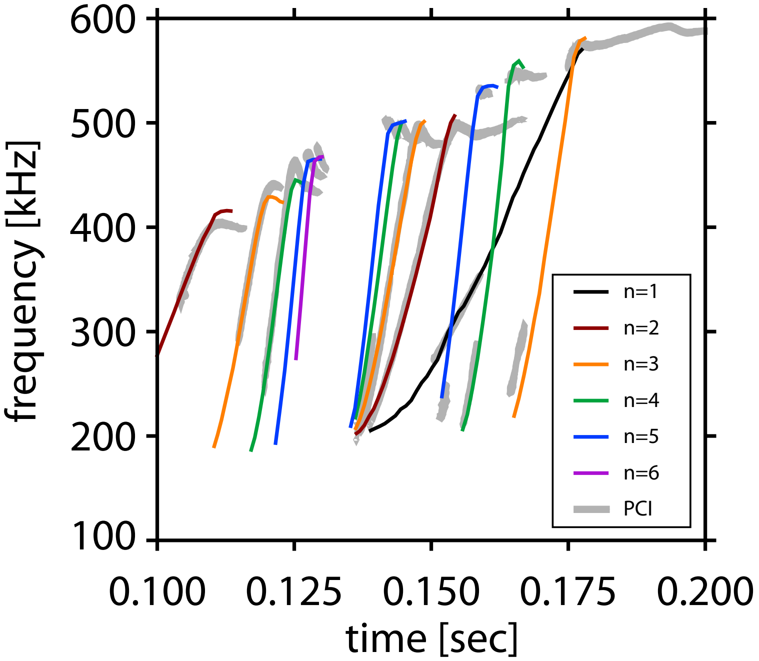

Figure 4-4: NOVA calculations are compared to the experimental RSAE signals measured by PCI to infer the evolution of q_{min}. The fit shows the largest disagreement as the RSAEs evolve into TAEs, but elsewhere shows good agreement.

The cessation of RSAEs near 170 msec is likely due to a decrease in the radial position of q_{min}, defined here as r_{min}, which causes the RSAE frequency to move closer to the Alfvén continuum which results in increased damping. Eventually, the q profile becomes monotonic at some time between the last RSAE and the start of the sawteeth at 240 msec. In this intervening period no constraints on the q profile can be determined. During the sawtoothing phase q_{min} remains close to unity, perhaps dropping as low as 0.92 and rising to a maximum of about 1.03 [19]. The constraint of $q = 1$ from the sawtoothing phase together with the RSAE spectroscopy result in a map of q_{min} over the time range of 100 ms to 250 ms, as in Fig. 4-5. The slight, but significant decrease in the average slope of q_{min}(t) during the period between the last RSAE and the first sawtooth crash is bounded by the curves $(\mathrm{d}/\mathrm{dt}) \ln q = constant$ and $(\mathrm{d}/\mathrm{dt}) q = constant$. These *ad hoc* forms can be interpreted in the former case as a diffusive response to a temperature profile which is approaching steady state, and in the latter case as a response to a steadily increasing temperature profile. The ECE data (see Fig. 4-2) confirm that while the temperature continues to increase during the period between the RSAEs and the sawteeth, the rate of increase is greatly reduced compared to the period of Alfvénic activity. The actual trajectory of q_{min} can then be understood as some average of these ad hoc trajectories.

While not exactly spectroscopic in nature, the extension of the method to include an analysis of the spatial structure of the modes can reveal additional information regarding the evolution of r_{min}. The PCI diagnostic is able to resolve a spatial structure corresponding to the vertically line-integrated density perturbations, appropriately modified by the system response function (see section 3.6 for discussion of this point). Similarly, a synthetic PCI signal can be generated from the model density perturbations calculated by NOVA or other codes. Many tests of the synthetic PCI have shown that the variation of the parameter r_{min} yields robust variations

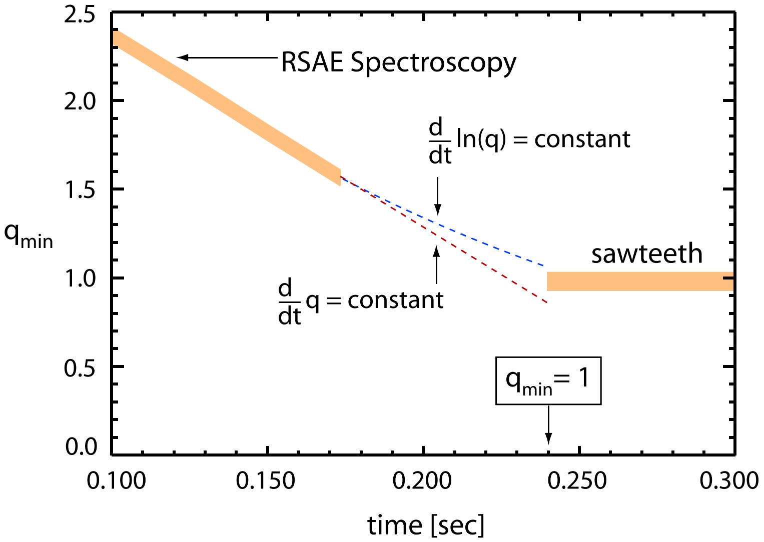

Figure 4-5: The evolution of q_{min} determined from the MHD spectroscopy. The point $q_{min} = 1$ is determined from the start of the sawteeth, which are observed in the T_{e0} trace in Fig. 4-2 to start around 0.24 seconds.

in the output. Specifically, the spacing between the peaks in the synthetic PCI structure vary approximately linearly with r_{min}. It is tempting to try to resolve the remaining discrepancy between the model and the experimental spatial structures through variation of another parameter such as q_0, that is, q at the magnetic axis. An eigenmode often becomes strongly peaked at the point where it encounters the Alfvén continuum. Small changes in the parameter q_0, or the profile curvature, can significantly modify gradients, and hence the density perturbations, near the point of continuum interaction. Ultimately, the resolution of the discontinuities near the points of continuum crossing should be viewed with skepticism, as FLR corrections are needed to properly model this region [55]. The summary point is that while the variations of r_{min} manifest as a robust representation in the peak spacing, which is rather insensitive to other changes, it is not possible to reliably infer q_0 based on

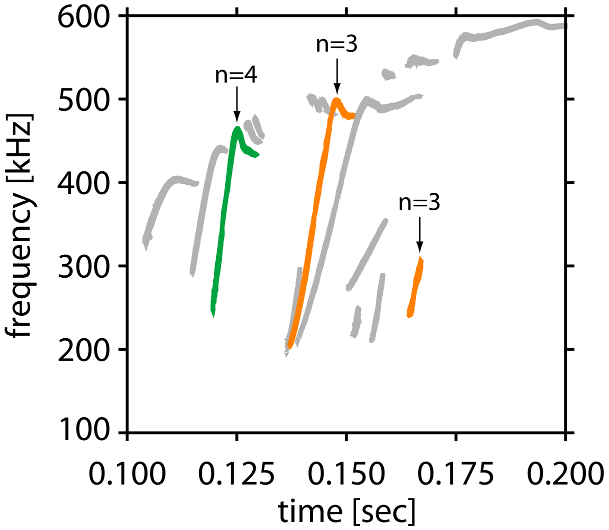

Figure 4-6: Filtered PCI spectrogram highlighting the three modes presented in the subsequent analysis used to derive constraints on the q profile.

variation of the remaining features. This work concludes that a more accurate modeling of the continuum interaction will be needed to account for the observed spatial structures, and hence, NOVA is simply not equipped to provide answers at this level of detail.

The comparison between the synthetic PCI model and the experimentally measured spatial structures can be quantified with a correlation coefficient. The simplest representation of the correlation is a single scalar value, which in this analysis is defined as

$$\chi^2 = \sum_{i=1}^{32} (F_i^{exp} - F_i^{syn})^2, \tag{4.1}$$

where i is an index representing the 32 PCI detector channels and the F_i^{exp} are the experimental PCI amplitudes for each channel and the F_i^{syn} are the synthetic PCI signals at the same radial positions as the experimental data. Because NOVA is a linear code and cannot predict an absolute amplitude, the comparisons are performed in a normalized scale with the experimental data scaled to have a maximum value of 1. Using this normalization, we can establish some rules of thumb for when correlations can be considered good or bad. A bad fit can be considered one in which, on average, each F_i^{syn} differs from the F_i^{exp} by about 1/4, which yields a χ^2 of 2. A case in which each F_i^{syn} differs from the F_i^{exp} by 1/8 (roughly 10%) may be considered a decent fit and yields a χ^2 of 1/2. In some cases the optimal fit may have a relatively high χ^2 on account of outliers which strongly weight the correlation.

Some of the fits, such as the solutions presented in Figs. 4-7 through 4-9, are remarkably close to the experimental data. In all cases, however, the synthetic PCI signal does not match the PCI signal perfectly, with the largest differences in the side lobes. As mentioned previously, such details may be the result of a complex interaction between the eigenmodes and the Alfvén continuum. Nonetheless, the results of the spectral and spatial analysis can be assembled to reconstruct the q profile evolution over the period in which the RSAEs are present. Figure 4-10 summarizes these results. In addition to improving the modeling of the Alfvén eigenmodes near points of continuum interaction, the method of MHD spectroscopy outlined here could be greatly complemented by some independent measure of q_0, or even the change in q_0. Together, these data would provide fairly tight constraints on the shape of the core q profile.

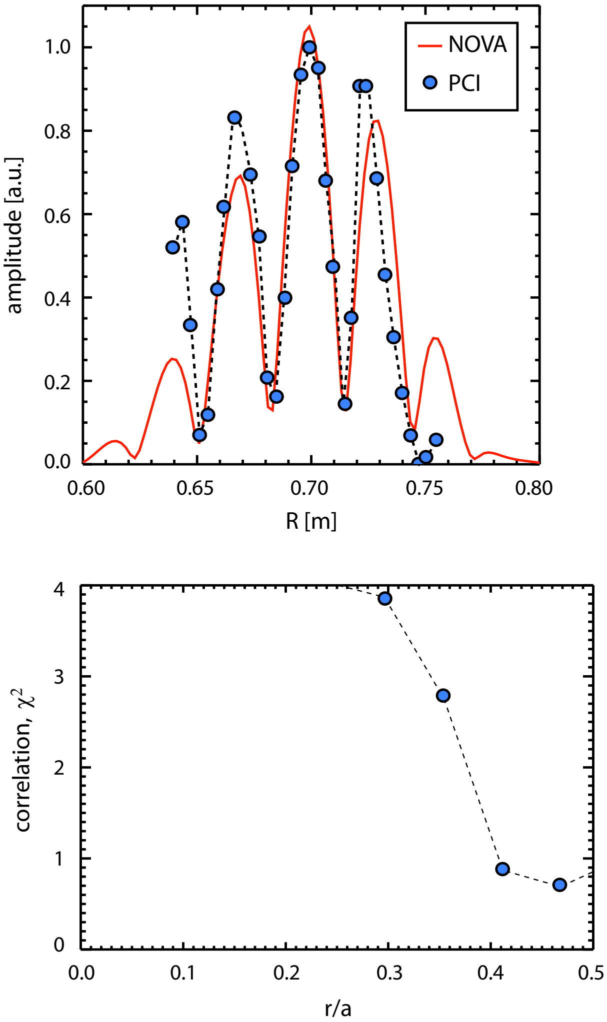

Figure 4-7: Best fit synthetic PCI solution and the correlation as a function of r_{min} for the $n = 4$ RSAE near 0.125 s.

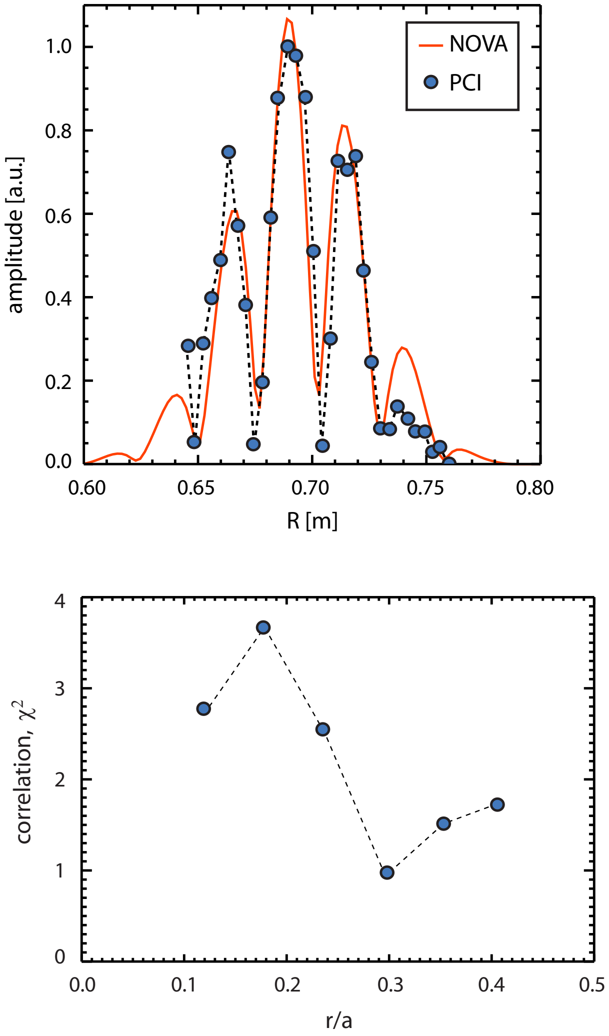

Figure 4-8: Best fit synthetic PCI solution and the correlation as a function of r_{min} for the $n = 3$ RSAE near 0.140 s.

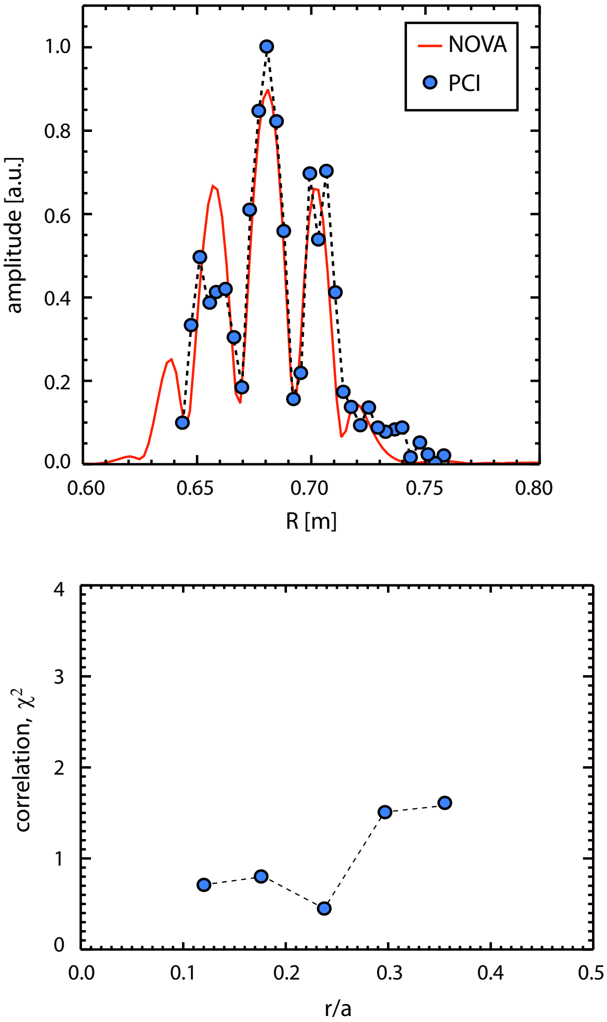

Figure 4-9: Best fit synthetic PCI solution and the correlation as a function of r_{min} for the $n = 3$ RSAE near 0.160 s.

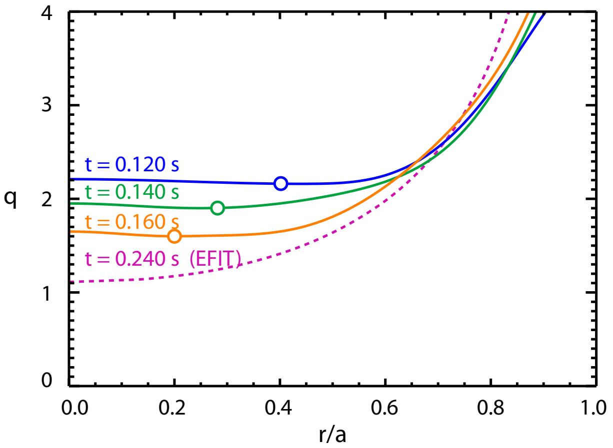

Figure 4-10: Reconstructed q profile from MHD spectroscopy and the synthetic PCI analysis. The final EFIT solution at 0.240 s is representative of the q profile at about the time that sawteeth start, though is still calculated to have $q_{min} > 1$, an obvious flaw in the calculation.

4.3 The RSAE minimum frequency

As q_{min} passes through integer values, or certain other rational values given by $q_{min} = m/n$, $k_{\parallel}$ will vanish and so too will the Alfvénic component of the perturbation. In the limit $k_{\parallel} \to 0$ the RSAE is strongly modified by the geodesic acoustic wave branch [63] and approaches a minimum frequency different from zero. In the parlance of Alfvén eigenmode theory, the Alfvén continuum is deformed by the geodesic acoustic branch [60]. The result is the addition of a minimum frequency offset to the RSAE dispersion relationship, simply represented as $\omega^2 = \omega_{min}^2 + k_{\parallel}^2 v_A^2$, which has the characteristic form as illustrated in Fig. 4-1. Near the minimum of the frequency sweep it is no longer possible for the plasma to respond as an incompressible fluid. The absence of fluid motion parallel to the magnetic field means that it becomes increasing difficult for the plasma to simultaneously satisfy $\nabla \cdot \xi = 0$ and $\nabla \cdot \mathbf{B} = 0$. Obviously, the divergence of the magnetic field imposes the stronger requirement, forcing a non-zero compression. It should be noted that even for $k_\| \neq 0$ the plasma responds with $\nabla \cdot \xi \neq 0$, but that this divergence becomes significantly larger as $k_\| \rightarrow 0$ (see pages 261-264 in Ref. [36] for further discussion of these points). The perturbation of the parallel magnetic field is proportional to $(\nabla \cdot \xi)$, implying that finite compressibility results in a compressional Alfvén wave component. A back of the envelope calculation taking $n_1/n_0 \sim 10^{-2}$ and B_0 of order 5 Tesla shows that the energy in the wave fields can increase by an order of magnitude due to the fact that $\mathbf{B}_1 \cdot \mathbf{B}_0 \sim B_0^2(\nabla \cdot \xi)$ as $k_\| \rightarrow 0$, a sign of enhanced stability. Generally, the most unstable modes are those that minimize $\nabla \cdot \xi$ [36].

Experimentally, the minimum frequency and lower portion of the Alfvénic phase of the RSAE evolution are often observed at amplitudes smaller by about an order of magnitude than those in the later Alfvénic phase. It is interesting that there is an analogous numerical difficulty with finding RSAE solutions in NOVA when $m/n - q_{min} \lesssim 0.02$, near the bottom of the frequency sweep. Apparently, NOVA does not fully resolve the $k_\| = 0$ states. In practice, the minimum value of the frequency can be inferred from NOVA solutions at finite $k_\|$ by extrapolation to $k_\| = 0$, as illustrated in Fig. 4-11.

The implementation of MHD theory in NOVA uses a single fluid equation of state defined as $\mathrm{d}/\mathrm{d}t(p/\rho^\gamma) = 0$, where p is the plasma pressure, ρ is the mass density and γ is the thermodynamic adiabatic index [64]. In classical thermodynamics the adiabatic index is directly related to the number of degrees of freedom of the system through $\gamma = (N + 2)/N$, where N is the degrees of freedom. A highly compressible gas with many degrees of freedom can be described as having $N \rightarrow \infty$ and a limiting value of $\gamma = 1$. At the other extreme, a one dimensional gas has $\gamma = 3$. An ideal gas

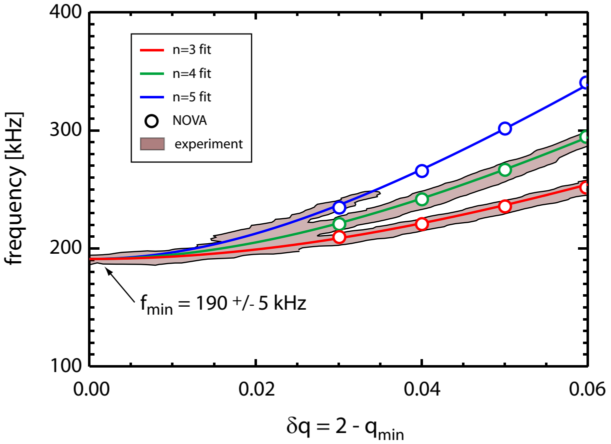

Figure 4-11: Comparison of NOVA results (circles) to the experimental PCI data (shaded region). The fit to the NOVA data allows for extrapolation into the region near the minimum of the frequency sweep where NOVA solutions are not found.

with $N = 3$ has the well known adiabatic index of 5/3. One may make a theoretical extension to a zero dimensional system, yielding $\gamma \to \infty$, which is the mathematical limit in which an incompressible gas should be considered. A proper treatment of the MHD equations yields the relation $\lim_{\gamma\to\infty}(\nabla \cdot \xi) = 0$. The physical interpretation of incompressibility is that the fluid mass is not only conserved, but the fluid density is constant along streaming trajectories, at least to first order. A fluid may in general have finite pressure and pressure perturbations even when incompressible, and it is interesting to note that while $(\nabla \cdot \xi)$ vanishes, the product $\gamma(\nabla \cdot \xi)$ appearing in the pressure perturbation is finite (see Eq. 3.15). The point of this discussion is to highlight the complexity of even a simple equation of state, and this even without attempting to provide a theoretical argument for what particular value of γ should be used. Though this equation of state is certainly a simplification of the physics, by taking γ as a free parameter one can seek an optimal fit to the experimental data.

Comparison of the experimentally measured minimum frequency with that calcu-

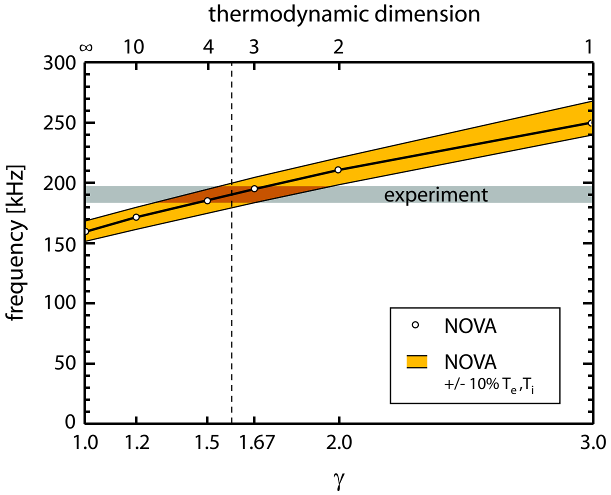

Figure 4-12: Comparison of the theoretical minimum RSAE frequency plotted as function of the adiabatic index (γ), to the experimental minimum frequency derived from Fig. 4-11. γ is an effective free parameter in the NOVA analysis.

lated by NOVA as γ is varied is presented in Fig. 4-12, showing a $\gamma^{1/2}$, expected from the scaling of the plasma sound speed, $c_s^2 = \gamma(T_e + T_i)/M_i$. The intersection of the gray band (the experimental frequency range) and the yellow band (the numerical frequency range) suggests that the effective plasma γ falls in the range of 1.5 to 1.7. Note that the ideal adiabatic limit of 5/3 (1.67) is very close to the upper limit from the analysis. When the dispersion relationship is dominated by the Alfvénic term, $\gamma \approx 5/3$ is anticipated on the grounds that $v_{th} \ll v_{phase,\parallel} = v_A$. While this condition is always true for ions, it fails for the electrons. Typical C-Mod parameters give $v_{th,e} \approx 2 \times 10^7$ m/s and $v_A \approx 1 \times 10^7$ m/s. Among other things, the apparent bias toward $\gamma < 5/3$ may be attributed to a non-adiabatic electron response. The problem becomes more complicated as $k_\parallel \to 0$ and $\omega^2 \to C_s/R_0^2$ which represents a wave with infinite parallel phase velocity and zero parallel group velocity. This relation holds only at q_{min}, and $k_\parallel$ will be slightly different from zero in the regions around this.

In this limit it is expected that both the ions and electrons should respond isothermally, that is, with $\gamma_e = \gamma_i = 1$. But this limit is simply not reconcilable with the analysis presented in Fig. 4-12 which shows that $\gamma = 1$ is well outside of the error bars. Rather, this analysis suggests that even as $k_\parallel \to 0$, the response of the ions and electrons is similar to that of the Alfvénic phase. Further work is needed to clarify the physics of this limit.

A thermodynamic treatment of the Alfvén waves provides another insight into the issue of the adiabatic index [73]. Classically, the adiabatic index can be interpreted as a constant of proportionality between the pressure (P) and internal energy (U) via the relation $P = (\gamma - 1)U$, an equivalent expression of $1/2kT$ per degree of freedom. While these concepts were derived for a system in equilibrium, an isentropic wave also satisfies the conditions and can be considered with the same model. The condition for an isentropic process is that the wave speed be much larger than the thermal speeds, which as noted earlier, may be true only for the ions. Nonetheless, we may proceed to derive an estimate of the adiabatic index via this method. The energy density is the sum of the field energy and kinetic energy of the wave. Ignoring the contribution from the electric field, which is smaller by a factor of $v_A^2/c^2 \ll 1$ compared to the magnetic contribution, the energy density of the wave can be expressed as,

$$U_w = \frac{1}{2\mu_0}B_1^2 + \frac{1}{2}\rho v^2,$$

where v and B_1 are the magnitudes of the perturbed quantities from the wave, v is assumed to be of first order. Note that in deriving this form, we have assumed that $\mathbf{B}_0 \cdot \mathbf{B}_1 = 0$ as per the argument in 3.1. Combining Faraday's Law (3.3), Ohm's Law (3.4), and the dispersion relation $\omega^2 = k_\parallel^2 v_A^2$ we have $\mathbf{v} = \mathbf{B}_1/\sqrt{\mu_0 \rho}$, which gives

$$U_w = \frac{1}{\mu_0} B_1^2, \tag{4.2}$$

Similarly, the pressure is accounted for by the combination of the Maxwell stress tensor and the pressure tensor for the perturbations,

$$\begin{aligned} P_w &= \frac{1}{2\mu_0} B_1^2 \underline{\mathbf{I}} - \frac{1}{\mu_0} \mathbf{B}_1 \mathbf{B}_1 + \rho \mathbf{v}\mathbf{v} && (4.3) \\ &= \frac{1}{2\mu_0} B_1^2 \underline{\mathbf{I}} && (4.4) \end{aligned}$$

where $\underline{\mathrm{I}}$ is the identity matrix and the notation **vv** signifies an outer product. The resulting pressure perturbation in Eq. 4.4 is isotropic. Apparently, the kinetic and line bending pressures cancel exactly, with the remaining pressure arising from the second order field variation, yielding $\gamma = 3/2$. The author's interpretation of this result is that the shear Alfvén wave is effectively a system with four degrees of freedom: two from the motion of the plasma and another two from the motion of the magnetic field. Shear Alfvén waves are effectively absent of motion in the parallel direction. The theoretical basis for these calculations is complicated by the presence of a small but necessary compressional component. However, as an approximation, this calculation supports the measurement of $\gamma < 5/3$.

In addition to the theoretical uncertainty in the parameter γ, there are the uncertainties in the input profiles used for the analysis. While the core q profile is unknown, the uncertainty is effectively eliminated through analysis of the frequency chirp which gives $q_{min}(t)$. The remaining sources of uncertainty are the temperature, temperature gradient, density, and density gradient, whose dependencies are summarized in Fig. 4-13. To separate the effects of temperature and temperature

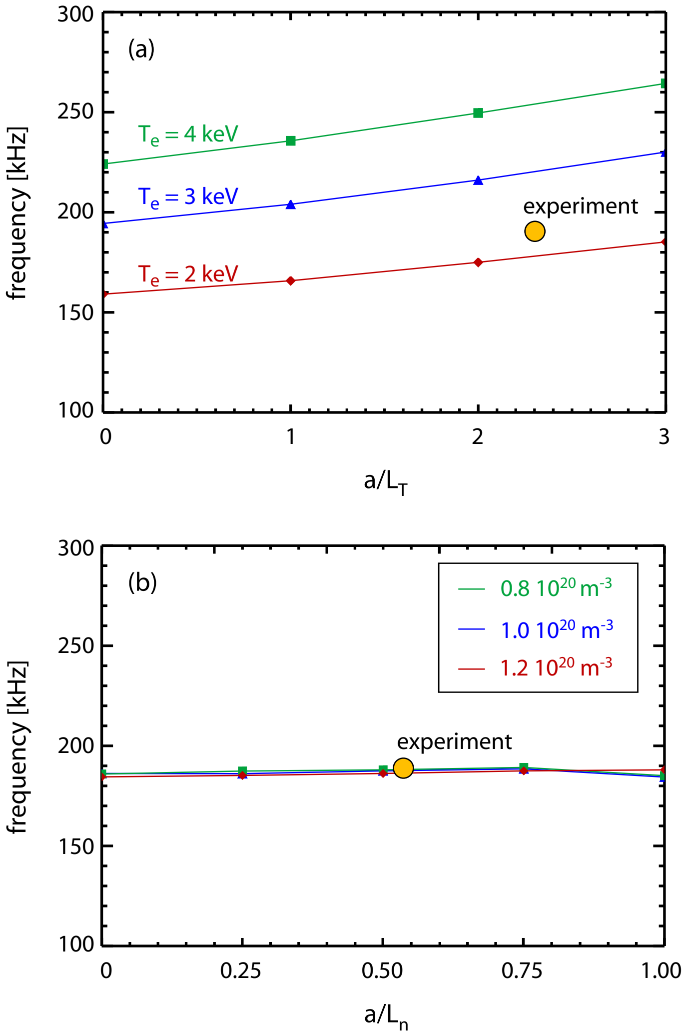

Figure 4-13: Parameter scans in NOVA show that the minimum RSAE frequency has (a) a strong temperature dependence and weaker temperature gradient dependence and (b) no significant dependence on density and density gradient. The temperature scan was conducted using the experimental density profile, and the density scan using the experimental temperature profile. The electron temperature near q_{min} is about 2.3 keV, in good agreement with an interpolation of the scaling studies in panel (a). These cases used $T_i/T_e = 0.8$ and $\gamma = 5/3$.

gradient, for example, the values of T_e and T_i were held fixed at the radial position of the maximum of the eigenmodes while the temperature gradient was varied. These scans show that f^2_{min} has a strong, linear dependence on the adiabatic index and the temperature, with a comparatively minor dependence on the temperature gradient. The minimum frequency is independent of density and density gradient. A best fit function from parameter scans in NOVA is found to be of the form,

$$f_{\mathrm{NOVA}}[\mathrm{kHz}] = 100\, T_e^{1/2} \left(0.75\, \gamma + 0.15 \frac{a}{L_T}\right)^{1/2}, \tag{4.5}$$

where T_e is given in keV, a is the plasma minor radius, and $L_T^{-1} = -(\mathrm{d}/\mathrm{d}r) \ln T_e$. The fit function is compared to a collection of minimum frequency data in Fig. 4-14. This analysis finds that the best fit to the collection is for $\gamma = 1.40$, with bounds at $\gamma = 1.25$ and $\gamma = 1.55$ from the error analysis. The point marked 1040406018 corresponds to the data presented in the previous discussion of Fig. 4-12.

An alternative method of evaluating the minimum frequency scaling can be found in analytic theory of the RSAEs employing an expansion about the point of zero shear. Analysis by Breizman *et al.* [60] examines the geodesic acoustic deformation of the Alfvén continuum as $k_\parallel \to 0$. From the eigenmode equations in Ref. [60] an approximate dispersion relation can be derived,

$$\omega^2_{RSAE} \approx \frac{2C_s^2}{R_0^2} - \frac{2}{M_i R_0^2}\, r \frac{\mathrm{d}}{\mathrm{d}r} (T_e + T_i) + \frac{v_A^2}{R_0^2} \left(\frac{m}{q_{min}(t)} - n\right) + (\Delta\omega)^2, \tag{4.6}$$

where $C_s^2 = (T_e + 7/4 T_i)/M_i$ is the sound speed (including ion FLR corrections), T_e and T_i are the electron and ion temperatures respectively, and M_i is the ion mass. The $(\Delta\omega)^2$ term includes energetic ion effects. Note that the minimum frequency is achieved when the Alfvénic term vanishes, which occurs when $q_{min} = m/n$. For the sake of the present analysis the $(\Delta\omega)^2$ term is ignored, mainly due to the difficulty

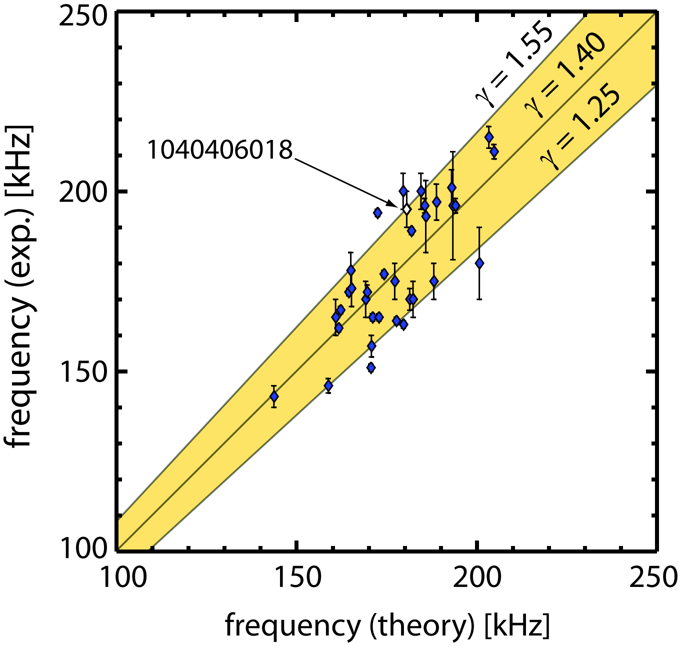

Figure 4-14: Plot of the experimental minimum frequency measured by PCI versus the form fitted to NOVA data, Eq. 4.5. The best fit between the experimental set and the fit is found for $\gamma = 1.40$, with an approximate error bound set at $\gamma = 1.25$ and $\gamma = 1.55$, based on the FWHM of the inverse of the sum of the squared residuals.

in establishing a good measure of these effects based on the available experimental data. It should be noted that Eq. 4.6 was derived under certain assumptions about the ordering of various terms, including large m and n, $2q_{min}^2 \gg 1$ and $\epsilon^2/m \ll \beta \ll \epsilon$, where ϵ is the local inverse aspect ratio (r/R_0) and can be taken to be approximately 10^{-1}. The $2q_{min}^2 \gg 1$ is not well satisfied for $q_{min} \approx 1$ and the lower inequality of the third condition may be of order $1:2$, but otherwise these approximations are reasonable for conditions of Alcator C-Mod experiments. As will be shown in the following chapter, RSAEs excited near $q_{min} = 1$ have a non-zero minimum frequency which seems to be in good agreement with this form, suggesting that the approximate dispersion relationship (Eq. 4.6) may be rather robust.

Equation 4.6 should be recast in a form appropriate for comparison with experimentally measured values. Taking the limiting case of a vanishing Alfvénic term and ignoring the energetic particle effects, Eq. 4.6 becomes

$$\omega_{RSAE}^2(q_{min} = m/n) \approx \frac{2T_e}{M_i R_0^2}\left[\left(1 + \frac{7}{4}\tau\right) + \frac{r}{L_T}(1+\tau)\right], \tag{4.7}$$

where $\tau = T_i/T_e$. Experimentally, the electron temperature profile is a well diagnosed quantity from which both the local T_e and L_T can be derived. The ion temperature profile is less well diagnosed, and for these experiments is assumed to be have the same shape as the electron temperature profile, though scaled in amplitude to match the ion temperature inferred from the neutron diagnostic. In the following analysis the radial position of the modes is approximated by $r/a = 0.3$ for all cases. Replacing the factor of $7/4$ in C_s^2 with a free parameter Γ the fit between experiment and theory can be varied. A collection of minimum frequency data from multiple experiments is compared to 4.7 and presented in Fig. 4-15. The range covered by the yellow band is indicative of the optimal fit when the theoretical values are varied by the formerly discussed uncertainty analysis. The optimal fit is very close to the theoretical value of 7/4, though the sensitivity of the fit to Γ and the significant error bars on the calculations limit the conclusiveness of this study. The largest uncertainties in the analysis of the minimum frequency come from the radial position of the mode (which affects both r and the local value of T_e), the ratio of the ion to electron temperature (τ), and the local electron temperature gradient (most significant). An uncertainty analysis for f_{min} calculated via Eq. 4.7 shows that the fractional uncertainty including all of these effects is approximately 10%. This provides an effective bound to the data, which was used to limit the range of possible Γ values. It may be that much of the residual scatter is due to the influence of the unknown energetic particle contributions, but without additional information it is impossible to account for these effects.

In summary, the minimum frequency data for RSAEs during the current ramp have been collected and compared to numerical and theoretical models. The data suggest that within the MHD framework the theoretical models can reproduce the experimental data when the thermodynamic γ is taken to be in the neighborhood of 1.4 ± 0.15. This value seems to be in agreement with a thermodynamic estimate of γ considering perturbation of both plasma and magnetic fields which calculated $\gamma = 3/2$. Corrections to this estimate based on finite compressibility and non-adiabatic response of electrons may well account for the difference. Comparison of the same data with the theoretical Eq. 4.6 suggest that the Breizman *et al.* form is close to the optimal fit to the experimental data. Neglect of the energetic ion contribution and the significant error bars on the study limit the conclusiveness of this comparison. In all of these studies, the results depend rather sensitively on the local value of the ion temperature, for which there was not a good experimental measurement at the time of these experiments. The global neutron rate, together with a measure of the density

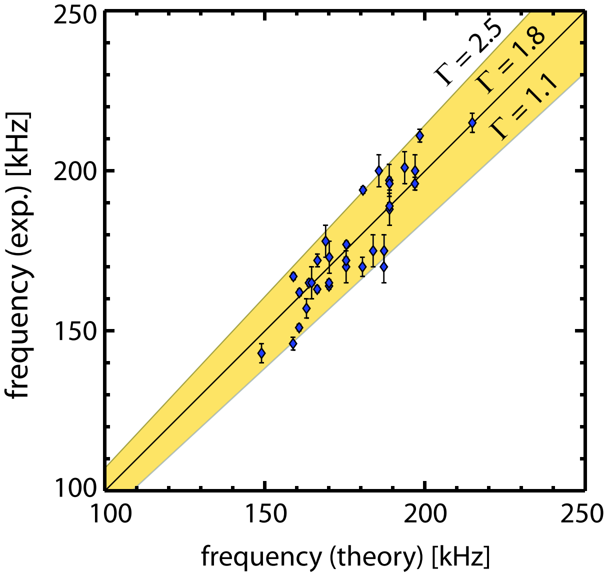

Figure 4-15: Experimental PCI data is plotted versus the theoretical minimum frequency relation from Breizman *et al.*. The vertical uncertainty arises from the finite width and extrapolation uncertainty, as shown in Fig. 4-11. The spread in the range of γ arises primarily from the uncertainty analysis of the temperature and temperature gradient effects.

profile from Thomson scattering and an assumption about the similarity of the profile shapes, provides the only estimate of the ion temperature. Future experiments would benefit from having a direct method of diagnosing the ion temperature profile to eliminate this as a source which would allow for a stronger bound on the scaling of the minimum frequency and the effective adiabatic index.

4.4 Mode Tunneling

An interesting feature of measurements of RSAEs is that the relative amplitude of the magnetics signals, referenced to the PCI signals, are generally smaller by about an order of magnitude in the RSAE phase compared to their later development in the TAE phase. The model of the RSAE residing above a local maximum in the Alfvén continuum deep in the plasma core shows that they are shielded from the edge by the presence of a large peak in the Alfvén continuum rising up to the TAE gap, as in Fig. 4-16. Consideration of this model begs the question of how the RSAEs interact with the Mirnov coils located in the limiters if they are thus shielded from the edge, especially in light of the fact that NOVA always calculates the modes to have zero amplitude at the plasma edge. Admittedly, the failure of NOVA in this regard is a result of its design, employing a fixed boundary condition when solving the differential equations. A proper solution would remove this artificial constraint and allow finite displacements at the edge which could couple to the vacuum magnetic field. The task of modeling the scrape off layer and plasma boundary is formidable, in part due to the complicated magnetic geometry of this region which often includes a magnetic X-point (null in the poloidal field). While at this time it is not possible to run NOVA with a free-boundary condition, it is nonetheless possible to examine the coupling to the Mirnov coils, at least qualitatively. The central idea of this section

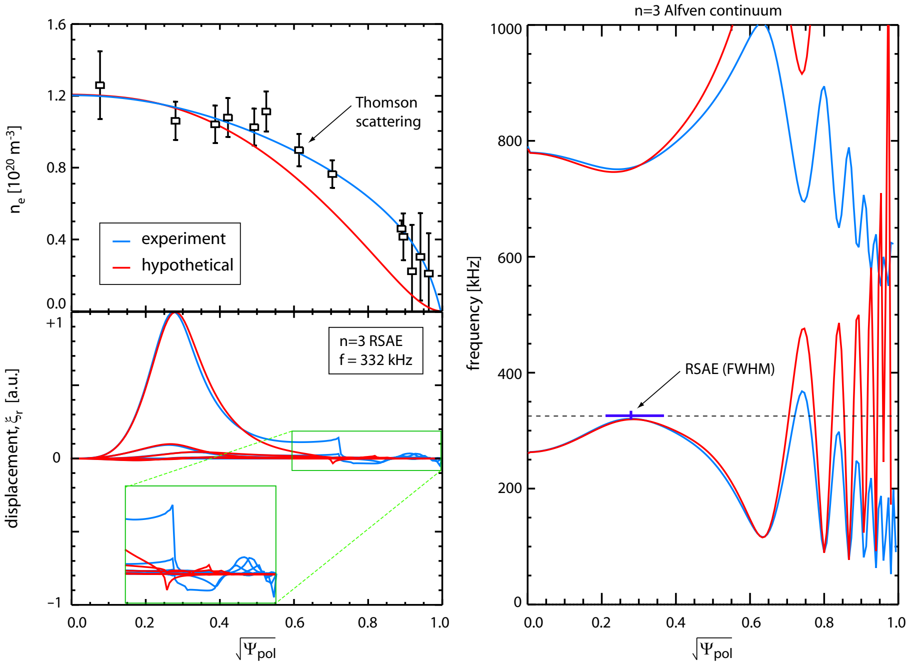

Figure 4-16: A comparison of RSAE solutions for two density profiles. The solid blue traces represent the experimental case and the red dashed traces represent a case with a reduced edge density profile. The effect of the reduction of the edge density is to increase the frequency of the Alfvén continuum, providing additional barriers through which the RSAE must tunnel to reach the edge, effectively reducing the measurable amplitude to zero. The experimental case, however, must tunnel through only a single barrier, resulting in finite amplitude at the edge.

is that even though NOVA's eigenmodes are forced to have zero amplitude at the plasma boundary, just interior to this point they may have finite amplitude. It is possible then to look for qualitative changes in the edge amplitude as the profiles are varied or evolved and compare these changes to the relative amplitudes observed in experiment.

The basic structure of the Alfvén continuum is derived from the geometric and equilibrium properties of the plasma. Except for very rare cases, the RSAE frequency equals the Alfvén continuum at some point in the plasma, as in the right panel of Fig. 4-16. For eigenmodes which are truly localized to the plasma core, this does not present a problem. However, for extending modes which have finite amplitude at the edge this implies that the eigenmode must interact with the Alfvén continuum. The only conceivable answer to the question of how the magnetics can detect the core localized RSAEs is that the modes must "tunnel" through the resonant regions defined by crossings of the Alfvén continuum, much like the tunneling of a quantum particle in a double-well potential. The representation of the RSAE eigenmode equation as a Schrödinger potential [8] (see 3) shows a slightly different picture than what is expected of quantum tunneling through classically forbidden regions. Instead of a potential barrier, the Alfvén continuum forms a strong potential well where $\omega^2 = \omega_A^2$, causing the eigenmode to develop large gradients around these points. Nonetheless, the effect is quite similar, with the existence of an eigenmode localized to the region around q_{min} depending on the relative strengths of the potential wells at q_{min} and at the points of continuum crossing.

What is important for the question at hand, that of edge detection, is the number of continuum crossings. The Alfvén continuum is a function of $\omega_A^2 = k_\parallel^2 v_A^2$, appropriately modified by coupling of poloidal harmonics, and has within it a profile dependence of the form $(m/q - n)^2/n_e$, the $(m/q - n)$ factor from $k_\parallel^2$ and the $1/n_e$ term from v_A^2. The density of peaks in the Alfvén continuum is sparse near the core (which allows the modes to form here) and is largest toward the edge on account of the rapid variation of q in this region. It follows then, that modest changes to the edge Alfvén continuum may result in large changes to the structure of the edge eigenmode, and that correspondingly, a large change should be observed on the magnetic pick-up coils. This effect is illustrated in Fig. 4-16. This case compares two density profiles, one approximating the experimental values and the other with reduced density near the edge. In both cases, the RSAE must tunnel through the first peak near $\sqrt{\psi_{pol}} = 0.7$. In the case of the experimental profiles the mode encounters only the two singularities associated with this peak and develops finite edge amplitude. The hypothetical density profile, however, shows that the reduced density translates to an increase in the Alfvén continuum which forces the mode amplitude to vanish near the edge. If such a decrease in density could be realized in experiment, this model predicts that the magnetics signal should progressively diminish, and perhaps at some point vanish altogether as a series of Alfvén continuum barriers effectively trap the mode in the core. While it may not be feasible to vary the density profile to this extent in experiment, an alternative method for modifying the Alfvén continuum based on modifying the plasma current may be possible. This effect is illustrated in Fig. 4-17.

Outside of varying the density or q profile (which has not been performed experimentally at this time), evidence in support of the tunneling effect can be found in variations of magnetics and PCI signals as the RSAEs evolve. A comparison of PCI and magnetics spectrograms, see Fig. 4-3, shows striking differences in the observed amplitudes of the RSAEs. Specifically, PCI often measures the RSAEs with great clarity and with an amplitude peaking at or before f_{max}. The Mirnov coils on the other hand, register much weaker signals from the RSAEs during the Alfvénic phase and often exhibit a peak amplitude as the mode evolves into a TAE. A relative increase in the amplitude of the magnetics signal compared to the PCI signal can be interpreted as a result of a change in tunneling efficiency as the eigenmode rises above successive barriers in the Alfvén continuum, reaching a maximum as the RSAE enters the TAE gap where it is free of all barriers. Because of the difficulty of directly comparing the PCI measurements to the magnetics measurements, the problem of tunneling is best cast as a question of tunneling efficiency, that is, the

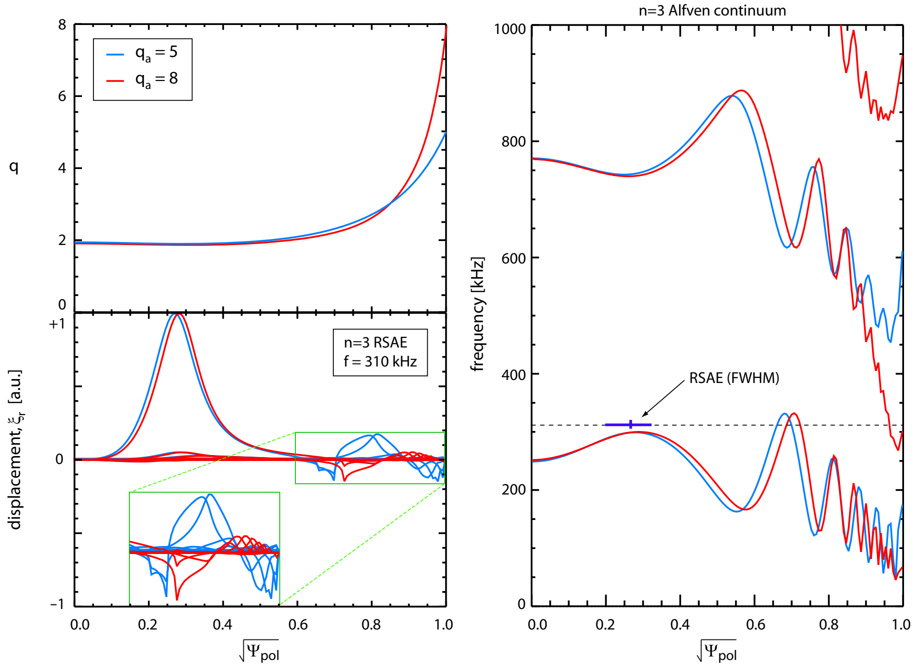

[H]

Figure 4-17: A comparison of RSAE solutions for two q profiles. Increasing the edge q profile, equivalent to a decrease in plasma current, results in an additional Alfvén continuum crossing. This modeling suggests that a sharp transition in the magnetic signal should be observed as the current is decreased.

normalized penetration of the mode from the core to the edge. Approximating the first order perturbation of the poloidal field as $B_{\theta 1} \sim B_\theta \xi_r / r$ shows that an estimate of the edge magnetic perturbation may be derived from the amplitude of the fluid displacement which is provided by the eigenmode structures like those presented in Figs. 4-16 and 4-17. With the assumption that the magnetic perturbations at the Mirnov coils are strongly correlated with the amplitude of the magnetic perturbations just interior to the plasma edge, NOVA calculations of the fluid displacement provide a means of comparing the synthetic PCI and magnetics signals.

While the RSAEs during the grand cascade structure (starting around 135 ms in Fig. 4-3) are clear and distinct in the PCI data, analysis of the tunneling effect with these modes is problematic on account of the interactions between the modes. In particular, the amplitude of the n^{th} RSAE will decrease dramatically as the $(n+1)^{th}$ RSAE transitions to a TAE, presumably because of an enhanced access to the free energy of the energetic ions by the TAEs. These features are presented in section 7.1 as an interesting further problem regarding the transport of the energetic ions. However, the RSAEs occurring at the earlier times (100 – 130 ms) do not overlap and thus their amplitude can be more directly interpreted as arising from a steady energetic ion distribution, shown in Fig. 4-18 for reference. Mode amplitude histories for the identified $n = 3, 4$ RSAEs observed between 100 ms and 130 ms are presented in Fig. 4-19. The data for each diagnostic are scaled relative to the maximum signal detected. The following discussion seeks to expose the gross trends of the ratios of the PCI to magnetics measurements.

The spatial structures calculated by NOVA for the $n = 3$ and $n = 4$ eigenmodes agree well with the spatial structures measured by PCI, supporting the use of these solutions in this analysis (see for example Fig. 4-7). It is evident from the traces in Fig. 4-19 that the magnetic signature of the $n = 4$ mode is delayed well into the evolution, becoming strong only as $f \to f_{max}$. The $n = 3$ RSAE on the other hand shows a larger magnetics signal earlier in the evolution. The ratio of the edge signal to the line integral of the density fluctuations in the NOVA solutions provides a measure of the theoretical tunneling efficiency. These calculations are compared to the experimental data in Fig. 4-20, where the ratios show more clearly the trend of greater tunneling efficiency for the $n = 3$ RSAE as compared to the $n = 4$ RSAE. The theoretical tunneling efficiency reproduces the gross features of the experimental tunneling factors, namely that the $n = 3$ RSAE has the larger tunneling efficiency

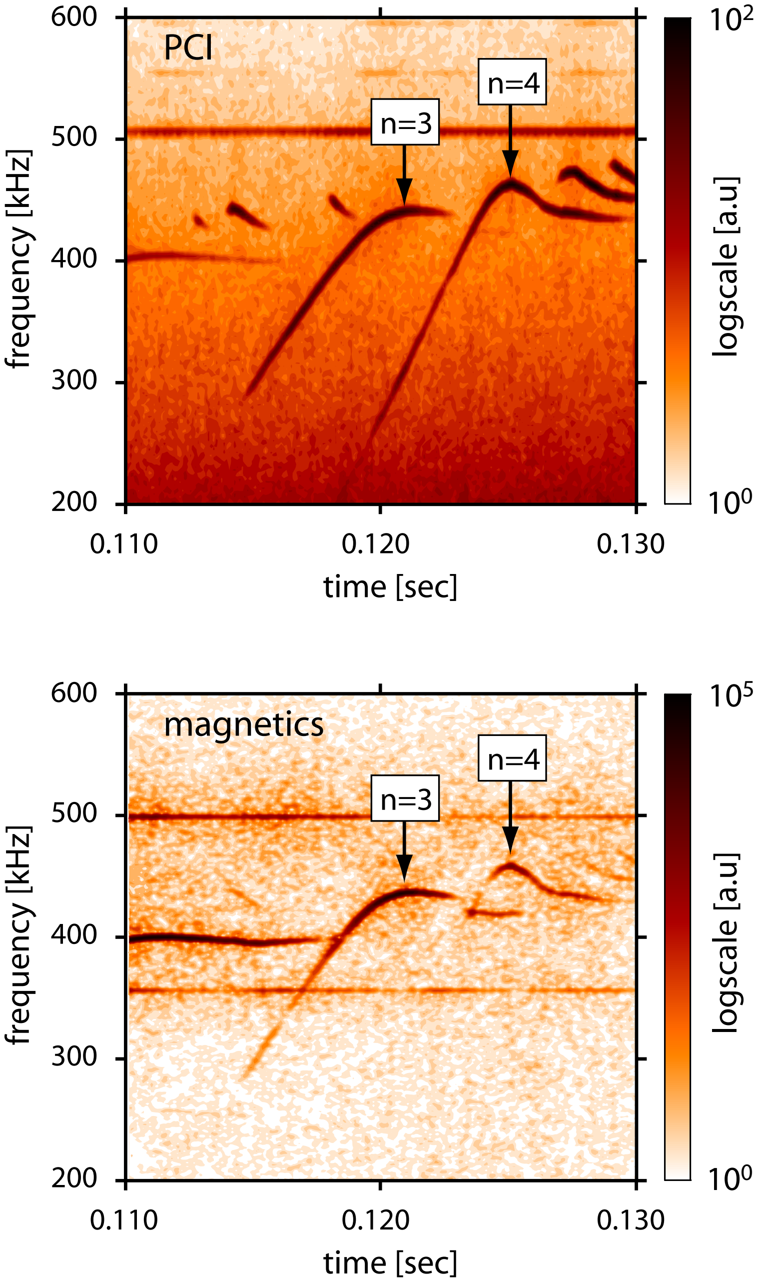

Figure 4-18: PCI and magnetics spectrograms of the RSAEs showing the modes used for analysis of the Alfvén continuum tunneling effect.

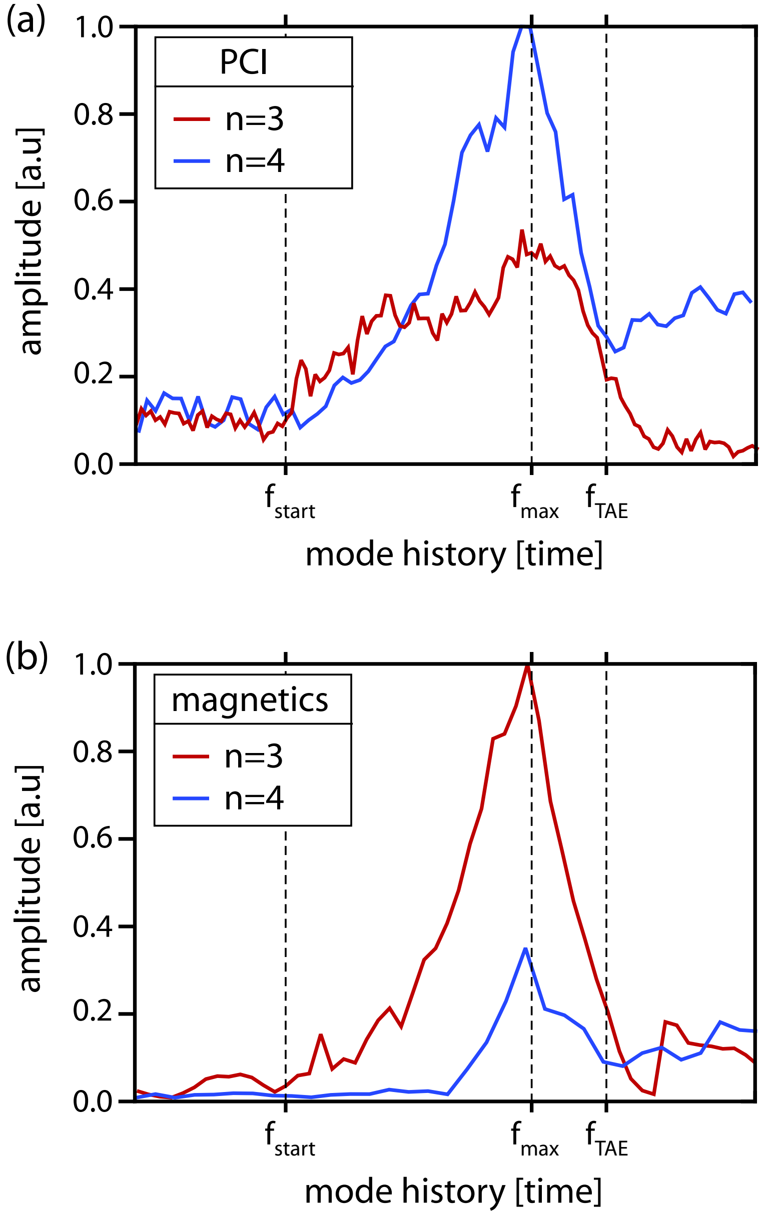

Figure 4-19: Amplitude history for the n = 3 and n = 4 RSAEs as measured by (a) PCI and (b) magnetics. These data indicate that for a given level of excitation measured by PCI, the $n = 3$ RSAE couples to the edge much more effectively.

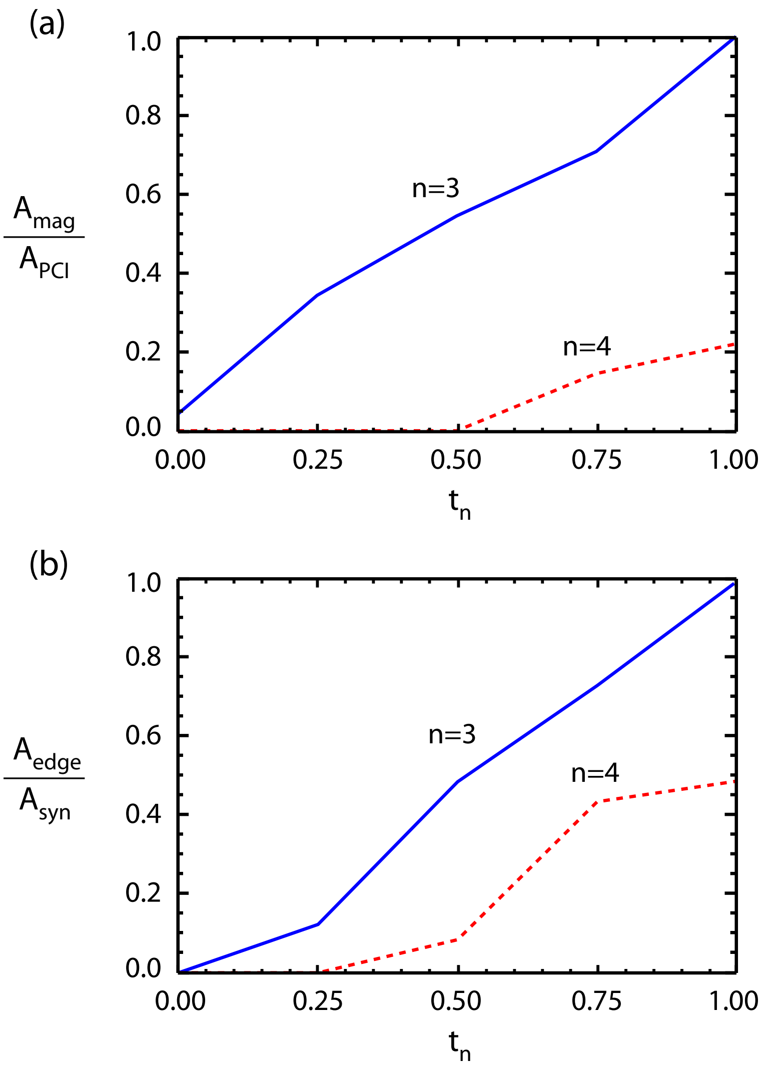

Figure 4-20: Tunneling efficiency factors calculated for the $n = 3$ and $n = 4$ RSAEs as a function of normalized mode time, $t_n = (t - t_{min})/(t_{max} - t_{min})$ for (a) the experimental data derived from the ratio of the magnetics signal to the PCI signal and (b) calculations from NOVA comparing the edge amplitude to the synthetic PCI signal.

and the $n = 4$ curves increase more slowly as a function of normalized time. While acknowledging that modeling of the edge plasma is difficult on many accounts, these comparisons strongly suggest that at least qualitatively the models in NOVA account for the tunneling effect and motivate further studies along these lines.

4.5 Second Order RSAE Perturbations

The RSAEs excited during that current ramp are often accompanied by harmonics at twice the frequency of the fundamental, as shown in Fig. 4-21 below. Motivated by these observations, a theoretical model of RSAE harmonics was published in 2006 [74], though at that time the more general features of mode coupling were not appreciated. An interesting result of this theoretical treatment is that it may be possible to derive a measure of the local magnetic perturbation from the ratio of the second order perturbation to the first order perturbation. This in turn would allow further testing of the mode tunneling effect by comparing the core magnetic perturbation to the edge magnetic perturbation through the eigenmode structure calculated by NOVA. Such work is envisioned as a future extension of the analysis presented here.

Note that there are numerous examples of modes in the harmonic range of frequencies with no companion in fundamental frequency range. Harmonics at $2\omega_n$ with mode numbers of $(2m, 2n)$ are anticipated from an analysis of second order perturbations, a result of nonlinear products in the MHD equations such as $\tilde{\mathbf{j}}_n \times \tilde{\mathbf{B}}_n$, where $\tilde{\mathbf{j}}_n$ represents the perturbation to the current density with toroidal mode number n. More generally, nonlinear mixing between modes with different toroidal mode numbers, arising from terms like $\tilde{\mathbf{j}}_{n+1} \times \tilde{\mathbf{B}}_n$ and its conjugate, will result in wider range of second order modes in the harmonic range of frequencies. Similar to the harmonics,

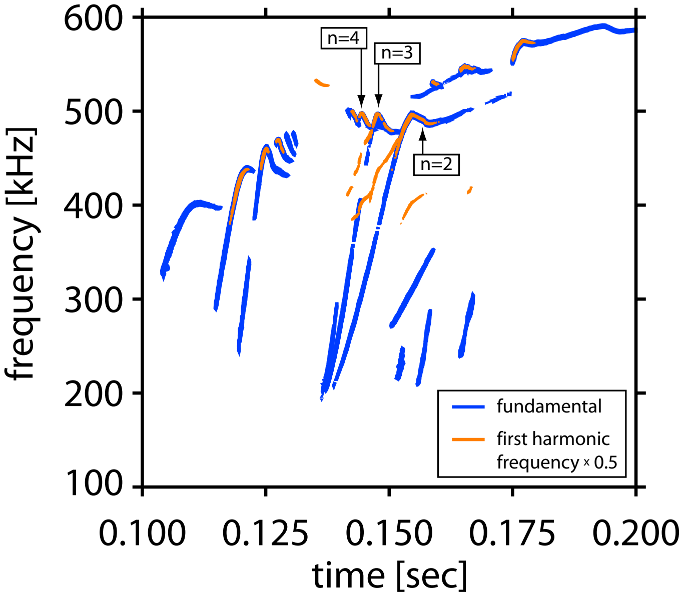

Figure 4-21: A filtered PCI spectrogram showing only the unstable RSAEs and TAEs. The fundamental modes are shown in blue and the first harmonic measurements overlaid in orange after dividing their frequency by 2.

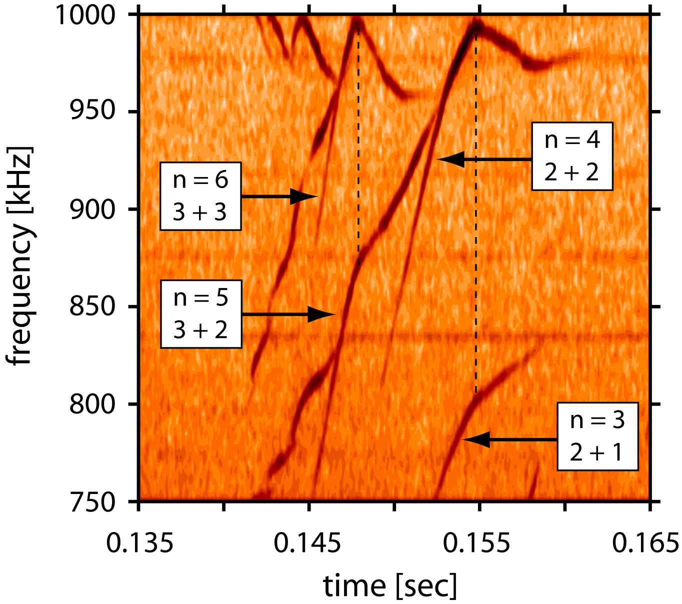

Figure 4-22: Composite PCI spectrogram focusing on the RSAE harmonics.

general second order modes have a frequency and wavenumber which are the sum of the coupled first order RSAEs. The modes in Fig. 4-21 at frequencies other than a harmonic are a result of coupling between RSAEs of mode numbers $n = 1$ and $n = 2$, and $n = 2$ and $n = 3$, and so on.

Figure 4-22 presents a PCI spectrogram highlighting the modes in the harmonic range of frequencies. The $n = 5$ mode is a result of coupling between the $n = 2$ and $n = 3$ fundamental RSAEs. The bend in the frequency of the $n = 5$ mode results when the $n = 3$ RSAE transitions from the RSAE to TAE phase, highlighted by the dashed line. Perhaps most interesting is the observation that the $n = 3$ and $n = 5$ modes are excited more strongly than the $n = 4$ and $n = 6$ modes (in the harmonic range of frequencies), suggesting that the coupling between unlike RSAEs is stronger than the self-coupling. Further theoretical work is needed to address these issues.

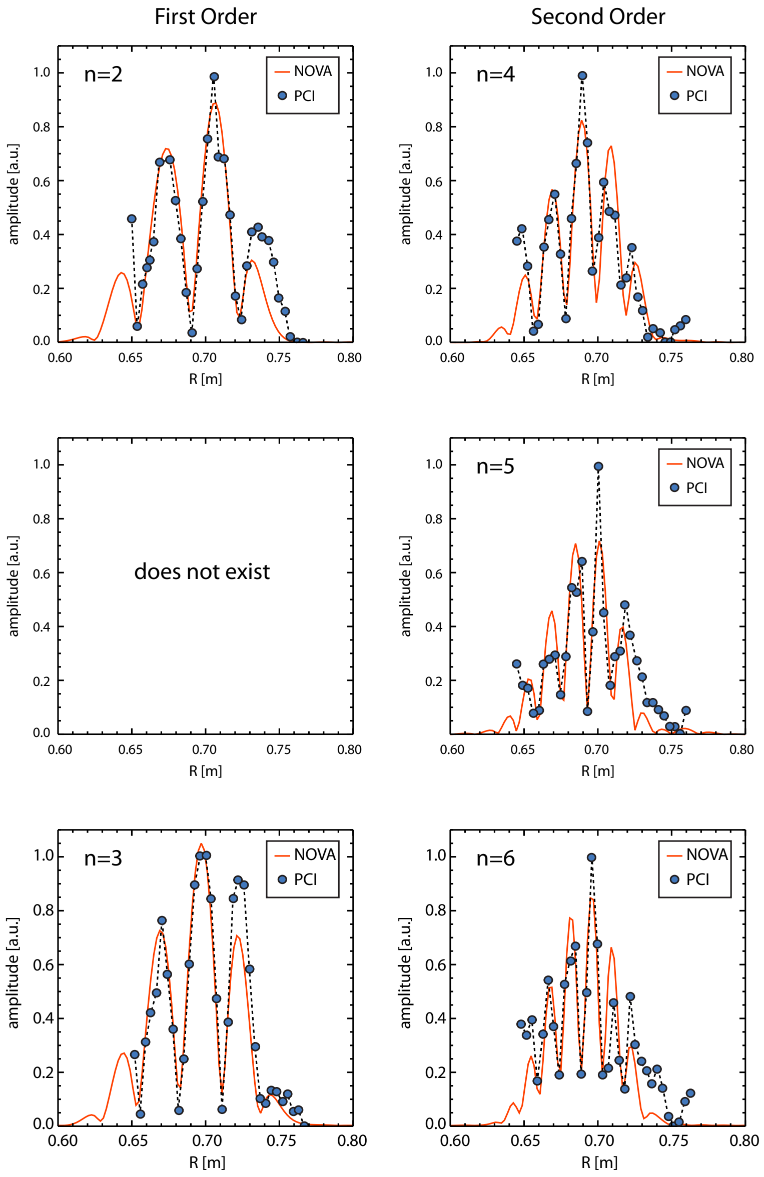

Figure 4-23: Comparison of synthetic and experimental PCI structures for the first order RSAEs (left column) and the second order RSAEs (right column). The second order $n = 4$ and $n = 6$ RSAEs are harmonics of the $n = 2$ and $n = 3$ first order RSAEs, respectively. There is no equivalent to the $n = 5$ RSAE in the fundamental frequency range. The difference in spatial structure of the harmonics and fundamental modes provides confirmation that these signals are not the result of a diagnostic non-linearity.

To conclude these studies we look at the spatial structure of the second order RSAEs. While NOVA calculates eigenmodes for the first order expansion of the MHD equations, it is simply incapable of providing solutions for the second order perturbations. However, the RSAEs can be approximated by a spatial structure described by a single toroidal mode number, and a single dominant poloidal mode number. In this regard, NOVA can be used to model the spatial structure of the second order modes by using the first order solutions, even if the frequency is incorrect. Figure. 4-23 shows the comparison between the synthetic PCI and the experimental measurements of the spatial structure of the $n = 4, 5, 6$ second order modes identified in Fig. 4-22. These comparisons confirm that the wave numbers add as expected to produce the second order structure.

Chapter 5

Reversed shear Alfvén eigenmodes during sawteeth

Following the diffusion of current during the ramp-up phase, the experiments often enter what is known as the ”flattop phase”, wherein the plasma current is maintained at a near constant value by the continual application of the toroidal electric field to balance resistive losses, usually with a loop voltage of about 1 Volt in Alcator C-Mod. One of the striking features of the flattop phase is that under almost all operating conditions there exists a periodic oscillation of the core profiles, predominantly in the electron temperature, characterized by a sawtooth-like waveform [16], known as the sawtooth oscillation, and the abrupt transition which characterizes this oscillation is known as the sawtooth crash.

The sawtooth cycle can be considered as composed of two essentially independent parts, separated by time scale: a heating and relaxation phase of order 10 msec wherein the temperature and current profiles peak on axis and the cental electron temperature increases nearly linearly with time or reaches steady-state in longer cycles, and the crash phase wherein the core temperature may drop by as much as 50% over a fraction of a millisecond. The sawtooth crash results from a magnetic reconnection process which effectively short circuits the flux surfaces and allows rapid energy and particle equilibration between surfaces inside and outside of the $q = 1$ surface [16, 75, 76, 77]. The origin, timescales, and regulating mechanisms of the reconnection event remain an active area of investigation, challenging both experiment and theory. The heating phase on the other hand, is considerably more accessible to study in large part because it is governed by steady diffusive processes and occurs over a much longer period. The focus of this chapter is the analysis of RSAEs during heating phase of the sawtooth cycle, and their application to the study of the sawtooth crash through the provision of constraints on the physics of the reconnection and transport near the magnetic axis.

All tokamak experiments have observed that during the sawtooth crash the central q profile increases, at least interior to the $q = 1$ surface. With respect to the particular value of the post crash q_0, that is q at the magnetic axis, there are numerous measurements of q_0 close to unity from JET [78], JT-60 [10], DIII-D [79, 80] and Alcator C-Mod [19], among others. On the other hand, there exist highly regarded and frequently cited measurements showing that q_0 remains significantly less than unity throughout the sawtooth cycle in TFTR [81, 82] and TEXTOR [83]. One discriminating factor between the far from unity and close to unity observations cited here is the plasma shape. The former group represents the more recent tokamaks which tend to have strongly shaped plasmas and operate with a magnetic X-point and divertor. The far from unity cases (Refs. [81, 82, 83]) are distinguished by circular, wall-limited plasmas. It is not entirely clear at this time how shaping affects the sawtooth crash, particularly in light of the fact that the reconnection during a sawtooth crash is rather well confined to the plasma core. A more recent study of the effects of shaping on sawteeth in DIII-D plasmas has found that reversed shear q profiles are likely generated in strongly shaped plasmas [79]. Alcator C-Mod experiments typically use moderate shaping parameters of $\kappa \sim 1.5$ (elongation) and $\delta \sim 0.4$ (triangularity).

A range of Alfvénic activity often accompanies sawteeth and has proven useful for MHD spectroscopy, e.g. Refs. [10, 19]. Though they were not recognized as such at the time, RSAEs during sawteeth were first observed in JT-60 [10]. Alcator C-Mod experiments in 2003 (in particular, shots 1031124027 and 1031217012) detected RSAEs with PCI, which were appreciated as such only much later. In hindsight, it is not wholly surprising that RSAEs should exist during sawteeth. The philosophical obstacle to the identification of RSAEs near $q = 1$ perhaps resulted from incorrect interpretations of equilibrium reconstructions from codes like EFIT [84] which show monotonic q profiles during sawteeth, as well as the precedent for $q < 1$ established by the frequently cited Refs. [81, 82, 83]. The EFIT program used as Alcator C-Mod calculates the q profiles based on a least squares fit to a given monotonic form and thus is simply incapable of producing a model of the accuracy and subtlety required for RSAE studies. Recent publications investigating a range of Alfvén eigenmodes during sawteeth in JET concluded in one case that the modes were $q = 1$ RSAEs [85], and in another case that the chirping modes were not RSAEs, in part due to an apparent inconsistency derived from NOVA modeling based of observed TAEs (Tornado modes) [86], though the work was hardly conclusive in this regard. Furthermore, Ref. [86] did not consider the possibility of a transient period of reversed shear following the sawtooth crash. Further measurements from Alcator C-Mod during 2007 provided definitive magnetic measurements of the toroidal mode numbers, which together with the internal fluctuation profile measured by PCI and interpreted with NOVA, firmly established these modes as RSAEs [18, 19].

The magnetic reconnection occurring during the sawtooth crash strongly modifies the poloidal field while the toroidal field is altered to a much lesser degree. The increase in q during the crash is primarily due to a decrease in B_{pol}, which results from a displacement of current away from the magnetic axis. The reheat phase following the crash sees the displaced current diffuse toward the magnetic axis, resulting in a decrease in q. The observation of RSAEs during the reheat phase naturally leads to the line of questions regarding the conditions under which the relaxation of the current following the sawtooth crash will express a reversed shear q profile. The analysis reported in Refs. [18, 19], based on modeling with NOVA, determined that the magnitude of the reversed magnetic shear interior to r_{min}(where r_{min} is the radial position of q_{min}) is very small, with $q_0 - q_{min} \lesssim 0.02$. However, attempts to model the current diffusion concluded that a strongly peaked impurity profile near the magnetic axis was necessary [18]. These issues will be further explored in chapter 6.

The following sections explore the studies of RSAEs during sawteeth, starting with an introduction to the experiments. The second section presents the $q = 1$ RSAEs and a few important observations. The last section presents a simple model of the reconnection consistent with the RSAE observations.

5.1 Overview of experimental conditions

The operating parameters for Alcator C-Mod experiments in which the $q = 1$ RSAE are observed are quite similar to those used for the current ramp studies. The data presented in Fig. 5-1 for shot 1070823019, an exceptional example of $q = 1$ RSAEs, use an early ICRH injection time of approximately 100 ms, and was an experiment optimized to study RSAEs during the current ramp. By extending the ICRH pulse through the flattop a series of RSAEs were observed during the sawtoothing period.

It should be noted that approximately 300 kW of LH power at 90° phasing was injected during a portion of this shot. Comparison of this shot to others similar except for variations in the injected LH power show little change in the behavior of the RSAEs, leading to the conclusion that 300 kW of LH power is insufficient to have a significant impact on the current profile.

The changes in the slope of the average electron density in Fig. 5-1b, between approximately 0.25 seconds and 0.40 seconds, mark transitions between L-mode (low confinement mode) and ELM-free H-mode (edge-localized mode free, high confinement mode). The transitions to the ELM-free H-mode are coincident with an unprogrammed decrease of injected ICRH power of approximately 10%. The change in the density associated with with these transitions slightly precedes the decrease of the ICRH power, suggesting that the ICRH system is responding to a change in coupling efficiency imposed by the H-mode profiles. The ELM-free H-mode is characterized by a quiescent edge D_α (deuterium Lymann α) signal which arises when edge temperature perturbations are suppressed. This reduction in edge turbulence leads to reduced edge transport, though this also applies to the impurities and ultimately leads to large radiated power and radiative collapse wherein the plasma transitions back to L-mode [87].

The $q = 1$ RSAEs have been observed in numerous experiments of varied conditions, though generally during operation at lower densities (for Alcator C-Mod) with moderate ICRH power (P_{ICRH}). Figure 5-2 presents a set of these experiments in the n_e and P_{ICRH} parameter space. These data reveal an apparent operational boundary for the excitation of RSAEs. The P_{ICRH} dependence may also be recast as a temperature constraint, which shows that peak temperatures in the $4-6$ keV range are necessary to see strong excitation of the RSAEs. It is unclear at this time if the preferential excitation of RSAEs in this lower density operational regime results from

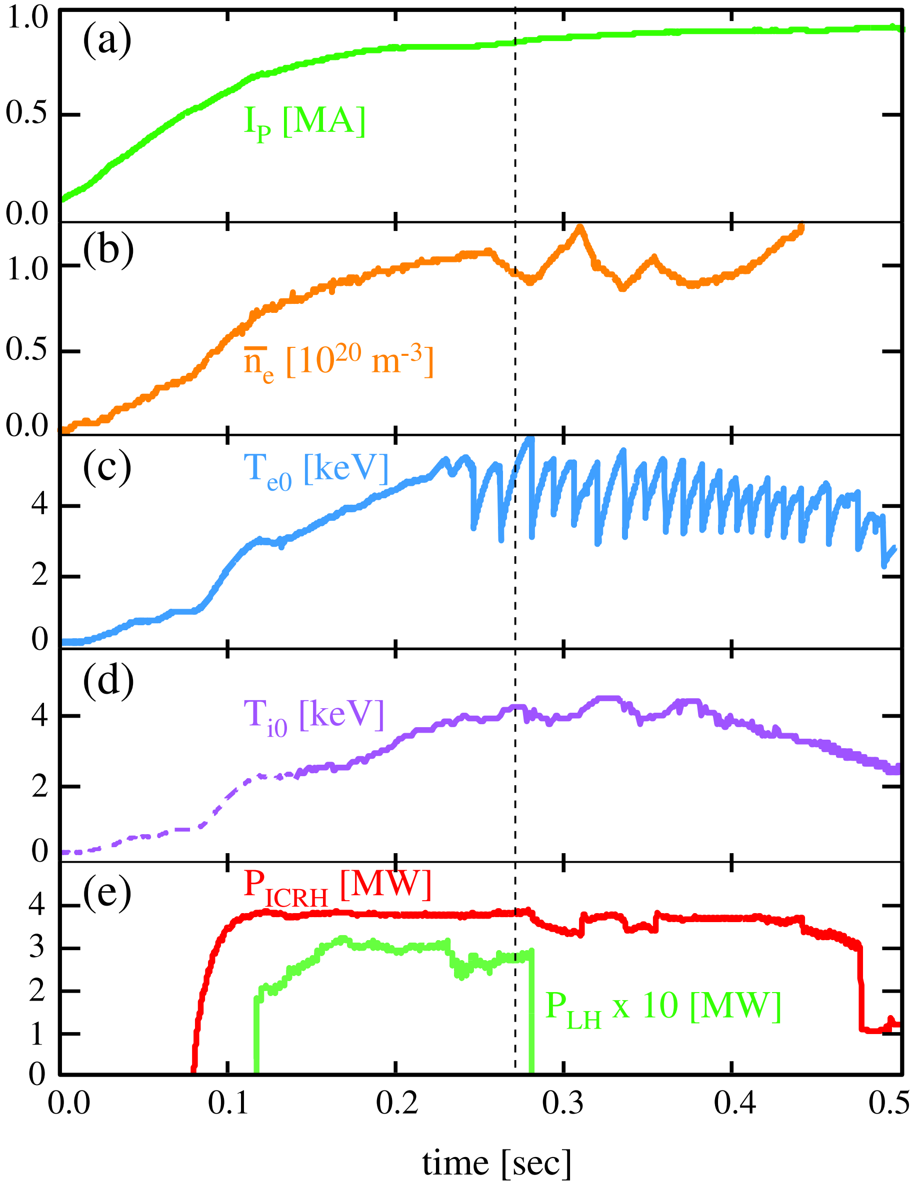

Figure 5-1: Representative plasma parameters during the current ramp ($t < 0.25$ sec) and subsequent flattop phase for shot 1070823019 for (a) plasma current, (b) average electron density, (c) electron temperature from the ECE diagnostic, (d) ion temperature from neutrons and (e) injected ICRH and LH power. The dashed line in the ion temperature trace identifies the region for which there was no neutron data, and the trace is scaled to be equal to $0.8\,T_e$. The vertical dashed line at about 0.27 seconds identifies the start of the first set of RSAEs.

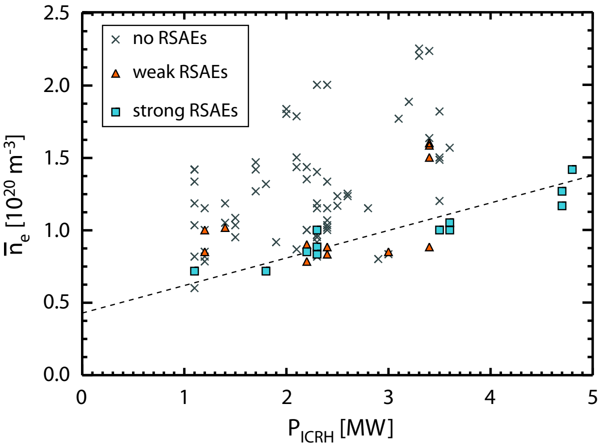

Figure 5-2: Parameter space plot of line averaged density ($\bar{n}_e$) and ICRH power (P_{ICRH}) for the excitation of $q = 1$ RSAEs, collected for 91 L-mode shots from 2007. The data indicate that the RSAEs are primarily excited in low-density with moderate to high ICRH power, for Alcator C-Mod. The null data indicate that the RSAEs are a rather general feature of operation in these conditions.

a sufficiently large energetic ion population at lower density (recall that T_H decreases approximately linearly with n_e, see Fig. 2-2) or if some aspect of the sawteeth allows a reversed shear q profile to form more readily in lower density. Measurements of the energetic ion distribution at intervals less than a sawtooth period may help to resolve this uncertainty by identifying systematic changes correlated with the RSAE activity.

5.2 Observations and modeling

Though observed in many shots, the $q = 1$ RSAEs presented here focuses on two exceptional shots which highlight some of the fundamental features of this work, 1070823019 and 1060525010. The latter shot will be discussed later with regard to the observation of down-chirping RSAEs observed in many sawteeth. The first

(1070823019) is presented in Fig. 5-3 as a composite PCI spectrogram covering the end of the current ramp and the beginning of the flattop phase. Following 0.5 sec, higher density is established and the RSAEs are no longer observed.

The set of $q = 1$ RSAEs excited immediately prior to the third sawtooth crash in Fig. 5-3 is rather unique among the collection of observations in that the amplitudes were large enough to register on the Mirnov coils. The combined PCI and magnetics data are presented in Fig. 5-4, which presents the mode numbers derived independently by PCI and the Mirnov coils. The mode numbers determined by PCI are determined by a fit to the RSAE dispersion relationship for small $k_\parallel$ which can be cast in the form $f_{min}^2 = f_0^2 + f_A^2\, n^2(\delta q)^2$ (see Eq. 3.51) where $\delta q = m/n - q_{min}$. The toroidal phase measurements from the Mirnov coils located at five different toroidal locations measure the wave propagation to be in the ion-diamagnetic drift direction, as expected for RSAEs, and confirm the PCI results. The experimental identification of the mode numbers in concert with the modeling results from NOVA presented in the following unambiguously identify these modes as $q = 1$ RSAEs. For the remainder of the analysis we focus on the PCI data.

In exactly the same manner as presented in chapter 4 for the RSAEs during the current ramp phase, modeling of the $q = 1$ RSAEs allows $q_{min}(\mathrm{t})$ to be inferred to high accuracy. More complete descriptions of the MHD spectroscopic analysis is presented in Refs. [18, 19] by the author and collaborators and is summarized here. One of the main results is the NOVA modeling of the frequencies of the large amplitude RSAEs, showing that q_{min} decreases to approximately 0.92 prior to the third sawtooth crash. These results are presented in Fig. 5-5. Similar modeling performed for other cases shows that q_{min} often decreases to approximately 0.95, and that the value of 0.92 determined here is somewhat of a lower limit for sawteeth in Alcator C-Mod under these operating conditions.

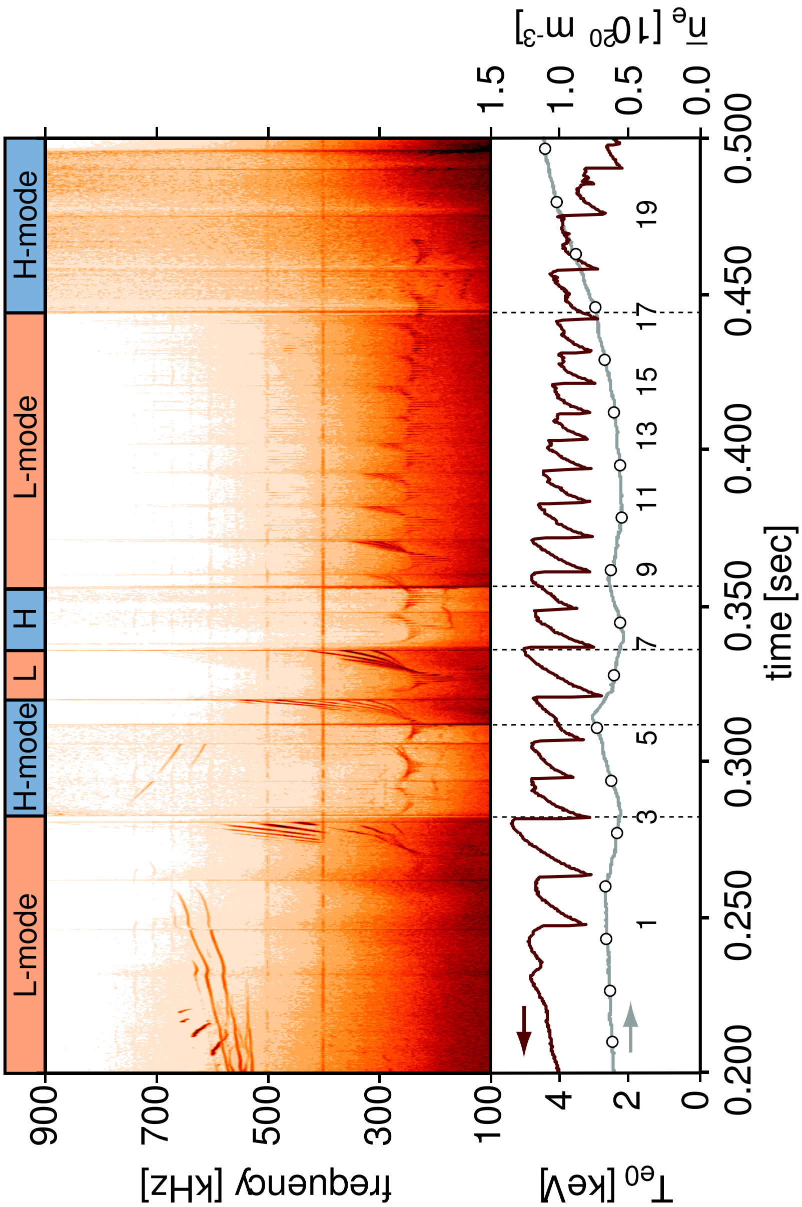

Figure 5-3: The RSAEs are the frequency-chirping traces between 200 kHz and 500 kHz. They are excited to largest amplitude during the L-mode phases, but only weakly excited during the H-mode (ELM-free) phases. Both up-chirping and down-chirping RSAEs are present in many of the sawtooth cycles, indicating that $q_{min} = 1$ enters approximately halfway through the sawtooth cycle. The numbers below the T_e data indicate the sawtooth crash number. The circles on the n_e trace identify time points where density profiles are available from the Thomson scattering system.

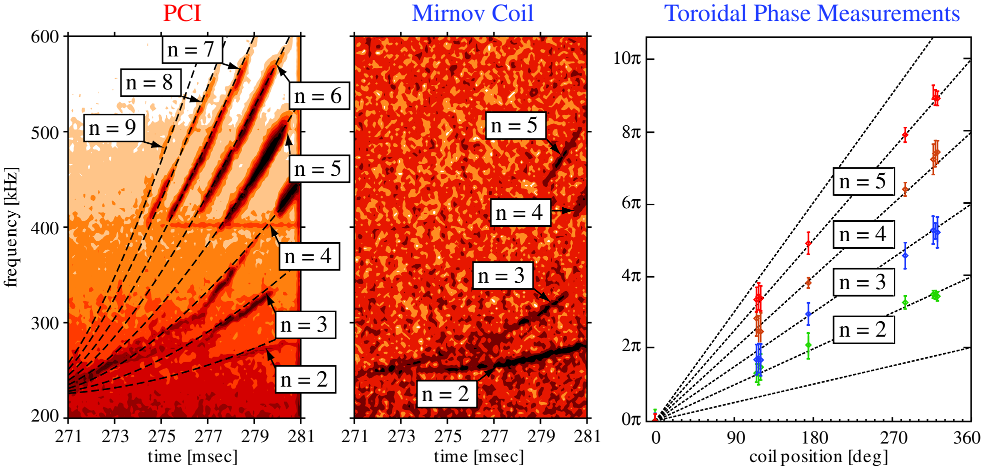

Figure 5-4: PCI and Mirnov coil spectrograms of the RSAEs observed prior to the third sawtooth crash. The spectra measured by PCI are fit with a theoretical form to infer a set of mode numbers. These inferences are corroborated by direct mode number identification from the toroidal phase measurements from the array of Mirnov coils. Reproduced from Ref. [18].

Figure 5-6 presents a complementary example of a set of down-chirping modes excited immediately following a sawtooth crash. Similar to the up-chirping RSAEs observed regularly, the down-chirping branch have a common minimum frequency. Unlike the up-chirping RSAEs however, these down-chirping modes are not, to our knowledge, associated with a minimum in q, but rather a local maximum in q as determined by modeling with NOVA.

Figure 5-7 presents two RSAE solutions from NOVA, the first pertaining to the typical up-chirping case (a-c) and the second pertaining to a down-chirping case (d-f) [18]. Importantly, no down-chirping RSAEs are found for the case of a q profile with $q > 1$ and a minimum. As noted in chapters 1 and 3, a local maximum in the Alfvén continuum is needed for eigenmode formation, as in Fig. 5-7(d) for the up-chirping RSAEs. Rather, a case with a minimum and $q > 1$ produces an Alfvén continuum

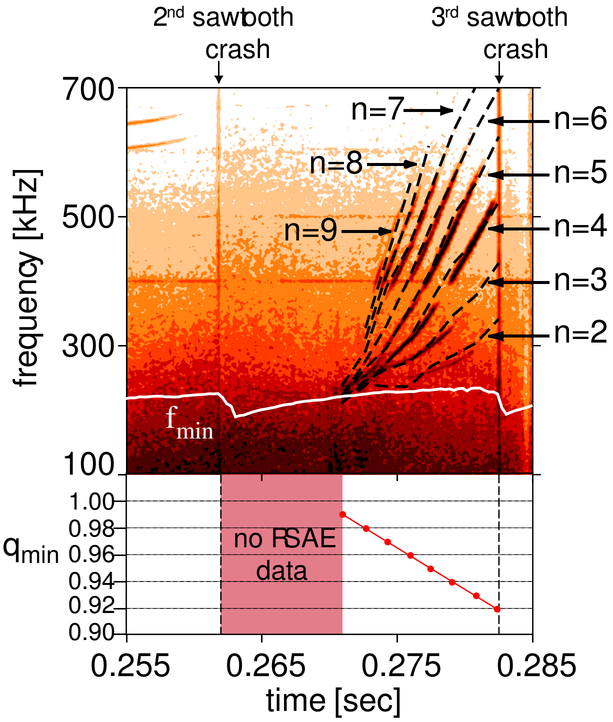

Figure 5-5: PCI spectrogram showing the RSAEs prior to the third sawtooth crash. The dashed overlay is the modeling results from NOVA which determine the evolution of q_{min}, shown below. The line f_{min} is based on the theoretical geodesic deformation of the Alfvén continuum, a function of the electron temperature [60]. Reproduced from Ref. [19].

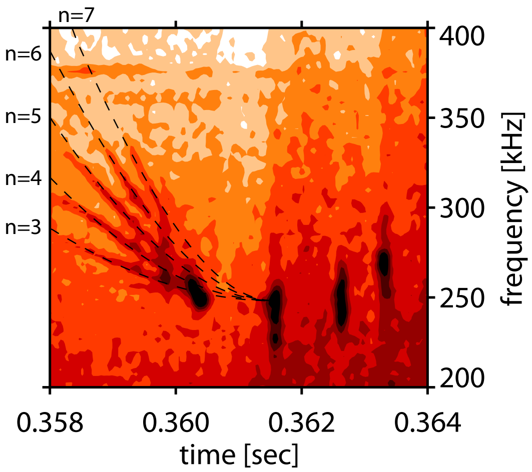

Figure 5-6: PCI spectrogram showing down-chirping RSAEs following a large sawtooth crash in shot 1060525010, the clearest example of all known cases in Alcator C-Mod. The value of q following the crash is determined to be about 1.03 based on a fit to the theoretical dispersion relationship (dashed lines). Reproduced from Ref. [18].

with a local *minimum* which does not allow RSAEs to form, except in the case of sufficiently steep pressure gradient [61]. Based on the available experimental data, the only viable solutions for down-chirping RSAEs occur with a q profile with a local maximum. These results will be revisited in section 5.3 as constraints on the sawtooth crash.

The remainder of this section focuses on three prominent observations from Fig. 5-3. First, the absence of RSAEs during the first two sawtooth cycles begs the question of what particular conditions were suddenly satisfied in the third cycle. Referencing the experimental traces in Fig. 5-1, one can observe a significant decrease in the density beginning at approximately the end of the second sawtooth crash, just prior to the start of the RSAEs. This effect is due to the formation of a magnetic X-point as the plasma moves from a wall-limited to diverted configuration. The outer

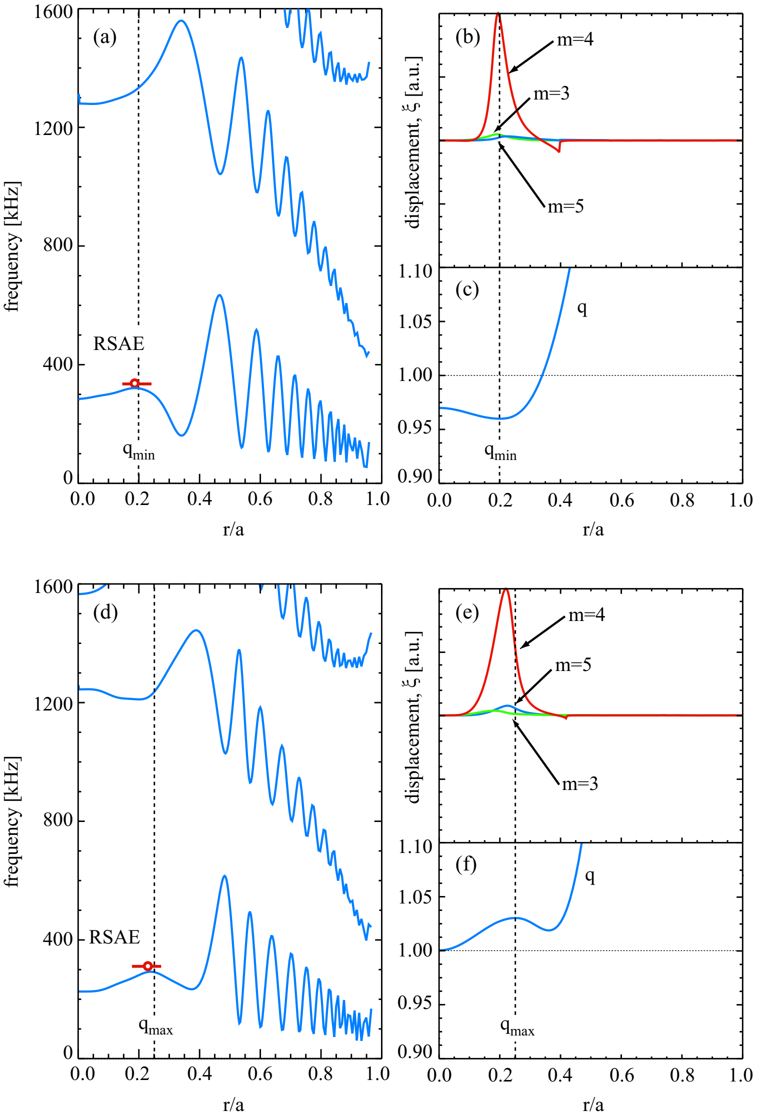

Figure 5-7: NOVA calculations for an up-chirping RSAE with $q_{min} < 1$ for (a) the Alfvén continuum, (b) the radial displacement eigenfunction and (c) the input q profile. Plots (d) through (f) correspond to the case of a down-chirping RSAE with $q_{max} > 1$. Reproduced from Ref. [18].

region of the plasma can be rapidly affected by the divertor, though any changes here may also cascade to the core as the equilibrium adjusts to the new force balance. As noted in prior experimental works, namely Refs. [88, 89], the impurity transport is greatly enhanced by the sawtooth crash which rapidly draws in impurities on time scales much shorter than can be accounted for by diffusive effects. Reference [89] estimated the high Z diffusion coefficient to be less than $6 \times 10^{-2} m^2/s$, which gives a diffusive time scale of $\tau_D \sim 1s$ for Alcator C-Mod. It may be that the impurities had not fully diffused to the core and that this process was accelerated during the first two sawtooth crashes. This hypothesis may be somewhat criticized by the observation of RSAEs appearing prior to the first sawtooth crash in other Alcator C-Mod discharges (in particular 1060525014), though cases such as this are rare and may be exceptions. Additional measurements of the impurity profile are needed to resolve this issue.

Another point is that the RSAEs develop to much larger amplitudes in L-mode as compared to H-mode. The problem of the difference in excitation amplitude between L-mode and H-mode is a difficult one to resolve with the present information. One could consider using the calculated growth rates from NOVA-K as a proxy for the saturated amplitude observed in experiment. This approach however, is complicated on two fronts. First, reliable measurements regarding the energetic ion distribution were not available for most experiments. Secondly, the calculations performed with NOVA-K, using what estimates of the energetic ion distribution are available, tend to show larger growth rates in H-mode compared to L-mode, in contrast to the observations. The trends of the growth rate calculations show rather wild variations for relatively small changes in electron density, suggesting that the growth rate calculations may be unreliable for this purpose. It seems unlikely at this time that significant statements regarding the mode stability can be made. However, another explanation is available which has the possibility of experimental verification.

Recalling that the density perturbation takes the form $\tilde{\rho} = -(\xi \cdot \vec{\nabla})\rho_0 - \rho_0(\vec{\nabla} \cdot \xi)$, we see that a reduction in the gradient term (the first term on the RHS) then implies that the ratio of the total perturbation the compressional component becomes more significant. It may be the case that the flattening of the density gradient in H-mode leads to a reduction in the density perturbation and consequently, an *apparent* decrease in the amplitude measured by PCI. This hypothesis could in principle be tested by comparing measurements from PCI to measurements from the ECE system (measuring thermal electron cyclotron radiation), which should show a lesser change due to the fact that the temperature profiles often evolve less than the density profiles between L-mode and H-mode transitions.

Lastly, the steady decrease of the RSAE amplitude with time, observed in the third L-mode phase in Fig. 5-3, shows a strong correlation with both decreasing sawtooth period and amplitude. The peak temperature in the latter part of this phase drops below 4 keV, supporting the earlier statement that temperatures in excess of this are needed for strong excitation of the RSAEs. What is perhaps most interesting about this observation is that the minimum temperature of the sawtooth cycle is nearly constant for all sawteeth in this period. If the RSAE amplitude could be measured before the end of the sawtooth cycle is reached one may be able to predict the sawtooth period, and possibly the peak temperature of the cycle. It is tempting to think that perhaps the RSAEs have a role in determining the evolution of the sawtooth cycle, though this seems highly unlikely based on the wealth of sawtooth observations in the absence of RSAEs which show varied behavior. Rather, it may be that the RSAEs act as a diagnostic for small changes in the equilibrium which also impact the stability of the equilibrium. This observation suggests that the evolution of the sawtooth cycle may be quite sensitive to the initial conditions which are established by the sawtooth crash of the previous cycle.

5.3 Boundary conditions for the sawtooth crash

The prior observations, including the results of MHD spectroscopy published in Ref. [18], provide strong constraints on the shape of the q profile immediately prior to the sawtooth crash. The presence of a minimum frequency, occurring at about half of the sawtooth period, which is often preceded by down-chirping RSAEs also present a constraint on the system, particularly the post-crash q profile. The minimum frequency of the RSAEs can be more clearly seen in Fig. 5-8. As discussed in chapter 4, the RSAE minimum frequency occurs when $k_\parallel = 0$. The presence of a minimum frequency then implies that a $q_{min} = 1$ condition exists at about halfway through the sawtooth period. Furthermore, the relaxation of the current profile, where the current density is expected to increase on axis, implies that prior to $q_{min} = 1$ the core plasma is in a state with $q > 1$.

In the body of reconnection models for the sawtooth crash, the Kadomtsev model [90], published in 1975, has survived many decades of debate and remains a candidate model. One of the fundamental characteristics of this model is that the q profile following the reconnection has a minimum value of unity at the magnetic axis. This model has been widely criticized for its inability to account for q profiles like that reported in Refs. [81, 83] which show that $q < 1$ throughout the sawtooth cycle. Additionally, the time scales predicted by the Kadomtsev model are generally longer than observed in experiment, though they are a definite improvement over the resistive Sweet-Parker time scale [91, 92]. In considering the Kadomtsev model, we may separate the issue of the time scale, which is based on estimates of inflow and outflow velocities of the plasma near the region of reconnection, from the issue of the magnetic topology modification which is based on conservation of magnetic flux. Furthermore, the observation of q profiles with $q \sim 1$ following the sawtooth crash,

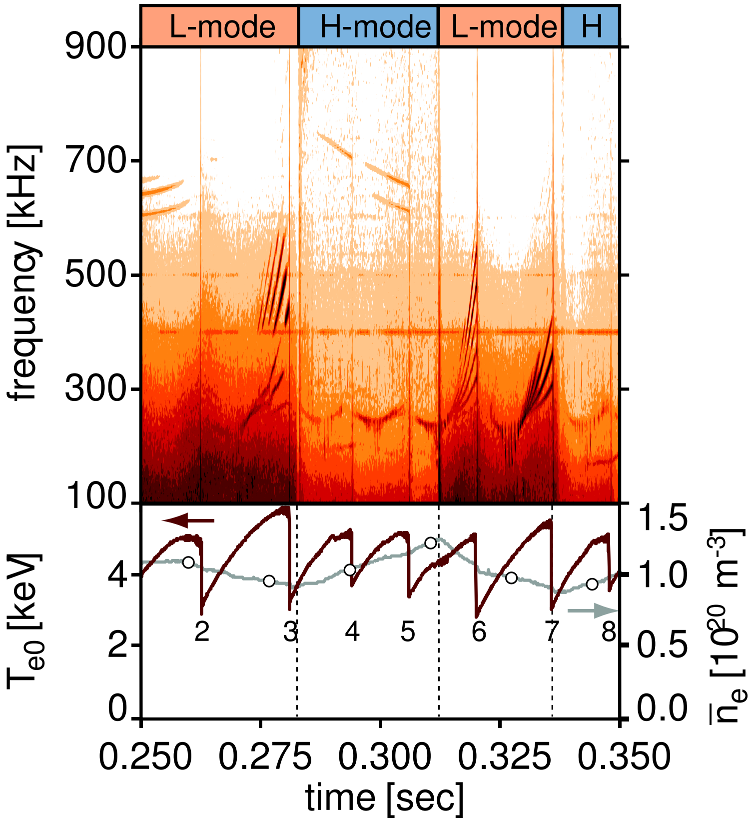

Figure 5-8: Composite PCI spectrogram showing the $q = 1$ RSAEs from Fig. 5-3 in higher resolution. The minimum frequency is apparent, with a minimum occurring at approximately the midpoint of the sawtooth period. Note that faint down-chirping RSAEs follow many of the crashes.

like that reported here for Alcator C-Mod experiments, suggests that there may be two distinct paths for reconnection.

In the case of $q < 1$, the reconnection process may either be "incomplete", where the reconnection does not proceed all the way to the magnetic axis, but stops at some intermediate position, or else there is a process of rapidly enhancing cross field thermal transport while maintaining the magnetic topology [93]. Incomplete reconnection has been incorporated into more recent sawtooth crash models by Porcelli *et al.* [94], which defines an inner region which undergoes a Taylor relaxation preserving the magnetic helicity [95, 96], and an outer region which experiences reconnection of magnetic surfaces. These models may not be applicable to Alcator C-Mod plasma which appear to undergo complete reconnection.

While the time scales of the Kadomtsev model may be incorrect, this does not necessarily invalidate the model of the magnetic topology modification which is based on two axioms: first, that the toroidal flux is conserved in the pre and post reconnection states and secondly, that surfaces of equal helical magnetic flux reconnect. The helical flux in this case is defined to be that which threads a surface with magnetic winding equivalent to that found at the $q = 1$ surface. It is the magnetic flux perpendicular to this helical $m = 1, n = 1$ perturbation which is forced to reconnect when the amplitude of this 1/1 mode becomes large enough. The toroidal flux is defined as

$$\begin{aligned} \Psi_{tor} &= \int_0^r \mathbf{B}_\phi \cdot \mathrm{d}\mathbf{A} \\ &\approx B_0 A(r), \end{aligned} \tag{5.1}$$

where the cross sectional area (A) is a function of the minor radial coordinate r

and the flux surface shaping parameters. The helical magnetic flux (Ψ^*) is found by integrating $\mathbf{B} \cdot \mathrm{d}\mathbf{A}^*$ where $\mathrm{d}\mathbf{A}^* \approx 2\pi R_0 \mathrm{d}r\ (\hat{b}_\perp^*)$ is the $m = 1, n = 1$ helical differential area and $\hat{b}_\perp^* = \hat{\theta} - \epsilon\hat{\phi}$ is the unit vector normal to the magnetic field and in the plane of the flux surface at the $q = 1$ surface, and $\epsilon = r/R_0$. It follows that

$$\Psi^* \approx B_0 \int_0^r \left(\frac{1}{q} - 1\right) 2\pi r\, \mathrm{d}r. \tag{5.2}$$

Notice that in the equation for Ψ^*, the integrand changes sign at the $q = 1$ surface. In the frame of the $m = 1, n = 1$ perturbation the magnetic field is oppositely directed on either side of the $q = 1$ surface. This is precisely the condition needed to generate a magnetic X point in a reconnection process [75, 97]. With the prior expressions for the magnetics fluxes, and the model axiom that surfaces of equal Ψ^* reconnect, the post-crash q profile may be derived from the pre-crash state. This process is illustrated in Fig. 5-9 for the case where the reconnection starts with a mild amount of reversed shear as is expected for the experiments presented here based on observation of the RSAEs [18].

The main conclusion of this section with regard to the Kadomtsev model is that a small local maximum in the post-crash q profile may be generated when the reconnection process begins with a reversed shear configuration. It may be that a more accurate model accounting for the small changes in the toroidal field due to the change in the diamagnetic currents arising from a flattened post-crash pressure profile may have a significant impact on this feature, the changes in the current density giving rise to the effect being essentially perturbations on the equilibrium. Use of this post-crash q profile will be explored as an initial condition for the relaxation of current profiles in the subsequent chapter. The goal of such modeling is produce a self-consistent evolution which predicts both the local maximum and the reverses

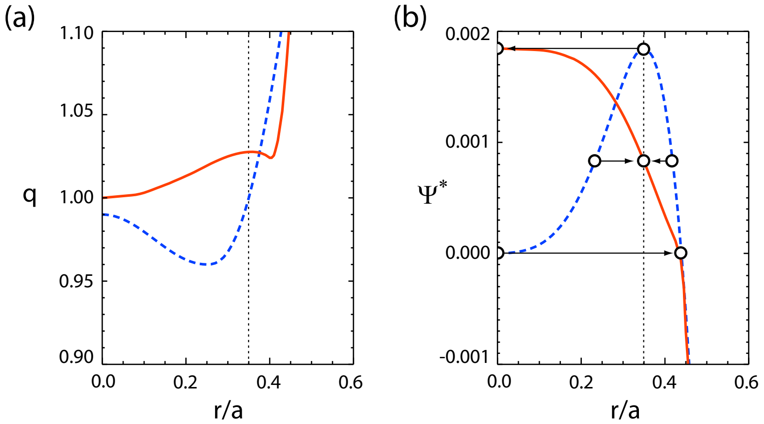

Figure 5-9: Calculations based on the Kadomtsev model showing (a) the pre-crash (blue dashed) and post-crash (orange solid) q profiles and (b) the helical flux function Ψ^*. When the reconnection process begins with a reversed shear q profile, the post-crash state may develop a small local maximum. Reproduced from Ref. [18].

shear necessary for the range of observed RSAE phenomena. As we will see, the maximum in the q profile is associated with a peak in the current density profile. The evolution toward a state with a minimum in q, as determined from the analysis of the up-chirping RSAEs, may result from the tendency of this peak to move toward the axis due to diffusive relaxation. Closure of the model would then test to see if the relaxed profiles can indeed recreate the q profile with the local maximum needed for the down-chirping RSAEs.

Chapter 6

Diffusion of the Electric Field and Ohmic Current

In this chapter we will examine the evolution of the current profile between sawteeth crashes in the reheat phase, to investigate conditions under which reversed shear q profiles may develop. The complexities of the problem are to a large extent hidden in the physics of the resistivity (or conductivity). In the simplest model, the case of classical resistivity based on Coulomb collisions only, the resistivity is a function of the electron temperature and the effective ion charge state, Z_{eff} [98]. In tokamaks, the resistivity should be modified to account for the fraction of electrons which are magnetically trapped and cannot freely circulate [99]. This is the basis for the so-called "neo-classical" corrections to the resistivity.

We can derive an estimate of the trapped particle fraction ($f_{trapped}$) by considering that the particles' energy ($\mathcal{E} = \frac{1}{2}mv^2$) and magnetic moment ($\mu = mv_\perp^2/2B$) are constants of the motion. Assuming a Maxwellian distribution at the low-field side of the tokamak, only those particles with energies greater than μB_+ will circulate, where B_+

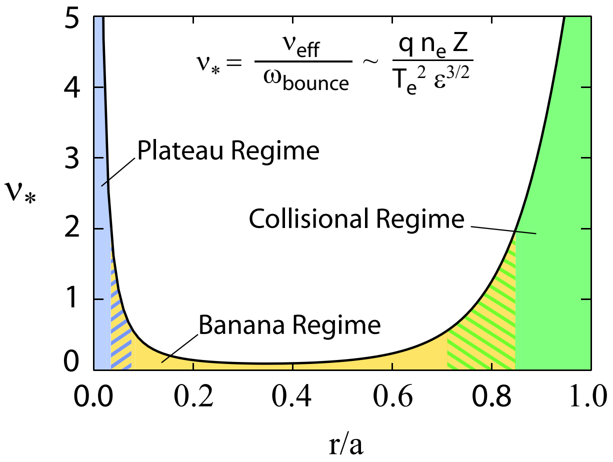

Figure 6-1: The parameter ν_* defines the transport regime. Close to the magnetic axis the transport regime moves from the plateau regime to the banana regime over a very small space.

is the magnitude of the field at the high-field side for a given flux surface. Considering those particles which have vanishing parallel velocity at the high field side of the tokamak, we have $\mathcal{E} = \mu B_+ = \frac{1}{2} m v_{\parallel,-}^2 + \mu B_-$. Expanding $B_\pm$ as $B_0(1 \pm \epsilon)$, the trapped angle in velocity space is related to these parameters by $\tan(\theta_{trapped}) = v_\parallel / v_\perp \sim \sqrt{2\epsilon}$ where $\epsilon = r/R_0$ is the local inverse aspect ratio. The total trapped fraction is the volume in velocity space within the trapped region. Because $\theta_{trapped}$ is independent of velocity, we may solve the problem geometrically. The volume of the trapped cone is approximately $(4\pi/3)v^3\theta_{trapped}$, and the total volume is simply $(4\pi/3)v^3$ for any value of v. In the ratio, the v^3 terms cancel and we have $f_{trapped} \approx \theta_{trapped} \sim \sqrt{2\epsilon}$. Indeed, more accurate calculations reflect this fundamental dependence, and with very nearly the same coefficient [39, 100].

Other factors also come into play near the magnetic axis. Namely, the collision frequency becomes large relative to the bounce frequency of the particle orbits, effectively marking a transition in the nature of the transport to the "plateau regime" [99]. The different transport regimes are illustrated in Fig. 6-1, based on the calculation of the parameter $\nu_* = \nu_{eff}/\omega_{bounce}$ = where ν_{eff} is the effective collision frequency.

The neoclassical corrections used in this analysis are taken from Ref. [101], which employs fits of continuous functions to a set of parameter scans from a code which calculates the various transport coefficients. Note that there is a published errata to accompany Ref. [101], listed here as Ref. [102]. The equations of interest for these studies are the modifications to the conductivity (σ_{neo}), which are given as,

$$\frac{\sigma_{neo}}{\sigma_{Spitzer}} = 1 - \left(1 + \frac{0.36}{Z}\right) X + \frac{0.59}{Z} X^2 - \frac{0.23}{Z} X^3, \tag{6.1}$$

where $\sigma_{Spitzer}$ is the classical conductivity, Z is the effective ionization state and X is given as,

$$X = \frac{f_t}{1 + (0.55 - 0.1 f_t)\nu_*^{1/2} + 0.45(1 - f_t)\nu_*/Z^{3/2}}. \tag{6.2}$$

In Eq. 6.2, f_t is the trapped fraction and $\nu_* = 6.921 \times 10^{-18} q R n_e Z \ln\Lambda / T_e^2 \epsilon^{3/2}$. Unfortunately, the authors of Ref. [101] did not include a representation for f_t, so we have instead used the formulation from Ref. [100]. Without proceeding to simulation, we can observe the trend of the solution near the magnetic axis from Eq. 6.2. Making explicit the ϵ dependence by using $f_t = a\epsilon^{1/2}$ and $\nu_* = b\epsilon^{-3/2}$, we have

$$\begin{aligned} X &= \frac{a\epsilon^{1/2}}{1 + (0.55 - 0.1 a\epsilon^{1/2}) b^{1/2}\epsilon^{-3/4} + 0.45(1 - a\epsilon^{1/2} b\epsilon^{-3/2} Z^{-3/2})} \\ &= \frac{A\epsilon^2}{1 - B\epsilon^{1/2} + C\epsilon^{3/4} + \ldots}, \end{aligned} \tag{6.3}$$

for some combination of parameters A, B, C, and so on. The values of these constants are unimportant, rather, it is the ϵ dependence of the denominator which determines the form of the current diffusion near the magnetic axis. As we will see, the diffusion equation contains terms like $\nabla^2\eta_\parallel$. The derivatives in this expression carry through to the function X defined previously. While the second derivative of X is well behaved at the origin, we can see by Eq. 6.3 that the third derivative does not behave so well. While the current density remains finite at the magnetic axis, its gradient becomes infinite, resulting in a strongly peaked current density profile. It may be that the fits employed in the work of Ref. [101] do not adequately represent the physics near the magnetic axis to within the accuracy required of this work. However, these forms are the best available without resource to calculation of the neoclassical quantities from fundamentals, a significant undertaking in itself. It may also be the case that the neoclassical model in general, does not include all of the necessary physics for accurate modeling of the region near the magnetic axis [103].

In the following, we explore the implications of this formulation relative to the classical case. While toroidal effects and asymmetries will have an impact on the evolution of the current profile, we examine here a cylindrical model as a first step toward illuminating some of the potential problems and solutions with regard to current diffusion.

6.1 Derivation of the Diffusion Equation

As was briefly mentioned in chapters 4 and 5, the current tends to lag far behind the temperature in relation to the steady-state condition - the current is always trying to catch up to the temperature profile. Assuming an Ohm's Law of the form $E_\parallel = \eta_\parallel j_\parallel$, then in steady-state we expect $E_\parallel \approx$ constant and the current density will be proportional to $\eta_{\parallel}^{-1}$ where $\eta_{\parallel}$ is the classical Spitzer resistivity modified to account for reduced collision frequency parallel to the magnetic field [35, 98, 104]. Distributing the total plasma current in accordance with a current density profile proportional to $\eta_{\parallel}^{-1} \sim T_e^{3/2}$ results in a q_0 which is almost always well below unity at the magnetic axis, a condition that is clearly not met on account of the sawteeth which redistribute the current.

In this section we will model the tokamak as a cylindrically symmetric screw pinch and derive a partial differential equation for $j_{\parallel}(r,t)$. In visualizing a tokamak of infinite aspect ratio we take the $\hat{z}$ direction to be equivalent to the toroidal direction, $\hat{\phi}$. We will see that the plasma physics only enters our analysis in the final steps, and in this sense the results derived here are quite general. This analysis derives from the treatment of Faraday's Law and Ampere's Law in the limiting case of a small displacement current. This approximation is justified by the consideration that the phase velocity of the electromagnetic waves in this limit are much smaller than the speed of light, quantified by the statement

$$v_{ph}^2 \sim \frac{\frac{\partial^2 E}{\partial t^2}}{\frac{\partial^2 E}{\partial r^2}} \ll c^2. \tag{6.4}$$

or equivalently,

$$\frac{1}{c^2}\frac{\partial^2 E}{\partial t^2} \ll \frac{\partial^2 E}{\partial r^2}, \tag{6.5}$$

which is exactly the justification needed for the neglect of the displacement current. In this sense, the solutions and method derived here are a subset of the wave equations appropriately filtered for the low frequency limit. We will eventually impose a constitutive relation for **j** in terms of **E** to close the equations. We begin with Faraday's Law and Ampere's Law,

$$\nabla \times \mathbf{E} = -\frac{\partial}{\partial t}\mathbf{B}, \tag{6.6}$$

$$\nabla \times \mathbf{B} = \mu_0 \mathbf{j}. \tag{6.7}$$

The time dependent equation is derived by eliminating $\mathbf{B}$ from Eqs. 6.6 and 6.7 and making use of the vector identity $\nabla \times \nabla \times \mathbf{A} = \nabla(\nabla \cdot \mathbf{A}) - \nabla^2 \mathbf{A}$,

$$\nabla^2 \mathbf{E} - \nabla(\nabla \cdot \mathbf{E}) = \mu_0 \frac{\partial}{\partial t}\mathbf{j}. \tag{6.8}$$

As before, we desire a projection of our equations onto the natural basis defined by $\hat{b}_\parallel$, $\hat{b}_\perp$, and $\hat{r}$. We first derive an expression for the projection of Eq. 6.8 onto the generalized unit vector $\hat{c} = \hat{c}(\mathbf{r}, t)$,

$$\begin{aligned} \nabla^2 E_c - \mu_0 \frac{\partial}{\partial t} j_c \quad &= \quad \nabla \cdot \left[\mathbf{E} \times (\nabla \times \hat{c}) + (\hat{c} \cdot \nabla)\mathbf{E} + (\mathbf{E} \cdot \nabla)\hat{c}\right] + \\ &\quad (\nabla \times \mathbf{E}) \cdot (\nabla \times \hat{c}) - \mu_0 \mathbf{j} \cdot \frac{\partial}{\partial t}\hat{c}, \end{aligned} \tag{6.9}$$

where we have defined $E_c = \mathbf{E} \cdot \hat{c}$ and $j_c = \mathbf{j} \cdot \hat{c}$. It should be reinforced that Eq. 6.9 is approximate only insofar as we have neglected the displacement current which amounts to the neglect of high frequency waves, but is otherwise derived solely from Maxwell's equations. Note that the LHS of Eq. 6.9 has the form of a diffusion equation if E_c is related to j_c via some constitutive relation such as $E_\parallel = \eta_\parallel j_\parallel$. It can be shown that all terms on the RHS are smaller than those on the LHS by at least a factor of $\beta \sim 10^{-2}$ and can be ignored. Taking $\hat{c} = \hat{b}_\parallel$, we have

$$\frac{\partial}{\partial t} j_{\parallel} = \nabla^2 \left(D j_{\parallel} \right) , \tag{6.10}$$

where $D = \eta_{\parallel}/\mu_0$ is a diffusion coefficient with units of L^2/T. We choose to represent the diffusion equation in terms of $j_{\parallel}$ rather than $E_{\parallel}$ (or for that matter, $B_{\perp}$) because we may impose upon the simulations the requirement that the total current be conserved. In experiment, the transformer responds by adjusting the loop voltage to maintain a preset value of total current. Similarly, in the numerical model we adjust the external electric field to maintain a constant total current.

6.2 Current Diffusion in a Cylinder

Studies of current diffusion in cylindrical geometry have been used previously to try to explain a number of phenomena related to sawteeth, including the effect of compound sawteeth [105, 106]. These studies, however, differed from the approach used here in two fundamental ways. First, they considered only classical resistivity. Secondly, they developed coupled equations for the temperature profile and current density profile for an ohmically heated scenario and included an anomalous thermal conductivity as a free parameter. The temperature profiles used in the work presented here were derived from experimental ECE data, and in this sense represent a simpler, and perhaps more robust, model for the current density evolution.

As noted earlier, the primary objective of this effort is to model the diffusion of current between sawteeth crashes to look for conditions when a reversed shear q profile may be generated. The initial conditions for the relaxation of the current density are taken from the Kadomtsev model of section 5.3. From numerous parameter scans within this model it has been determined that a reversed shear q profile may

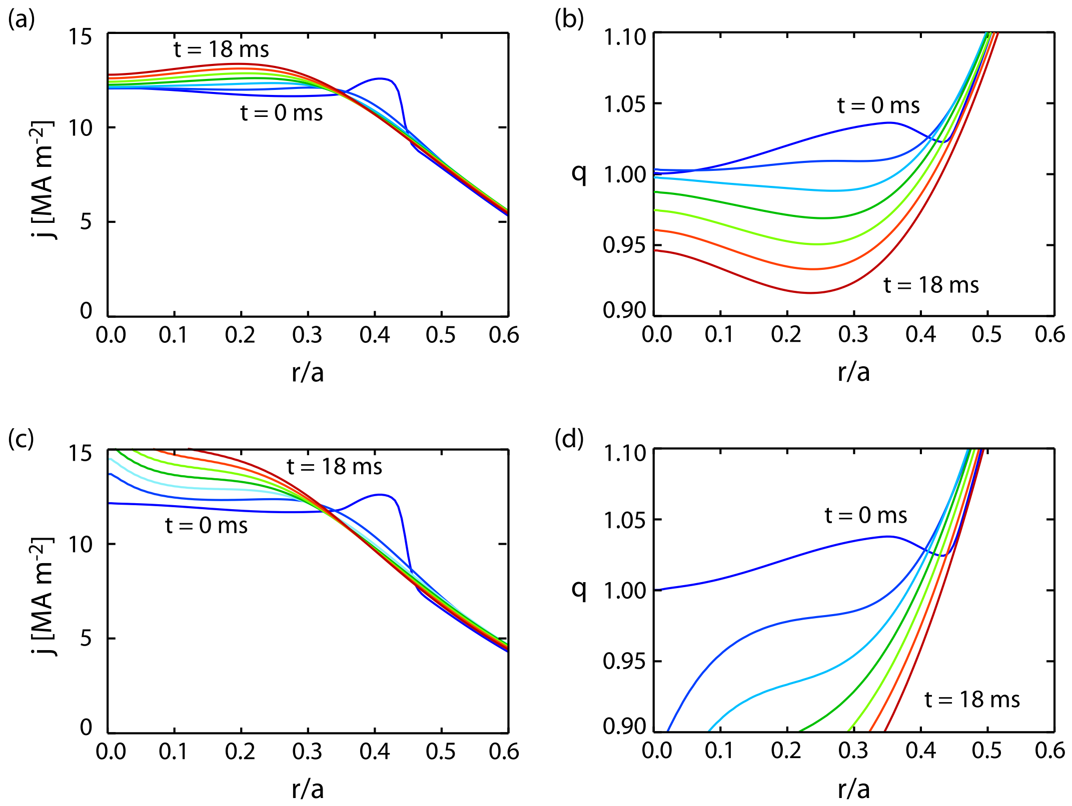

Figure 6-2: Plots of the (a) current density profile and (b) q profile for classical resistivity and a flat impurity profile. Plots (c) and (d) pertain the neoclassical resistivity.

be generated with the neoclassical corrections *only* if the impurity profile is peaked with a non-zero derivative at the magnetic axis. Comparisons of model results using classical and neoclassical resistivity are presented in Fig. 6-2.

The major result of this work is that a steep impurity profile is necessary to counterbalance the enhancement of the resistivity due to the neoclassical effects [18]. A peaked impurity profile increases the resistivity in the plasma core sufficiently to expel current from the magnetic axis toward regions of lower resistivity. The impurity profile is working against the $T_e^{3/2}$ profile and the $\sqrt{\epsilon}$ factor from neoclassical

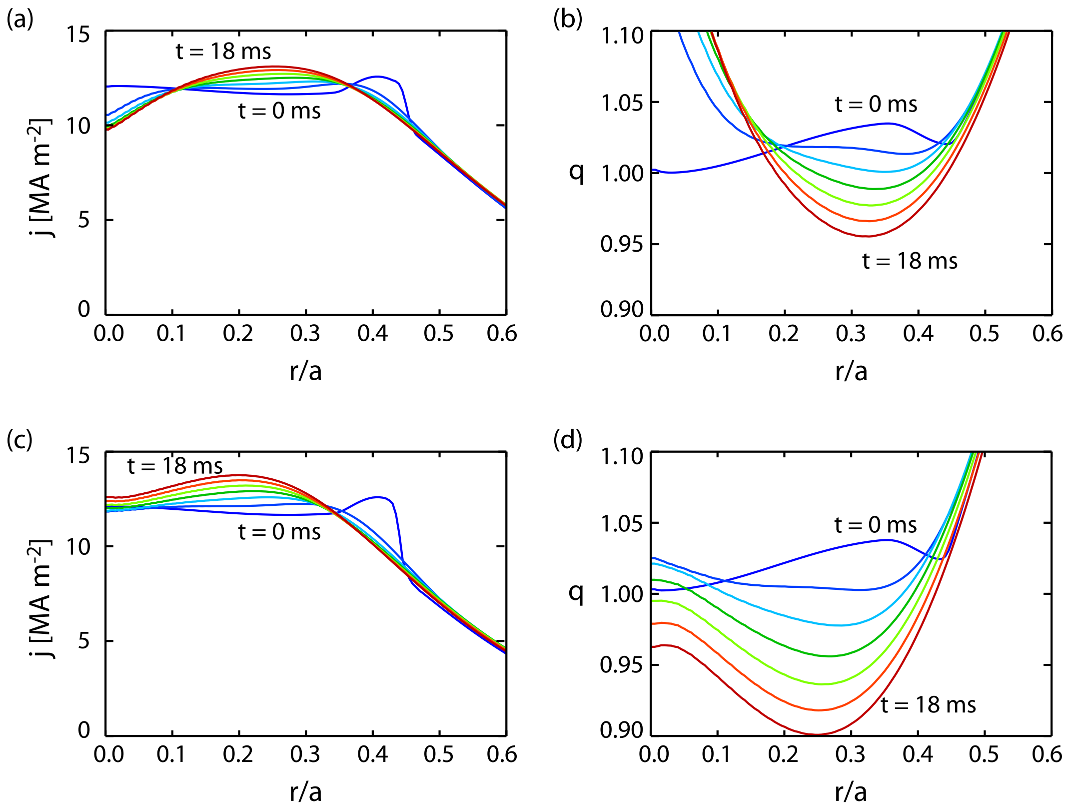

Figure 6-3: Plots of the (a) current density profile and (b) q profile for neoclassical resistivity and a peaked impurity profile. Plots (c) and (d) pertain the neoclassical resistivity.

theory, and hence must be quite strongly peaked for this effect to be realized. While at this time we do not have good impurity profile measurements for Alcator C-Mod, especially for the high Z impurities like molybdenum, experiments from other machines report highly peaked impurity profiles. In particular, a report from FTU, also using molybdenum tiles on the first wall, found highly peaked impurity profiles [65]. Additionally, measurements from JET [88] and ASDEX Upgrade [89] using laser blow-off of high Z materials found a rapid influx of impurities to the core during the sawtooth crash. An older study from the Alcator C tokamak found that carbon and molybdenum impurities peaked strongly on axis following pellet injection [72]. While we are at this time unable to make more definitive statements regarding the source of the anomalous resistivity necessary to generate a reversed shear q profile, it at least seems plausible that an impurity profile may account for a large part of it.

6.3 Bootstrap Current

Another effect within neoclassical theory is the "bootstrap" current, a self-generated current arising from collisional asymmetries of trapped and passing electrons. For completeness, this effect should be considered in the evolution of the current density profiles. During a sawtooth cycle where the plasma pressure profile may change significantly on account of the rapid heating of the plasma core, there is the possibility of a large change in the bootstrap current which could account for much of the observed behavior. However, as will be shown, the total bootstrap current in Alcator C-Mod is expected to be very small and likely does not explain the experimental results. Multiple models of the bootstrap current may be found in Refs. [39] and [101], among others. We use here a simplified representation of the bootstrap current, to gauge its importance in the calculations, from Eq. 25 of [39],

$$j_{bs} \approx -\sqrt{\epsilon} R_0 \left(2.4 T \frac{\mathrm{d}n}{\mathrm{d}\psi} + 0.1 n \frac{\mathrm{d}T}{\mathrm{d}\psi} \right), \tag{6.11}$$

where ψ is the poloidal flux (see Eq. 3.56). For simplicity, we reformulate Eq. 6.11 in terms of derivatives with respect to r, which gives us

$$j_{bs} \approx -\frac{q}{2\pi\sqrt{\epsilon} B_0} \left(2.4\, T \frac{\mathrm{d}n}{\mathrm{d}r} + 0.1\, n \frac{\mathrm{d}T}{\mathrm{d}r} \right). \tag{6.12}$$

Note that this form should be finite everywhere as n' and T' should scale ap-

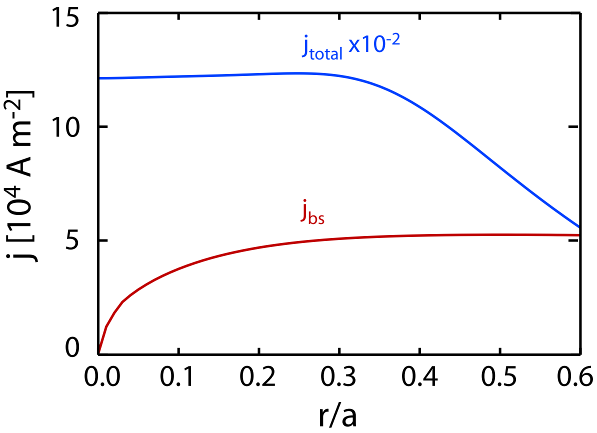

Figure 6-4: Comparison of the total current density for Alcator C-Mod to the theoretical bootstrap current density based on Eq. 6.12.

proximately as r near the origin (consider $n \propto (1-x^2)^p \approx 1 - px^2$ when $x \ll 1$). We see that j_{bs} scales like $B_0\beta/a$ so that in typical Alcator C-Mod conditions, where $\beta \ll 1$, the bootstrap current may be quite small. A plot of the bootstrap current calculated via this form is presented in Fig. 6-4. Recalling that in experiment j_0 will be constrained such that $q_0 \sim 1$, we have that $j_0 \sim B_0/R_0$. The bootstrap current, however, scales as $\beta B_0/a$, so that as a fraction, $j_{bs}/j_0 \sim \beta$ for similar aspect ratio tokamaks. The very low β of Alcator C-Mod plasmas ($\sim 10^{-2}$) means that the bootstrap contribution is generally negligible near the plasma core, and especially so in L-mode plasmas. Profile shape optimization can significantly increase the bootstrap fraction. The example calculations presented in Ref. [39] considered a tokamak with $T_0 \sim 30\,\mathrm{keV}$, a value about an order of magnitude larger than Alcator C-Mod. Thus, it is not likely that the bootstrap current is responsible for the reversed shear in the sawtooth experiments reported here.

Chapter 7

Summary and Future Work

This thesis sought to present a range of phenomena related to RSAEs during the current ramp and sawtoothing phases of Alcator C-Mod operation. The primary tools for the study of these modes are the phase contrast imaging diagnostic (PCI) and the synthetic PCI analysis used with model results from the ideal MHD code NOVA. Among the major results of this work are the identification of the evolution of the q profile during the current ramp phase and sawtoothing phase, constraining both the value of q_{min} and r_{min}. In the absence of q measurements from other diagnostics, these results provide valuable constraints for further modeling of many aspects of Alcator C-Mod plasmas. They may also serve as a benchmark by which the MSE diagnostic can be compared when it comes online. Extensions of this work to include the scaling of the edge amplitude measured by magnetics relative to the core amplitude measured by PCI have provided a solid basis for future experimental and theoretical works along these lines. The explanation of the RSAEs in the first harmonic frequency range by a general mode coupling process is an area of continuing research. As pointed out in chapter 4, the presence of RSAE harmonics may provide an additional avenue for the measurement of a local fluctuation amplitude. With regard to the RSAEs observed during sawteeth, the q profile modeling has been used to constrain models of the current relaxation, suggesting that either the impurity profile is strongly peaked on axis, or that corrections to the neoclassical model are needed.

While the application of RSAEs and other Alfvénic modes to MHD spectroscopy is one particularly useful direction, there are many remaining questions both of practical and theoretical interest. Perhaps one of the largest issues, certainly a practical issue as well as a theoretical puzzle, is that the experimentally measured transport of energetic ions from Alfvén eigenmodes may be an order of magnitude larger than that predicted by codes [22]. It is not fully known at this time what implications Alfvén eigenmodes will have for a burning plasma including alpha particles. A range of Alfvén activity is expected in the next generation devices, in part due to observations of such phenomena in TFTR during its D-T operations [11]. Due to the lack of energetic ion loss measurements for the Alcator C-Mod experiments we cannot at this time draw conclusions about the level of mode-induced transport based on our observations.

In general, one of the greatest sources of uncertainty in the models of RSAE activity is the knowledge of the energetic ion population. It is expected that the energetic ions should have some contribution to the RSAE dispersion relation, perhaps only on the order of 10 kHz or so, but nonetheless a potentially measurable quantity. With additional experimental constraints for the energetic ions it may be possible to test the growth rate models in NOVA-K, or to apply this to another code which calculates the non-linear saturated mode amplitude. This, however, requires that the energetic ion density and pressure profile be known to better than the sensitivity of the code. The energetic ions may have a significant variation of the tail temperature as a function of radius, a property not currently modeled by the single temperature distribution in NOVA-K. A confounding problem with this line of research is the influence of the impurities that often accompany the use of the ICRH system, especially in lower densities like that targeted in these studies. However, if advances are to be made on this front, the requisite condition will be the development of better experimental diagnosis of the energetic ion distribution.

Other matters, such as the relation between the saturated mode amplitude and the operational mode (L vs. H) during sawteeth, or refinement of the measurement of the adiabatic index are open for further investigation, without the need of strong characterization of the energetic ions. One fruitful extension of this work may be to consider further the tunneling effect described in chapter 4. At this time, the author knows of no experimental studies along these lines. A rather straightforward series of experiments could be conducted to examine the dependence of the Mirnov coil signal as a function of the edge Alfvén continuum. Certainly, modification of the edge q profile through changing the plasma current may provide an experimental knob. If one could also find a method of varying the edge density profile without greatly affecting to central density, then this may provide an additional experimental control. The $n_e^{-1/2}$ dependence of the Alfvén continuum means that a rather significant change in density may be needed, suggesting that modification of the current, or perhaps the plasma shape, may be a more reasonable approach. Experiments along these lines may also see benefit from employing the reflectometer system to monitor density fluctuations in the RSAE range of frequencies and, because it can monitor fluctuations outside of the PCI view, it offers the possibility of observing strong density fluctuations near points of continuum interaction where $\omega = \omega_A$. From a theoretical perspective, modeling of the plasma edge is difficult for multiple reasons, not the least of which are the dense coupling of poloidal harmonics and the presence of the separatrix and open field lines [107]. However, this may be an area where definitive experiments prime a theoretical interest in the problem.

With regard to the observations of RSAEs during sawteeth, a significant void in our understanding persists. The reconnection model proposed in chapter 5, based on the Kadomtsev model, seems to agree with the observations of both up-chirping and down-chirping RSAEs. It would be interesting to consider refinements of the Kadomtsev model, accounting for the changes in the diamagnetic currents associated with a flattened pressure profile, and to see how these affect the post-crash q profile and the development of a local maximum. While the relatively small amount of magnetic shear inferred from the presence of the RSAEs brings into question the significance of these results, the existence of any reversed shear remains somewhat of a mystery. The standard neoclassical corrections are known to fail near the origin [103], causing a singularity in the gradient of the current density profile at the magnetic axis. How exactly this singularity is resolved is an interesting question. It may be that the finite size of the particle orbits near the axis requires a non-local transport formulation [108, 109]. Numerous theoretical studies have considered the possibility of an anomalous resistivity or viscosity which may tend to counterbalance the neoclassical effects [103, 110, 111]. And yet, a simple explanation in terms of the impurity profile may also be sufficient, but this requires better experimental diagnosis. Further modeling of the current profile relaxation using more advanced codes, such as TSC [112], to explore different sawtooth models might provide additional insight into the problem and the significance of trapped particle effects responsible for the strong neoclassical corrections near the magnetic axis.

As a final note, the author would like to present a brief exposition of three possibly fruitful topics for research which were not given their due consideration in this thesis, but which may be amenable to study in the near-term.

7.1 RSAE Amplitude Modulation

Direct measurement of the mode amplitude is an important experimental constraint for use in modeling the transport of energetic ions arising from their interaction with Alfvén eigenmodes. Studies using experimental data from other tokamaks have combined measurements of the absolute fluctuation levels of RSAEs and TAEs with measurements of energetic ion loss during this activity as a test of transport models [22, 21, 23, 113]. The results suggest that this aspect of the physics is poorly understood, with the transport rates predicted from codes often significantly less than the measured values. While Alcator C-Mod does not currently possess the capability to directly measure the energetic ion loss, it may be possible to model some aspect of the transport without this data by looking at the decrease in mode amplitude that occurs during transitions between the RSAE phase and the TAE phase. A few of the most notable cases of this effect are presented in Fig. 7-1, corresponding to the $n = 2$ and $n = 3$ RSAEs occurring during the grand cascade in Fig. 4-3.

One could derive absolute fluctuation levels from the absolutely calibrated PCI measurements to scale the perturbation levels in transport modeling of energetic ions. The first part of the problem should be to look for precisely what conditions or qualities of the RSAE/TAE transition are responsible for enhanced energetic ion transport which suppress the amplitude of the lower n RSAEs. Then, taking the modified energetic ion distribution from the transport codes, one could check to see whether these changes appropriately predict the decrease in mode amplitude of the lower n RSAEs, at least through a qualitative analysis of changes in the growth rates from NOVA-K.

Furthermore, a periodic bursting in the RSAE amplitude often arises when the RSAE frequency is close to f_{min}, as shown in Fig. 5-6. One suggestive factor is that

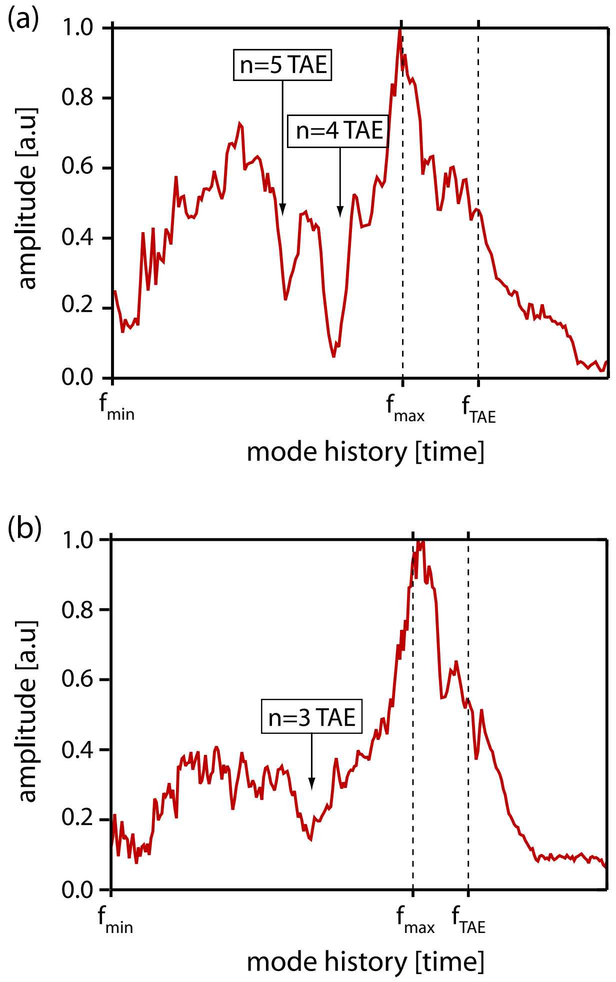

Figure 7-1: Large drops in PCI signal level are observed for the n^{th} RSAE as the $(n+1)^{th}$ even the $(n+2)^{th}$ RSAEs transition into TAEs. These data represent RSAEs excited during the grand cascade near 0.135 sec in Fig. 4-3 for (a) $n = 3$ and (b) $n = 2$.

the bursting behavior seems to occur near integer q values, which has the interesting corollary that the set of RSAEs, typically spanning $n = 2$ to $n = 5$ or more, all have approximately the same frequency. It may be then that in this limit the RSAEs behave more as a single mode structure with a highly nonuniform toroidal structure arising from the superposition of multiple toroidal modes. The varied structure of this collective mode may more efficiently resonate with a larger volume of the energetic ion phase space, leading to a non-linear and bursting behavior similar to fishbones [114].

7.2 The Transition from RSAE to TAE

An abrupt jump in frequency sometimes follows the maximum frequency as the RSAE transitions into a TAE, as in the $n = 3$ mode in Fig. 4-18 where an approximate -15 kHz jump in the TAE frequency is observed. These observations suggest that as the RSAE abruptly ceases to exist, perhaps through a strong encounter with the Alfvén continuum, very quickly a new mode appears. The author is not aware of any reports of a discontinuous RSAE/TAE evolution in the existing literature.

It may be possible with detailed parameter scans in NOVA to model such transitions. In general, NOVA calculates many TAE solutions populating a gap, yet only one is realized in experiment. Determining what selection rule favor a discontinuity in the mode frequency may provide another constraint on the equilibrium. The problem may be somewhat cumbersome in that it likely involves at least a three dimensional parameter space which must be explored numerically, comprising n (the toroidal mode number), q_{min} and another parameter such as a shaping parameter for the density profile or q profile. Also, the energetic ion distribution may play an important role in determining what modes are excited.

7.3 Broadband Turbulence

It was noticed rather late in this thesis work that the broadband turbulence detected by PCI displays a subtle variation as the $q_{min} = 2$ surface enters during the current ramp. This pattern can be just barely distinguished in the PCI data in Fig. 4-3 (100-600 kHz range), where the background spectrum is broadest near 0.135 sec and decreases at earlier and later times. This suggests a modification in the turbulence possibly linked to the presence of rational q surfaces. A relation between the q profile and changes in transport have been noted in other experiments, primarily with respect to internal transport barriers [115].

To illustrate this point more clearly, Fig. 7-2 presents two different measures of the spectra. In panel (a), spectra from three times are presented which show the slight, but significant, enhancement of the broadband spectrum around 0.135 sec. This point is perhaps more clear in panel (b) which shows the integrated power as a function of time. The striking trend is that as q_{min} passes through 2 the low frequency $[0, 50]$ kHz signals decrease and are complemented by an increase in the $[50, 1000]$ kHz signals. While not directly related to the study of Alfvén eigenmodes, the utility of MHD spectroscopy in this subject is critical in determining that the broadband spectrum is modified about $q = 2$.

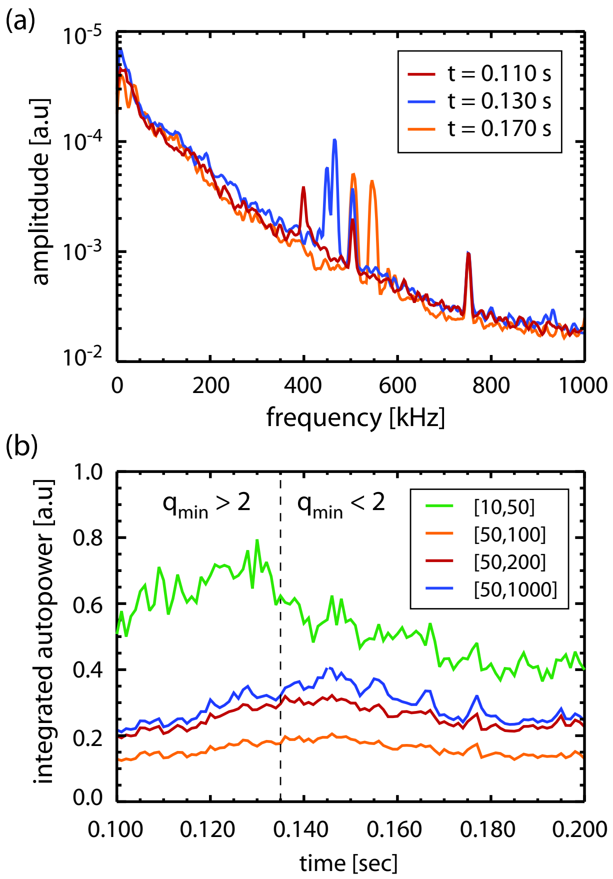

Figure 7-2: (a) The broadband spectrum measured by PCI is observed to increase as q_{min} approaches 2 and then decrease as q_{min} passes below 2. (b) The variation in the broadband spectrum as a function of time divided into separate frequency regimes shows that the low frequency [0,50] kHz band peaks at $q_{min} > 2$ and that the [50,1000] kHz band peaks at $q_{min} < 2$.

Bibliography

[1] H. Alfven. Existence of electromagnetic-hydrodynamic waves. *Nature*, 150:405, 1942.

[2] D.B. Jess, M. Mathioudakis, R. Erdlyi, P.J. Crockett, F.P. Keenan, and D.J. Christian. Alfvén waves in the lower solar atmosphere. *Science*, 323:1582, 2009.

[3] J.W. Belcher. The Jupiter-Io connection: an Alfvén engine in space. *Science*, 238:170, 1987.

[4] R. Behn, G.A. Collins, J.B. Lister, and H. Weisen. Observation of density fluctuations at the resonance layers during Alfvén wave heating. *Plasma Physics and Controlled Fusion*, 29:75, 1987.

[5] M.N. Rosenbluth and P.H. Rutherford. Excitation of Alfvén Waves by high energy ions in a tokamak. *Physical Review Letters*, 34:1428, 1975.

[6] N.N. Gorelenkov, G.J. Kramer, and R. Nazikian. Interpretation of finite pressure gradient effects in the reversed shear Alfvén eigenmode theory. *Plasma Physics and Controlled Fusion*, 48:1255, 2006.

[7] S.E. Sharapov, B. Alper, H.L. Berk, D.N. Borba, B.N. Breizman, C.D. Challis, A. Fasoli, N.C. Hawkes, T.C. Hender, J. Mailloux, S.D. Pinches, and D. Testa. Alfvén wave cascades in a tokamak. *Physics of Plasmas*, 9:2027, 2002.

[8] H. Berk, D.N. Borba, B.N. Breizman, S.D. Pinches, and S.E. Sharapov. Theoretical interpretation of Alfvén cascades in tokamaks with nonmonotonic q profiles. *Physical Review Letters*, 87:185002, 2001.

[9] H. Kimura, Y. Kusama, M. Saigusa, G.J. Kramer, K. Tobita, M. Nemoto, T. Kondoh, T. Nishitani, O. Da Costa, T. Ozeki, T. Oikawa, S. Moriyama, and A. Morioka. Alfvén eignemodes and energetic particle reasearch in JT-60U. *Nuclear Fusion*, 38:1303, 1998.

[10] G.J. Kramer, C.Z Cheng, Y. Kusama, R. Nazikian, S. Takeji, and K. Tobita. Magnetic safety factor profile before and after sawtooth crashes investigated with toroidicity and ellipticity induced Alfvén eignemodes. *Nuclear Fusion*, 41:1135, 2001.

[11] R. Nazikian, G.J. Kramer, C.Z. Cheng, and N.N. Gorelenkov. New interpretation of alpha-particle-drive instabilities in deuterium-tritium experiments on the Tokamak Fusion Test Reactor. *Physical Review Letters*, 91:125003, 2003.

[12] M.A. Van Zeeland, M.E. Austin, , T.N. Carlstrom, T. Deterly, D.K. Finkenthal, C.T. Holcomb, R.J. Jayakumar, G.J. Kramer, M.A. Makowski, G.R. McKee, R. Nazikian, W.A. Peebles, T.L. Rhodes, W.M. Solomon, and E.J. Strait. Internal Alfvén eigenmode observations of DIII-D. *Nuclear Fusion*, 46:S880, 2006.

[13] C. Kessel. Improved plasma performance in tokamaks with reversed magnetic shear. *Physical Review Letters*, 72:1212, 1994.

[14] B.W. Rice, D.G. Nilson, K.H. Burrell, and L.L. Lao. Simultaneous measurement of the q and E_r profiles using the motional Stark effect in high performance DIII-D plasmas. *Review of Scientific Instruments*, 70:815, 1999.

[15] H. Soltwisch. Current distribution measurement in a tokamak by FIR polarimetry. *Review of Scientific Instruments*, 57:1939, 1986.

[16] S. von Goeler, W. Stodiek, and N. Sauthoff. Studies of internal disruptions and m=1 oscillations in tokamak discharges with soft x-ray techniques. *Physical Review Letters*, 33:1201, 1974.

[17] H. Weisen, G. Borg, B. Joye, A.J. Knight, and J.B. Lister. Measurements of the tokamak-safety-factor profile by means of driven resonant Alfvén waves. *Physical Review Letters*, 62:434, 1989.

[18] E.M. Edlund, M. Porkolab, G.J. Kramer, L. Lin, Y. Lin, and S.J. Wukitch. Phase contrast imaging measurements of reversed shear Alfvén eigenmodes during sawteeth in Alcator C-Mod. *Physics of Plasmas*, 16:56106, 2009.

[19] E.M. Edlund, M. Porkolab, G.J. Kramer, L. Lin, Y. Lin, and S.J. Wukitch. Observation of reversed shear Alfvén eigenmodes during sawteeth in Alcator C-Mod. *Physical Review Letters*, 102:165003, 2009.

[20] G.Y. Fu and J.W. Van Dam. Excitation of the toroidicity-induced shear Alfvén eigenmode by fusion alpha particles in an ignited tokamak. *Physics of Fluids B*, 1:1949, 1989.

[21] L. Chen and F. Zonca. Theory of Alfvén waves and energetic paricle physics in burning plasmas. *Nuclear Fusion*, 47:S727, 2007.

[22] W.W. Heidbrink, N.N Gorelenkov, T. Luo, M.A Van Zeeland, R.B. White, M.E. Austin, K.H Burrell, G.J. Kramer, M.A. Makowski, G.R. McKee, and R. Nazikian. Anomalous flattening of the fast ion profile during Alfvén eigenmode activity. *Physical Review Letters*, 99:245002, 2007.

[23] H.L. Berk, B.N. Breizman, and M.S. Pekker. Simulation of Alfvén-wave-resonant-particle interaction. *Nuclear Fusion*, 35:1713, 1995.

[24] M. Porkolab, C. Rost, N. Basse, J. Dorris, E.M. Edlund, L. Lin, Y. Lin, and S.J. Wukitch. Phase contrast imaging of waves and instabilities in high temperature magnetized fusion plasmas. *IEEE Transactions on Plasma Science*, 34:229, 2006.

[25] R.J. Glauber. Photon correlations. *Physical Review Letters*, 10:84, 1963.

[26] F. Zernike. Phase contrast, a new method for the microscopic observation of transparent objects. *Physica*, 1:689, 1934.

[27] R.K. Luneburg. *Mathematical Theory of Optics.* Cambridge University Press, Berkely, California, 1964.

[28] L.D. Landau and E.M. Lifschitz. *The Classical Theory of Fields.* Addison-Wesley, Reading, Massachusetts, 1951.

[29] M.V. Klein and T.E. Furtak. *Optics, Second Edition.* John Wiley and Sons, New York, 1986.

[30] J. Schwinger, L.L. DeRaad, K.A. Milton, and W. Tsai. *Classical Electrodynamics.* Westview Press, Boulder, Colorado, 1998.

[31] R. Feynman. *QED, The Strange Theory of Light and Matter.* Princeton University Press, Princeton, New Jersey, 1985.

[32] M. Greenwald, D. Andelin, N. Basse, S. Bernabei, P. Bonoli, B. Bose, C. Boswell, R. Bravenec, B. Carreras, I. Cziegler, E. Edlund, D. Ernst, C. Fasoli, M. Ferrara, C. Fiore, R. Granetz, O. Grulke, T. Hender, J. Hosea, D.H. Howell, A. Hubbard, J. Hughes, I. Hutchinson, A. Ince-Cushman, J. Irby, B. LaBombard, R. LaHaye, L. Lin, Y. Lin, B. Lipschultz, J. Liptac, S. Lisgo, A. Lynn, E. Marmar, K. Marr, D.R. Mikkelsen, R. McDermott, D. Mossessian, A. Parisot, R. Parker, C. Phillips, P. Phillips, M. Porkolab, M. Redi, J. Rice, W. Rowan, M. Sampsell, G. Schilling, S. Scott, J.T. Scoville, N. Smick, J. Snipes, P. Stangeby, V. Tang, J. Terry, M. Ulrickson, G. Wallace, D. Whyte, J. Wilson, J. Wright, S. Wolfe, S. Wukitch, B. Youngblood, H. Yuh, K. Zhurovich, and S. Zweben. Overview of the Alcator C-Mod program. *Nuclear Fusion*, 45.

[33] S.J. Wukitch, R.L. Boivin, P.T. Bonoli, J.A. Goetz, J. Irby, I. Hutchinson, Y. Lin, A. Parisot, M. Porkolab, E. Marmar, G. Schilling, and J.R. Wilson. Investigation of performance limiting phenomena in a variable phase ICRF antenna in Alcator C-Mod. *Plasma Physics and Controlled Fusion*, 46:1479, 2004.

[34] A. Mazurenko. Phase Contrast Imaging on the Alcator C-Mod Tokamak. *Ph.D. Thesis, Massachusetts Institute of Technology*, 2001.

[35] R.J. Goldston and P.H. Rutherford. *Introduction to Plasma Physics*. Institute of Physics Publishing, Bristol, UK, 1995.

[36] J. Freidberg. *Ideal Magneto-hydrodynamics*. Plenum Press, New York, 1987.

[37] M. Porkolab, R. Boivin, P.T. Bonoli, C. Fiore, M. Greenwald, A. Hubbard, I.H. Hutchinson, Y. In, E. Marmar, P. O'Shea, J. Ramos, J. Rice, J.C. Rost, J.A. Schachter, J. Snipes, Y. Takase, and S.M. Wolfe. Reversed shear experiments in Alcator C-Mod with current ramp and ICRF heating. *Proceedings of the 1997 EPS Conference on Controlled Fusion and Plasma Physics*, 21A:569, 1997.

[38] W.A. Houlberg, C. Gormezano, J.F. Artaud, E. Barbato, V. Basiuk, A. Becoulet, P. Bonoli, R.V. Budny, L.G. Eriksson, D. Farina, Yu. Gribov, R.W. Harvey, J. Hobirk, F. Imbeaux, C.E. Kessel, V. Leonov, M. Murakami, A. Polevoi, E. Poli, R. Prater, H. St. John, F. Volpe, E. Westerhof, and A. Zvonkov. Integrated modelling of the current profile in steady-state and hybrid ITER scenarios. *Nuclear Fusion*, 45:1309, 2005.

[39] C.E. Kessel. Bootstrap current in a tokamak. *Nuclear Fusion*, 34:1221, 1994.

[40] T.S. Taylor. Physics of advanced tokamaks. *Plasma Physics and Controlled Fusion*, 39:B47, 1997.

[41] V. Mukhovatov, A.E. Costley, R. Bartiromo, D. Boucher, N. Fujisawa, Yu. Gribov, G. Janeschitz, L. Johnson, S. Kasai, L. de Kock, E. Marmar, K. Muraoka, A. Nagashima, D. Orlinski, S. Ortolani, F. Perkins, M. Petrov, D. Post, S. Putvinski, M. Rosenbluth, O. Sauter, P. E. Stott, V. Strelkov, G. Vayakis, C. Walker, J. C. Wesley, S. Yamamoto, K. M. Young ITER Physics Expert Groups ITER Joint Central Team, and Home Teams. ITER physics program and implications for plasma measurements. *Review of Scientific Instruments*, 68:1250, 1997.

[42] T.H. Stix. *Waves in Plasmas.* American Institute of Physics, New York, 1992.

[43] M. Brambilla and R. Bilato. Simulation of ion cyclotron heating of tokamak plasmas using coupled Maxwell and quasilinear-Fokker-Planck solvers. *Nuclear Fusion*, 46:S387, 2006.

[44] V. Tang, R.R. Parker, P.T. Bonoli, J.C. Wright, R.S. Granetz, R.W. Harvey, E.F. Jaeger, J. Liptac, C.L. Fiore, M. Greenwald, J.H. Irby, Y. Lin, and S.J. Wukitch. Experimental and numerical characterization of ion-cyclotron heated protons on the Alcator C-Mod tokamak. *Plasma Physics and Controlled Fusion*, 49:873, 2007.

[45] W.W. Heidbrink and G.J. Sadler. The behaviour of fast ions in tokamak experiments. *Nuclear Fusion*, 34:535, 1994.

[46] V. Tang (Lawrence Livermore National Laboratory). Private communications, 2007.

[47] Y. Lin, S.J. Wukitch, P.T. Bonoli, E. Marmar, D. Mossessian, E. Nelson-Melby, P. Phillips, M. Porkolab, G. Schilling, S. Wolfe, and J. Wright. Ion cyclotron range of frequencies mode conversion electron heating in deuterium-hydrogen plasmas in the Alcator C-Mod tokamak. *Plasma Physics and Controlled Fusion*, 45:1013, 2003.

[48] H. Weisen. The phase-contrast technique as an imaging diagnostic for plasma density fluctuations. *Infrared Physics*, 25:543, 1985.

[49] H. Weisen. The phase contrast method as an imaging diagnostic for plasma density fluctuations. *Review of Scientific Instruments*, 59:1544, 1988.

[50] S. Coda. An Experimental Study of Turbulence by Phase-Contrast Imaging in the DIII-D Tokamak. *Ph.D. Thesis, Massachusetts Institute of Technology*, 1997.

[51] I.H. Hutchinson. *Principles of Plasma Diagnostics, Second Edition.* Cambirdge University Press, Cambridge, UK, 2002.

[52] G. Binnig, C.F. Quate, and Ch. Gerber. Atomic force microscope. *Physical Review Letters*, 56:930, 1986.

[53] N. Cramer. *The Physics of Alfvén Waves.* Wilecy-VCH, Berlin, 2001.

[54] H.L. Berk, J.W. Van Dam, Z. Guo, and D.M. Lindberg. Continuum damping of low-n toroidicity induced shear Alfvén eigenmodes. *Phys. Fluids B*, 4:1806, 1992.

[55] N.N. Gorelenkov. Existence of weakly damped kinetic Alfvén eigenmodes in reversed shear tokamak plasmas. *Physics of Plasmas*, 15:110701, 2008.

[56] A. Hasegawa and L. Chen. Kinetic process of plasma heating due to Alfvén wave excitation. *Physical Review Letters*, 35:370, 1975.

[57] D.W. Ross, G.L. Chen, and S.M. Mahajan. Kinetic description of Alfvén wave heating. *Phys. Fluids*, 25:652, 1982.

[58] W.H. Press, B.P. Flannery, S.A. Teuolsky, and W.T. Vetterling. *Numerical Recipes.* Cambridge University Press, Cambridge, UK, 1986.

[59] B.N. Breizman, H.L. Berk, M.S. Pekker, S.D. Pinches, and S.E. Sharapov. Theory of Alfvén eigenmodes in shear reversed plasmas. *Physics of Plasmas*, 10:3649, 2003.

[60] B.N. Breizman, M.S. Pekker, and S.E. Sharapov. Plasma pressure effect of Alfvén cascade eigenmodes. *Physics of Plasmas*, 12:112506, 2005.

[61] G.J. Kramer, N.N. Gorelenkov, R. Nazikian, and C.Z. Cheng. Finite pressure effects on reversed shear Alfvén eigenmodes. *Plasma Physics and Controlled Fusion*, 46:L23, 2004.

[62] R. White. *The Theory of Toroidally Confined Plasmas.* Imperial College Press, London, 2001.

[63] N. Winsor, J. Johnson, and J. Dawson. Geodesic acoustic waves in hydromagnetic systems. *Physics of Fluids*, 11:2448, 1968.

[64] C.Z. Cheng and M.S. Chance. NOVA: a nonvariational code for solving the MHD stability of axisymmetric toroidal plasmas. *Journal of Computational Physics*, 71:124, 1987.

[65] D. Pacella, L. Gabellieri, G. Mazzitelli, K.B. Fournier, and M. Finkenthal. Direct measurement of the impurity radial flux in the FTU plasma core. *Plasma Physics and Controlled Fusion*, 39:1501, 1997.

[66] J.E. Rice, E.S. Marmar, F. Bombarda, and L. Qu. X-ray observations of central toroidal rotation in ohmic alcator c-mod plasmas. *Nuclear Fusion*, 37:421, 1997.

[67] C.Z. Cheng. Kinetic extensions of magnetohydrodynamics for axisymmetric toroidal plasmas. *Physics Reports*, 211:1, 1992.

[68] V.A. Mazur and A.B. Mikhajlovskji. Stabilization of the Alfvén wave instability in a two-component tokamak. *Nuclear Fusion*, 17:193, 1977.

[69] N.N. Gorelenkov, C.Z. Cheng, V.G. Kiptily, M.J. Mantsinen, and S.E. Sharapov. Fast ion effects on fishbones and n=1 kinks in JET simulated by a non-perturbative NOVA-KN code. *Proceedings of the 2004 IAEA conference*, pages TH/5–2Rb, 2004.

[70] P.T. Bonoli, M. Porkolab, J.J. Ramos, W. Nevins, and C. Kessel. Negative magnetic shear modes of operation in the Alcator C-Mod tokamak near the beta limit. *Plasma Physics and Controlled Fusion*, 39:223, 1997.

[71] N.P. Basse, A. Dominguez, E.M. Edlund, C.L. Fiore, R.S. Granetz, A.E. Hubbard, J.W. Hughes, I.H. Hutchinson, J.H. Irby, B. LaBombard, L. Lin, Y. Lin, B. Lipschultz, J.E. Liptac, E.S. Marmar, D.A. Mossessian, R.R. Parker, M. Porkolab, J.E. Rice, J.A. Snipes, V. Tang, J.L. Terry, S.M. Wolfe, S.J. Wukitch, K. Zhurovich, R.V. Bravenec, P.E. Phillips, W.L. Rowan, G.J. Kramer, G. Schilling, S.D. Scott, and S.J. Zweben. Diagnostic systems on Alcator C-Mod. *Fusion Science and Technology*, 51:476, 2007.

[72] R.D. Petrasso, D.J. Sigmar, K.W. Wenzel, J.E. Hopf, M. Greenwald, J.L. Terry, and J. Parker. Observations of centrally peaked impurity profiles following pellet injection in the Alcator-C tokamak. *Physical Review Letters*, 57:707, 1986.

[73] C.F McKee and E.G. Zweibel. Alfvén waves in interstellar gasdynamics. *The Astrophysical Journal*, 440:686, 1995.

[74] H. Smith, B.N. Breizman, M. Lisak, and D. Anderson. Nonlinearly driven second harmonics of Alfvén cascades. *Physics of Plasmas*, 13:042504, 2006.

[75] D. Biskamp. Magnetic reconnection in plasmas. *Astrophysics and Space Science*, 242:165, 1998.

[76] K.W. Gentle, M.E. Austin, and P.E. Phillips. Transport and reconnection in tokamak sawteeth. *Physical Review Letters*, 91:255001, 2003.

[77] R.J. Hastie. Sawtooth instability in tokamak plasmas. *Astrophysics and Space Science*, 256:177, 1998.

[78] A. Weller, A.D. Cheetham, A.W. Edwards, R.D. Gill, A. Gondhalekar, R.S. Granetz, J. Snipes, and J.A. Wesson. Persistent density fluctuations at rational-q surfaces following pellet injection in the Joint European Torus. *Physical Review Letters*, 59:2303, 1987.

[79] E.A. Lazarus, T.C. Luce, M.E. Austin, D.P. Brennan, K.H. Burrell, M.S. Chu, J.R Ferron, A.W. Hyatt, R.J. Jayakumar, L.L. Lao, J. Lohr, M.A. Makowski, T.H Osborne, C.C. Petty, P.A. Politzer, R. Prater, T.L. Rhodes, J.T. Scoville, W.M. Solomon, E.J. Strait, A.D. Turnbull, F.L. Waelbroeck, and C. Zhang. Sawtooth oscillations in shaped plasmas. *Physics of Plasmas*, 14:055701, 2007.

[80] D. Wroblewski and R.T. Snider. Evidence of complete magnetic reconnection during a sawtooth collapse in a tokamak. *Physical Review Letters*, 71:859, 1993.

[81] M. Yamada F.M. Levinton, N. Pomphrey, R. Budny, J. Manickam, and Y. Nagayama. Investigation of magnetic reconnection during a sawtooth craash in a high-temperature tokamak plasma. *Physics of Plasmas*, 1:3269, 1994.

[82] J. O'Rourke. The change in the safety factor profile at a sawtooth collapse. *Plasma Physics and Controlled Fusion*, 33:289, 1991.

[83] H. Soltwisch. Measurement of current-density changes during sawtooth activity in a tokamak by far-infrared polarimetry. *Review of Scientific Instruments*, 59:1599, 1988.

[84] L.L. Lao, , H. St. John, R.D. Stambaugh, A.G. Kellman, and W. Pfeiffer. Reconstruction of current profile parameters and plasma shapes in tokamaks. *Nuclear Fusion*, 25:1611, 1985.

[85] S.E. Sharapov, B. Alper, Yu.F. Baranov, H.L. Berk, D. Borba, C. Boswell, B.N. Breizman, C.D. Challis, M. de Baar, R. de Vries, S. Hacquin, N.C. Hawkes, V.G. Kiptily, H.R. Koslowski, J. Mailloux, M. Nave, S.D. Pinches, P. Sandquist, and N.P. Young. Development of Alfvén spectroscopy in advanced scenarios on JET. *Proceedings of the 21st IAEA Conference*, Chengdu, China (Internation Atomic Energy Agency, Vienna, 2007) Vol. IAEA-CN-149, EX/P6-19, 2006.

[86] P. Sandquist, S.E. Sharapov, M. Lisak, and T. Johnson. Bidirectional tornado modes on the Joint Eurpoean Torus. *Physics of Plasmas*, 14:122506, 2007.

[87] M. Greenwald, R.L. Boivin, F. Bombarda, P.T. Bonoli, C.L. Fiore, D. Garnier, J.A. Goetz, S.N. Golovato, M.A. Graf, R.S. Granetz, S. Horne, A. Hubbard, I.H. Hutchinson, J.H. Irby, B. LaBombard, B. Lipschultz, E.S. Marmar, M.J. May, G.M. McCracken, P. O'Shea, J.E. Rice, J. Schachter, J.A. Snipes, P.C. Stek, Y. Takase, J.L. Terry, Y. Wang, R. Watterson, B. Welch, and S.M. Wolfe. H mode confinement in Alcator C-Mod. *Nuclear Fusion*, 37:793, 1997.

[88] J.A. Wesson, B. Alper, A.W. Edwards, and R.D. Gill. Transport in the sawtooth collapse. *Physical Review Letters*, 79:5018, 1997.

[89] R. Dux, A.G. Peeters, A. Gude, A. Kallenbach, and R. Neu. Z dependence of the core impurity transport in ASDEX Upgrade H mode discharges. *Nuclear Fusion*, 39:1509, 1999.

[90] B.B Kadomtsev. Disruptive instability in tokamaks. *Soviet Journal of Plasma Physics*, 1:389, 1975.

[91] P.A. Sweet. *Electromagnetic Phenomena in Cosmical Physics.* Cambridge University Press, New York, 1958.

[92] E.N. Parker. Sweet's mechanism for merging magnetic fields in conducting fluids. *Journal of Geophysics Research*, 62:509, 1957.

[93] K. Itoh, S-I Itoh, and A. Fukuyama. A sawtooth model based on the transport catastrophe. *Plasma Physics and Controlled Fusion*, 37:1287, 1989.

[94] F. Porcelli, D. Boucher, and M.N. Rosenbluth. Model for the sawtooth period and amplitude. *Plasma Physics and Controlled Fusion*, 38:2163, 1996.

[95] J.B. Taylor. Relaxation of toroidal plasma and generation of reverse magnetic shear. *Physical Review Letters*, 33:1139, 1974.

[96] M.A. Berger. Introduction to magnetic helicity. *Plasma Physics and Controlled Fusion*, 41:B167, 1999.

[97] J. Egedal, A. Fasoli, D. Tarkowski, and A. Scarabosio. Collisionless magnetic reconnection in a toroidal cusp. *Physics of Plasmas*, 8:1935, 2001.

[98] L. Spitzer and R. Härm. Transport phenomena in a completely ionized gas. *Physical Review*, 89:977, 1953.

[99] P. Helander and D.J. Sigmar. *Collisional Transport in Magnetized Plasmas.* Cambridge University Press, Cambridge, UK, 2002.

[100] Y.R. Lin-Liu and R.L. Miller. Upper and lower bounds of the effective trapped particle fraction in general tokamak equilibria. *Physics of Plasmas*, 2:1666, 1995.

[101] O. Sauter, C. Angioni, and Y.R. Lin-Liu. Neoclassical conductivity and bootstrap formulas for general axisymmetric equilibria and abritray collisionality regime. *Physics of Plasmas*, 6:2834, 1999.

[102] O. Sauter, C. Angioni, and Y.R. Lin-Liu. Erratum: "Neoclassical conductivity and bootstrap formulas for general axisymmetric equilibria and abritray collisionality regime". *Physics of Plasmas*, 9:5140, 2002.

[103] B. Coppi and F. Pegoraro. Symmetries and global transport equations. *Physics of Fluids B*, 3:2582, 1991.

[104] A. Kuritsyn, M. Yamada, S. Gerhardt, H. Ji, R. Kulsrud, and Y. Ren. Measurments of the parallel and transverse Spitzer resistivities during collisional magnetic reconnection. *Physics of Plasmas*, 13:055703, 2006.

[105] D.E. Denton, J.F. Drake, R.G. Kleva, and D.A. Boyd. Skin currents and compund sawteeth in tokamaks. *Physical Review Letters*, 56:2477, 1986.

[106] V.V. Parail and G.V. Pereverzev. Internal disruption in a tokamak. *Soviet Journal of Plasma Physics*, 6:14, 1980.

[107] H.L. Berk (U. Texas at Austin). Private communications, 2009.

[108] P. Helander. On neoclassical transport near the magnetic axis. *Physics of Plasmas*, 7:2878, 2000.

[109] A. Bergmann, A.G. Peeters, and S.D. Pinches. Guiding center particle simulation of wide-orbit neoclassical transport. *Physics of Plasmas*, 8:5192, 2001.

[110] S.E. Segre and V. Zanza. Electrical conductivity in tokamaks and extended neoclassical theory. *Nuclear Fusion*, 32:1005, 1992.

[111] F.L. Hinton, R.E. Waltz, and J. Candy. Effects of electromagnetic turbulence in the neoclassical Ohm's Law. *Physics of Plasmas*, 11:2433, 2004.

[112] S.C. Jardin, M.G. Bell, and N. Pomphrey. TSC simulation of ohmic discharges in TFTR. *Nuclear Fusion*, 33:371, 1993.

[113] S. Bernabei, M.G. Bell, R. Budny, D. Darrow, E.D. Fedrickson, N. Gorelenkov, J.C. Hosea, R. Majeski, E. Mazzucato, R. Nazikian, C.K. Phillips, J.H. Rogers, G. Schilling, R. White, J.R. Wilson, F. Zonca, and S. Zweben. Role of Alfvén instabilities in energetic ion transport. *Physics of Plasmas*, 6:1880, 1999.

[114] B. Coppi and F. Porcelli. Theoretical model of fishbone oscillations in magnetically confined plasmas. *Physical Review Letters*, 3:2272, 1986.

[115] Y. Koide, M. Mori, T. Fujita, H. Shirai, T. Hatae, T. Takizuka, H. Kimura, T. Oikawa, N. Isei, A. Isayama, S. Takeji, Y. Kawano, A. Sakasai, Y. Kamada, T. Fukuda, and S. Ishida. Study of internal transport barriers by comparison of reversed shear and high-β_p discharges in JT-60U. *Plasma Physics and Controlled Fusion*, 40:641, 1998.